High-resolution infrared emission spectroscopy of diatomic and triatomic metal hydrides

by

Alireza Shayesteh

A thesis
presented to the University of Waterloo
in fulfillment of the
thesis requirement for the degree of
Doctor of Philosophy
in
Chemistry

Waterloo, Ontario, Canada, 2006

I hereby declare that I am the sole author of this thesis. This is a true copy of the thesis, including any required final revisions, as accepted by my examiners.

I understand that my thesis may be made electronically available to the public.

Abstract

Several hydrides of Group 2 and 12 elements were generated in the gas phase using an emission source that combines an electrical discharge with a high temperature furnace, and their high-resolution infrared emission spectra were recorded with a Fourier transform spectrometer. Two classes of molecules were studied: *a*) diatomic metal hydrides BeH, MgH, CaH, SrH, ZnH and CdH; *b*) linear triatomic metal hydrides BeH_2, MgH_2, ZnH_2 and HgH_2.

Infrared emission spectra of BeH, MgH, CaH, SrH, ZnH and CdH free radicals contained several vibration-rotation bands in their $^2\Sigma^+$ ground electronic state. The new data were combined with all the previous ground state data from diode laser infrared spectra and pure rotation spectra available in the literature. Spectroscopic constants, i.e., vibrational band origins, rotational, centrifugal distortion, and spin-rotation interaction constants, were determined for each observed vibrational level by least-squares fitting of all the data. In addition, the data from all isotopologues were fitted simultaneously using the empirical Dunham-type energy level expression for $^2\Sigma^+$ states, and correction parameters due to the breakdown of the Born-Oppenheimer approximation were determined. The equilibrium internuclear distances (r_e) of ^{9}BeH, ^{24}MgH, ^{40}CaH, ^{88}SrH, ^{64}ZnH and ^{114}CdH were determined to be 1.342424(2), 1.729721(1), 2.002360(1), 2.146057(1), 1.593478(2) and 1.760098(3) Å, respectively, and the corresponding r_e distances for ^{9}BeD, ^{24}MgD, ^{40}CaD, ^{88}SrD, ^{64}ZnD and ^{114}CdD are 1.341731(2), 1.729157(1), 2.001462(1), 2.145073(1), 1.593001(2) and 1.759695(2) Å, respectively.

Gaseous BeH_2, MgH_2, ZnH_2 and HgH_2 molecules were discovered and unambiguously identified by their high-resolution infrared emission spectra. The ν_3 antisymmetric stretching fundamental band and several hot bands in the ν_3 region were rotationally analyzed, and spectroscopic constants were obtained for almost all naturally-occurring isotopologues. The rotational constants of the 000 ground states were used to determine the r_0 internuclear distances. For BeH_2, ZnH_2, ZnD_2, HgH_2 and HgD_2 molecules, the rotational constants of the 000, 100, 01^10 and 001 levels were used to determine the equilibrium rotational constants (B_e) and the associated equilibrium internuclear distances (r_e). The r_e distances of ZnH_2 and ZnD_2 differed by about 0.01%, and those of HgH_2 and HgD_2 differed by about 0.005%. These discrepancies were larger than the statistical uncertainties by one order of magnitude, and were attributed to the breakdown of the Born-Oppenheimer approximation.

Acknowledgements

First and foremost I would like to express my deep gratitude to my supervisor, Professor Peter Bernath, for his invaluable support and guidance in the development of this research. I was very fortunate to have worked under supervision of such a distinguished scientist. I would like to thank Professor Robert Le Roy who taught me many fundamental concepts in the subject of Molecular Spectroscopy, and provided me with his computer programs. He helped me as much more than a member of the advisory committee.

I would also like to thank other members of my PhD advisory committee, Professor Frederick McCourt and Professor Nick Westwood, for their support and guidance during the years of my graduate studies. I thank the current and former members of our laboratory for their help and friendship. Especially, I would like to acknowledge my collaborations with Keith Tereszchuk, Iouli Gordon, Dominique Appadoo and Shanshan Yu in conducting experiments in our laboratory. The work presented here was financially supported in part by the Natural Sciences and Engineering Research Council (NSERC) of Canada, and in part by Ontario Graduate Scholarships (OGS).

Finally, I am indebted to my wife, Mahboobeh, who encouraged me and supported me in every aspect of my life in the past five years. It is to her I wish to dedicate this thesis.

For my wife

Contents

List of Tables

List of Figures

Chapter 1

Introduction

Transient molecules such as free radicals are generally important in chemistry as reaction intermediates. Although these molecules are highly reactive and relatively unstable, they dominate the chemistry in energetic environments such as in flames, the upper atmosphere, stellar atmospheres and the interstellar medium [1]. It is possible to provide a controlled environment in the laboratory to study such molecules. Flames, discharges, or high temperature furnaces are usually used to generate transient molecules in the gas phase, and it is often necessary to produce them at low pressures in order to minimize their collisions and interactions with other particles [2].

High-resolution spectroscopy is one of the best experimental tools for studying transient molecules. The energy levels of a molecule are quantized as governed by the time-independent Schrödinger equation, and molecular spectroscopy is based on the interaction of light with molecules as they transit from one energy level to another. Detailed information about electronic structure, chemical bonding and geometries of molecules can be obtained from careful analyses of their high-resolution spectra. Spectroscopic data can also be used to predict thermochemical properties of molecules.

This thesis concentrates on high-resolution infrared emission spectroscopy of diatomic and triatomic hydrides of Group 2 and 12 elements in the gas phase. More specifically, infrared emission spectra of BeH, MgH, CaH, SrH, ZnH and CdH free radicals were recorded and analyzed. In addition, gaseous BeH_2, MgH_2, ZnH_2 and HgH_2 molecules were discovered, and their high-resolution infrared emission spectra were analyzed.

1.1 Gaseous Metal Hydrides

Hydrogen is the most abundant element in the Universe. Some diatomic metal hydrides, e.g., MgH, CaH, CrH and FeH, have been found in cool stars [3], and their identifications have been primarily based on high-resolution laboratory spectra. For example, the green bands of MgH appear strongly in the absorption spectra of many cool stars, and are used to estimate the magnesium isotope abundances [4].

Metal hydrides are among the simplest inorganic molecules. They are favourite target molecules for quantum chemists because of the small number of valence electrons and the simplicity of metal-hydrogen bonding. Ab initio theoretical calculations on metal hydrides can predict reliable molecular parameters, and high quality experimental data on metal hydrides serve as benchmarks for testing the accuracy of ab initio methods. High-resolution spectra of metal hydrides are also useful for studying isotope effects. Hydrogen is the only element for which isotopic masses can differ by nearly a factor of two. Therefore, substitution of a hydrogen atom with deuterium in a diatomic molecule can have large effects on some molecular parameters. For example, effects due to the breakdown of the Born-Oppenheimer approximation (see below) are observed most clearly in hydrides and deuterides.

The investigation of infrared emission spectra of Group 2 and 12 hydrides in our laboratory was started by searching for the vibration-rotation transitions of BeH and BeD. Infrared emission spectra were recorded, and in addition to BeH and BeD free radicals, several vibration-rotation bands of gaseous BeH_2 and BeD_2 were observed. Although BeH_2 is a famous molecule and its chemical bonding is discussed in introductory chemistry textbooks, there was no previous observation of free BeH_2 in the gas phase, and the only metal dihydride known in the gas phase was FeH_2 [5]. Similar experiments were carried out in our laboratory in order to produce MgH_2, CaH_2, SrH_2 and BaH_2 in the gas phase, but only MgH_2 could be generated successfully. Since the electronic configurations of Group 2 and 12 atoms are very similar, our experiments were continued by searching for gaseous ZnH_2, CdH_2 and HgH_2. All these molecules were produced successfully in the gas phase, and their high-resolution infrared emission spectra were recorded. In the course of these experiments, new infrared emission spectra were obtained for MgH, CaH, SrH, ZnH and CdH free radicals, and were analyzed to yield improved molecular constants.

1.2 Molecular Energy Levels

1.2.1 Born-Oppenheimer approximation

The quantized energy levels of a molecule can be computed in principle by solving the time-independent Schrödinger equation [6]:

$$\hat{\mathrm{H}}\,\Psi = \left(\hat{\mathrm{T}}_{\mathrm{N}} + \hat{\mathrm{T}}_{\mathrm{e}} + \hat{\mathrm{V}}_{\mathrm{NN}} + \hat{\mathrm{V}}_{\mathrm{eN}} + \hat{\mathrm{V}}_{\mathrm{ee}}\right)\Psi = E\,\Psi\,. \qquad (1.1)$$

In this equation, $\hat{\mathrm{T}}_{\mathrm{N}}$ and $\hat{\mathrm{T}}_{\mathrm{e}}$ are kinetic energy operators for the motion of the nuclei and electrons, respectively. The terms $\hat{\mathrm{V}}_{\mathrm{NN}}$, $\hat{\mathrm{V}}_{\mathrm{eN}}$ and $\hat{\mathrm{V}}_{\mathrm{ee}}$ represent the contributions to the potential energy due to nuclear-nuclear repulsions, electron-nuclear attractions, and electron-electron repulsions, respectively. The first step in solving Eq. (1.1) is to separate electronic motions from nuclear motions, and is known as the Born-Oppenheimer approximation [7]. Electrons and nuclei experience similar Coulombic forces, but electrons are much lighter. Therefore, electrons move much faster than the nuclei. In the "clamped nuclei" approximation, the positions of the nuclei are held fixed at various molecular geometries ($\mathbf{r}_\alpha$), and the electronic Schrödinger equation is solved to obtain the electronic structure:

$$\hat{\mathrm{H}}_{\mathrm{el}}\,\psi_{\mathrm{el}} = \left(\hat{\mathrm{T}}_{\mathrm{e}} + \hat{\mathrm{V}}_{\mathrm{eN}} + \hat{\mathrm{V}}_{\mathrm{ee}}\right)\psi_{\mathrm{el}} = E_{\mathrm{el}}\,\psi_{\mathrm{el}}\,. \qquad (1.2)$$

Since the nuclear motion is frozen at each particular geometry, the nuclear-nuclear repulsion term in Eq. (1.1) is just a number, and can be added to E_{el} to give the total potential energy for a particular electronic state:

$$U(\mathbf{r}_\alpha) = E_{\mathrm{el}}(\mathbf{r}_\alpha) + \mathrm{V}_{\mathrm{NN}}(\mathbf{r}_\alpha)\,. \qquad (1.3)$$

This potential energy depends parametrically on the positions of the nuclei ($\mathbf{r}_\alpha$), and there is no general analytic function for it. Within these approximations, the total wavefunction is a simple product of electronic and nuclear wavefunctions [6],

$$\Psi(\mathbf{r}_i;\mathbf{r}_\alpha) \approx \psi_{\mathrm{el}}(\mathbf{r}_i;\mathbf{r}_\alpha)\chi_{\mathrm{N}}(\mathbf{r}_\alpha)\,, \qquad (1.4)$$

and the following two equations should be solved consecutively to obtain the energy levels:

$$\left(\hat{\mathrm{T}}_{\mathrm{e}} + \hat{\mathrm{V}}_{\mathrm{eN}} + \hat{\mathrm{V}}_{\mathrm{ee}} + \mathrm{V}_{\mathrm{NN}}\right)\psi_{\mathrm{el}}(\mathbf{r}_i;\mathbf{r}_\alpha) = U(\mathbf{r}_\alpha)\,\psi_{\mathrm{el}}(\mathbf{r}_i;\mathbf{r}_\alpha)\,, \qquad (1.5)$$

$$\left(\hat{\mathrm{T}}_{\mathrm{N}} + U(\mathbf{r}_\alpha)\right)\chi_{\mathrm{N}}(\mathbf{r}_\alpha) = E_{\mathrm{N}}\,\chi_{\mathrm{N}}(\mathbf{r}_\alpha)\,. \qquad (1.6)$$

In other words, Eq. (1.5) is solved first for all possible nuclear positions ($\mathbf{r}_\alpha$) to obtain $U(\mathbf{r}_\alpha)$, which is used in Eq. (1.6) as the potential energy function governing the motion of the nuclei. The variables $\mathbf{r}_i$ and $\mathbf{r}_\alpha$ in the above equations represent the positions of electrons and nuclei, respectively.

The potential energy $U(\mathbf{r}_\alpha)$ can be calculated at various geometries using an ab initio computation package. For diatomic molecules, Eq. (1.6) can be solved in the molecular coordinate system with only one variable, which is the internuclear distance r. Therefore, if the potential energy curve of a diatomic molecule, $U(r)$, is known accurately, the vibration-rotation energy levels can be obtained by numerical solution of Eq. (1.6) without any further approximations. For polyatomic molecules, however, $U(\mathbf{r}_\alpha)$ is a multi-variable function, which is usually approximated by a Taylor series expansion in symmetry-adapted internal coordinates [8]. The vibration-rotation energy levels of polyatomic molecules can be obtained by solving Eq. (1.6) variationally or by perturbation theory.

1.2.2 Diatomic molecules

There are very few diatomic molecules for which the potential energy curve of the ground electronic state, $U(r)$, is known accurately over a large range of internuclear distances. The most commonly used function for representing the parametric dependence of U on r was first introduced by Dunham [9], and is a Taylor series expansion about the equilibrium internuclear distance (r_e). At the bottom of the potential energy curve, both $U(r_e)$ and the first derivative of $U(r)$ are equal to zero. Therefore, $U(r)$ is expressed by the following equation,

$$U(r) = \tfrac{1}{2} k_2 (r - r_e)^2 + \tfrac{1}{6} k_3 (r - r_e)^3 + \tfrac{1}{24} k_4 (r - r_e)^4 + \cdots, \qquad (1.7)$$

in which k_n is the nth derivative of the potential energy function evaluated at r_e. The leading term on the right of Eq. (1.7) is the well-known potential energy function of a harmonic oscillator. By keeping only the first term on the right of Eq. (1.7) and solving Eq. (1.6) analytically, the harmonic oscillator solution is obtained for the nonrotating molecule:

$$E(\mathrm{v}) = hc\, G(\mathrm{v}) = hc\, \omega_e \left(\mathrm{v} + \tfrac{1}{2}\right), \qquad \mathrm{v} = 0, 1, 2, \ldots \qquad (1.8)$$

In this equation, h and c are the Planck constant and the speed of light, respectively, $G(\mathrm{v})$ and ω_e have units of cm^{-1}, and v is the vibrational quantum number. However, since the potential energy curve of a diatomic molecule is always anharmonic, it is customary to express the vibrational energy as a power series in $\left(\mathrm{v} + \tfrac{1}{2}\right)$:

$$G(\mathrm{v}) = \omega_e \left(\mathrm{v} + \tfrac{1}{2}\right) - \omega_e x_e \left(\mathrm{v} + \tfrac{1}{2}\right)^2 + \omega_e y_e \left(\mathrm{v} + \tfrac{1}{2}\right)^3 + \cdots \qquad (1.9)$$

Similarly, the rotation of a diatomic molecule can be approximated by that of a rigid rotor, for which the energy levels are given by:

$$E(J) = hc\, F(J) = hc\, BJ(J+1), \qquad J = 0, 1, 2, \ldots \qquad (1.10)$$

In this equation, $F(J)$ and B have units of cm^{-1}, and J is the rotational angular momentum quantum number. The equilibrium rotational constant (B_e) is related to the moment of inertia (I_e) and to the equilibrium internuclear distance (r_e) by [6],

$$hc\,B_\mathrm{e} = \frac{\hbar^2}{2I_\mathrm{e}} = \frac{\hbar^2}{2\mu r_\mathrm{e}^2}\,, \tag{1.11}$$

in which μ is the reduced mass, defined as:

$$\mu = \frac{m_\mathrm{A} m_\mathrm{B}}{m_\mathrm{A} + m_\mathrm{B}}\,. \tag{1.12}$$

As the molecule rotates, the internuclear distance increases due to the centrifugal force, and it is customary to express the rotational energy as a power series in $J(J+1)$:

$$F_\mathrm{v}(J) = B_\mathrm{v} J(J+1) - D_\mathrm{v}\left[J(J+1)\right]^2 + H_\mathrm{v}\left[J(J+1)\right]^3 + \cdots \tag{1.13}$$

The rotational constant has a vibrational dependence because the average value of $\langle 1/r^2 \rangle$ changes as the vibrational quantum number increases. The vibrational dependence of the rotational constant is customarily expressed as a power series in $\left(\mathrm{v} + \tfrac{1}{2}\right)$,

$$B_\mathrm{v} = B_\mathrm{e} - \alpha_\mathrm{e}\left(\mathrm{v} + \tfrac{1}{2}\right) + \gamma_\mathrm{e}\left(\mathrm{v} + \tfrac{1}{2}\right)^2 + \cdots, \tag{1.14}$$

in which α_e and γ_e are the vibration-rotation interaction constants.

There is another popular expression for the potential energy of diatomic molecules, introduced by Morse [10]:

$$U(r) = D\left[1 - \exp\left(-\beta(r - r_e)\right)\right]^2. \tag{1.15}$$

In this equation, D is the dissociation energy relative to the bottom of the potential, and β is now called the Morse potential parameter. If one uses the Morse function for $U(r)$, Eq. (1.6) can be solved analytically for the nonrotating molecule, and the following vibrational energy level expression is obtained:

$$G(\mathrm{v}) = \omega_\mathrm{e}\left(\mathrm{v} + \tfrac{1}{2}\right) - \omega_\mathrm{e} x_\mathrm{e}\left(\mathrm{v} + \tfrac{1}{2}\right)^2. \tag{1.16}$$

The first anharmonicity constant ($\omega_\mathrm{e} x_\mathrm{e}$) appears naturally in the energy level expression obtained from the Morse potential [6], but the higher order constants in Eq. (1.9) are all identically zero for this case.

The Dunham potential, Eq. (1.7), is more general than the Morse potential, but it is not possible to solve Eq. (1.6) analytically using this potential. However, Dunham used the WKB (Wentzel–Kramers–Brillouin) method to solve Eq. (1.6) semiclassically [11], and obtained the following expression for the vibration-rotation energy levels [9]:

$$E_{\mathrm{v},J}(\mathrm{cm}^{-1}) = \sum_{m=0} \sum_{l=0} Y_{l,m}\left(\mathrm{v} + \tfrac{1}{2}\right)^l \left[J(J+1)\right]^m. \tag{1.17}$$

The Dunham $Y_{l,m}$ coefficients can be mapped to the conventional spectroscopic constants in Eqs. (1.9), (1.13) and (1.14):

$Y_{1,0} \approx \omega_e$, $Y_{0,1} \approx B_e$, $Y_{0,2} \approx -D_e$,

$Y_{2,0} \approx -\omega_e x_e$, $Y_{1,1} \approx -\alpha_e$, and so forth.

Within the Born-Oppenheimer and the first order semiclassical approximations, the $Y_{l,m}$ coefficients of different isotopologues of a diatomic molecule are related by the following equation, in which μ_α and μ_β are reduced masses:

$$Y_{l,m}^{(\alpha)} = Y_{l,m}^{(\beta)} \left(\frac{\mu_\beta}{\mu_\alpha} \right)^{m+l/2} . \qquad (1.18)$$

Since the Born-Oppenheimer and the first-order WKB approximations can break down, especially for light diatomic molecules (small reduced masses), it is often necessary to add small correction terms to Eq. (1.18). These terms are generally referred to as the "Born-Oppenheimer breakdown correction parameters".

The rotational energy level expressions in Eqs. (1.13) and (1.17) are appropriate only for closed-shell molecules with no unpaired electrons. In general, the total angular momentum (exclusive of nuclear spin) of a diatomic molecule (**J**) is the vector sum of orbital (**L**), spin (**S**) and rotational (**R**) angular momenta, see Figure 1.1. The projections of **S**, **L** and **J** on the internuclear axis are denoted by Σ, Λ and Ω, respectively [6]. The notation for the electronic states of diatomic molecules is ${}^{2S+1}\Lambda_\Omega$, similar to the ${}^{2S+1}L_J$ notation used for atoms.

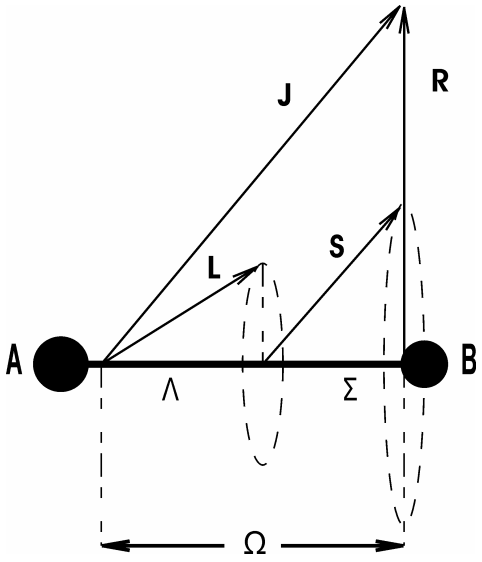

Fig. 1.1. Angular momenta in diatomic molecules.

For all electronic states with $|\Omega| \neq 0$, there is at least a double degeneracy for each value of J, and the sub-levels are labelled by their parities. The total (+/–) parity is defined based on the $\hat{E}^*$ symmetry operator that inverts all coordinates of the nuclei and electrons (in the laboratory frame) with the origin at the center of mass [6]:

$$\hat{E}^* \Psi(X_i, Y_i, Z_i) = \Psi(-X_i, -Y_i, -Z_i) = \pm \Psi(X_i, Y_i, Z_i). \quad (1.19)$$

In molecular spectroscopy, it is common to use the rotationless (*e*/*f*) parity rather than the total parity. The (*e*/*f*) parity is defined by the following equations for integer J values:

$$\hat{E}^* \Psi = +(-1)^J \Psi \quad \text{for } e; \quad (1.20a)$$

$$\hat{E}^* \Psi = -(-1)^J \Psi \quad \text{for } f. \quad (1.20b)$$

Similarly, for half-integer J,

$$\hat{E}^* \Psi = +(-1)^{J-1/2} \Psi \quad \text{for } e; \quad (1.21a)$$

$$\hat{E}^* \Psi = -(-1)^{J-1/2} \Psi \quad \text{for } f. \quad (1.21b)$$

The rotationless (*e*/*f*) parity is more convenient to use than the total parity because the alternation of sign with J has been removed [6]. There is no degeneracy for a closed-shell system ($^1\Sigma^+$ state), and all rotational levels have *e* parity.

The ground electronic state for all diatomic metal hydrides studied in this thesis is $^2\Sigma^+$ state. The "+" sign superscript indicates that the orbital part of the electronic wavefunction is symmetric with respect to the σ_v planes of reflection in the molecular frame [6]. Since L is equal to zero and S is equal to ½ for the $^2\Sigma^+$ states, the total angular momentum quantum number (J) is given by $J = N \pm ½$, in which N is the rotational angular momentum quantum number. The rotational energy level expressions in Eqs. (1.13) and (1.17) become applicable to $^2\Sigma^+$ states if J is replaced by N.

There is a double degeneracy in the rotational levels of a $^2\Sigma^+$ state, and the doublets are labelled by *e* and *f* parities. The J and N quantum numbers in a $^2\Sigma^+$ state are related by:

$J = N + ½$ for *e* parity;

$J = N - ½$ for *f* parity.

The (*e*/*f*) degeneracy in the rotational levels of a $^2\Sigma^+$ state can be lifted due to the spin-rotation interaction Hamiltonian [6]:

$$\hat{\mathbf{H}}_{SR} = \gamma \hat{\mathbf{N}} \cdot \hat{\mathbf{S}} = \gamma (\hat{\mathbf{J}} - \hat{\mathbf{S}}) \cdot \hat{\mathbf{S}}. \quad (1.22)$$

As a result, the *e* levels are shifted by $+ ½ \gamma N$, and the *f* levels by $- ½ \gamma (N+1)$. The spin-rotation interaction energy can also be expressed by a Dunham-type formula, which is described in Chapter 2.

1.2.3 Symmetric linear triatomic molecules

There are three vibrational modes in symmetric linear triatomic molecules: symmetric stretching (σ_g), bending (π_u), and antisymmetric stretching (σ_u). The bending mode is doubly degenerate because the molecule can bend in two planes. In its simplest form, the potential energy function, $U(\mathbf{r}_\alpha)$, is expressed as a sum of harmonic oscillator potentials associated with each vibrational mode. For symmetric linear molecules with $D_{\infty h}$ symmetry (B–A–B), it is convenient to use the following symmetry-adapted coordinates [6]:

$$s_1 = \frac{1}{\sqrt{2}}(\Delta r_1 + \Delta r_2) \quad \text{for symmetric stretching } (\nu_1),$$

$$s_2 = \sqrt{r_1 r_2}\,\Delta\theta \quad \text{for bending } (\nu_2),$$

and $$s_3 = \frac{1}{\sqrt{2}}(\Delta r_1 - \Delta r_2) \quad \text{for antisymmetric stretching } (\nu_3).$$

The variables r_1 and r_2 are the two internuclear distances (A–B), θ is the B–A–B angle, and Δr_1 and Δr_2 represent the displacements from the equilibrium internuclear distance (r_e). In terms of these symmetry-adapted coordinates, the potential energy function is given by the following equation:

$$U(\mathbf{r}_\alpha) = \tfrac{1}{2} F_{11} s_1^2 + \tfrac{1}{2} F_{22} s_2^2 + \tfrac{1}{2} F_{33} s_3^2, \tag{1.23}$$

in which F_{11}, F_{22} and F_{33} are the force constants [6]. When this potential energy function is used in the Schrödinger equation in Eq. (1.6), the following vibrational energy expression is obtained for the non-rotating molecule:

$$G(\nu_1, \nu_2, \nu_3) = \omega_1\left(\nu_1 + \tfrac{1}{2}\right) + \omega_2(\nu_2 + 1) + \omega_3\left(\nu_3 + \tfrac{1}{2}\right). \tag{1.24}$$

In this equation, ν_1, ν_2 and ν_3 are the vibrational quantum numbers for the symmetric stretching (σ_g), bending (π_u), and antisymmetric stretching (σ_u) modes, respectively, and the ω_i (i = 1, 2, 3) are the harmonic vibrational frequencies. The term (ν_2 + 1) appears for the bending because each oscillator of the doubly degenerate pair contributes $\frac{1}{2}\omega_2$ of zero-point energy.

The potential energy function in Eq. (1.23) can be expanded to include cubic and quartic terms, i.e., F_{111}, F_{122}, F_{133}, F_{1111}, F_{1122}, etc. When cubic and quartic terms are included in $U(\mathbf{r}_\alpha)$ in Eq. (1.6), the following vibrational energy expression [6] is obtained using second-order perturbation theory:

$$G(\mathrm{v}_1,\mathrm{v}_2^{\ell},\mathrm{v}_3)=\omega_1\left(\mathrm{v}_1+\tfrac{1}{2}\right)+\omega_2\left(\mathrm{v}_2+1\right)+\omega_3\left(\mathrm{v}_3+\tfrac{1}{2}\right)$$
$$+x_{11}\left(\mathrm{v}_1+\tfrac{1}{2}\right)^2+x_{22}\left(\mathrm{v}_2+1\right)^2+x_{33}\left(\mathrm{v}_3+\tfrac{1}{2}\right)^2+g_{22}\ell^2 \qquad (1.25)$$
$$+x_{12}\left(\mathrm{v}_1+\tfrac{1}{2}\right)\left(\mathrm{v}_2+1\right)+x_{13}\left(\mathrm{v}_1+\tfrac{1}{2}\right)\left(\mathrm{v}_3+\tfrac{1}{2}\right)+x_{23}\left(\mathrm{v}_2+1\right)\left(\mathrm{v}_3+\tfrac{1}{2}\right).$$

The x_{ij} constants in Eq. (1.25) are analogous to the $\omega_e x_e$ constants of diatomic molecules, and ℓ is the vibrational angular momentum quantum number associated with the bending mode.

The ground electronic state for all triatomic metal hydrides studied in this thesis is a $^1\Sigma_g^+$ state with no unpaired electrons. The symmetry of the 000 ground state is thus Σ_g^+, and the symmetries of other vibrational levels can be obtained using direct-product tables [6]. For example, the symmetry of the 111 level is: $\Sigma_g^+ \otimes \Pi_u \otimes \Sigma_u^+ = \Pi_g$. While the rotational levels of all Σ^+ states ($\ell = 0$) have only *e* parity, those of the Π, Δ, and Φ states ($\ell \geq 1$) are doubly degenerate, and are labelled by *e* and *f* parities.

The rotational energy for linear triatomic molecules [12] is expressed as a power series in $[J(J+1) - \ell^2]$:

$$F_{[\mathrm{v}]}(J) = B_{[\mathrm{v}]}\left[J\left(J+1\right)-\ell^2\right]-D_{[\mathrm{v}]}\left[J\left(J+1\right)-\ell^2\right]^2+\cdots \qquad (1.26)$$

and the vibrational dependence of the rotational constant $B_{[\mathrm{v}]}$ is given by:

$$B_{[\mathrm{v}]} = B_\mathrm{e}-\alpha_1\left(\mathrm{v}_1+\tfrac{1}{2}\right)-\alpha_2\left(\mathrm{v}_2+1\right)-\alpha_3\left(\mathrm{v}_3+\tfrac{1}{2}\right), \qquad (1.27)$$

which is analogous to Eq. (1.14) for diatomic molecules. The equilibrium rotational constant (B_e) is related to the equilibrium internuclear distance (r_e) via the moment of inertia equation. For a linear B–A–B molecule:

$$hc\,B_\mathrm{e} = \frac{\hbar^2}{2I_\mathrm{e}} = \frac{\hbar^2}{4\,m_\mathrm{B}\,r_\mathrm{e}^2}\ . \qquad (1.28)$$

There is a small term in the vibration-rotation Hamiltonian [12] that splits the *e* and *f* parity sub-levels of the Π states ($\ell = 1$). The *e* levels are shifted by $+\frac{1}{2}qJ(J+1)$, and the *f* levels by $-\frac{1}{2}qJ(J+1)$. The constant q is called the "rotational ℓ-type doubling constant".

1.2.4 Vibration-rotation perturbations

When two energy levels lie close to one another, and the wavefunctions associated with them have certain symmetries, the two wavefunctions mix. This mixing causes the energy levels to be pushed apart from each other, while their total energy remains unchanged. There are three important selection rules for perturbations in the vibrational and rotational levels of linear molecules in a $^1\Sigma_g^+$ electronic state:

(1) $\Delta J = 0$,

(2) $g \leftrightarrow g$ or $u \leftrightarrow u$,

(3) $e \leftrightarrow e$ or $f \leftrightarrow f$.

In case of a two-level perturbation, a 2×2 Hamiltonian matrix should be diagonalized to obtain the perturbed energy levels. For example, if the unperturbed wavefunctions are labelled by $|f_1\rangle$ and $|f_2\rangle$, the following Hamiltonian matrix should be diagonalized,

$$\mathbf{H} = \begin{pmatrix} E_1^0 & V \\ V & E_2^0 \end{pmatrix}, \tag{1.29}$$

in which $\langle f_1 | \hat{\mathrm{H}} | f_1 \rangle = E_1^0$, $\langle f_2 | \hat{\mathrm{H}} | f_2 \rangle = E_2^0$, and $\langle f_1 | \hat{\mathrm{H}} | f_2 \rangle = V$.

Vibrational perturbations are common in symmetric linear triatomic molecules; for example, $\omega_1 \approx 2\omega_2$ for the CO_2, CS_2 and BeF_2 molecules [13-15]. These perturbations are called “Fermi resonances” when the two interacting vibrational levels have the same symmetry [12]. Vibrational levels with different symmetries can also perturb one another as long as the above selection rules are not violated and the interaction matrix element V is nonzero.

1.3 Experimental Methods

1.3.1 The discharge-furnace emission source

An emission source that combines an electrical discharge with a high temperature furnace was used to generate metal hydride molecules in the gas phase. An alumina tube (120 cm long, 5 cm diameter) was placed inside a tube furnace, which can provide temperatures up to 1600°C. The metals (Be, Mg, Ca, Sr, Zn or Hg) were placed in the central part of the alumina tube, either directly or inside small zirconia or tantalum boats. Two stainless-steel tube electrodes were located inside both ends of the alumina tube, and were connected to a 3 kV / 330 mA dc power supply. The tube was sealed with CaF_2, BaF_2 or KBr windows, and was evacuated using a rotary pump. Pure hydrogen or deuterium flowed slowly through the tube at pressures ranging from 1 to 3 Torr. For some experiments, hydrogen and deuterium were mixed with either helium or argon gases before reaching the tube. The central part of the alumina tube was heated using the tube furnace to a temperature at which the vapour pressure of the metal is about 1 Torr. For example, the temperature for beryllium experiment was 1500°C and for zinc experiment was 470°C. Both ends of the alumina tube were cooled by a constant flow of water on the outside surface, and a dc discharge was created between the two stainless-steel electrodes. A schematic diagram of the discharge-furnace emission source is presented in Figure 1.2.

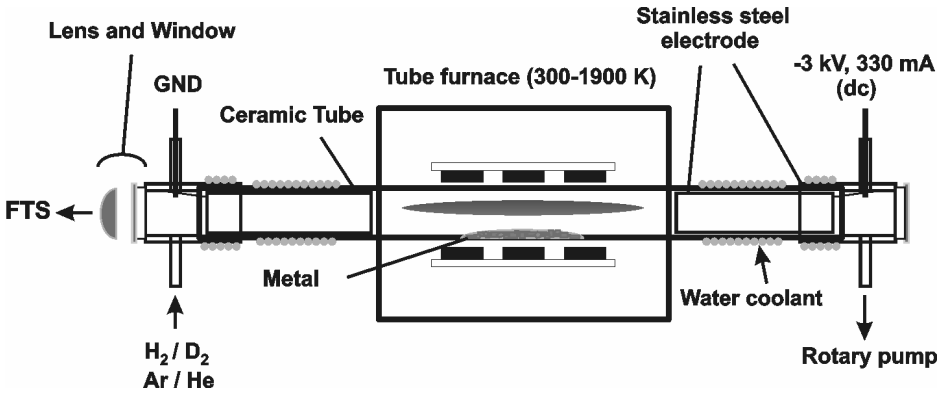

Fig. 1.2. The discharge-furnace emission source

The ground state Be, Mg, Ca, Sr, Zn or Hg atoms are excited (particularly to the metastable ^3P state) in the presence of the electrical discharge, and then react with molecular hydrogen to produce gaseous metal hydrides. A fraction of the metal hydride molecules generated in this source are in excited vibrational and rotational states, and they relax to the ground state by collisions or by emission of infrared radiation. A CaF_2, BaF_2 or KBr lens was used to focus this emission onto the entrance aperture of a Bruker IFS 120 HR Fourier transform spectrometer.

1.3.2 Fourier transform infrared emission spectrometry

It is well-known that emission spectroscopy is more sensitive than absorption spectroscopy in the visible and ultraviolet spectral regions [1]. This is due to the fact that in absorption spectra the noise arises mainly from the background continuum. Compared to an absorption experiment, the noise is reduced in an emission experiment because the continuum is absent. Although the total signal level is also reduced in emission spectra compared to absorption spectra, the noise declines much more than does the signal, and the overall signal-to-noise ratio is increased. This improvement in sensitivity is particularly important for transient molecules because of their low concentrations [16].

Although infrared spectrometers are routinely operated in absorption, the advantages of emission spectroscopy persist into the infrared spectral region. Infrared emission spectra are obtained when the sample has a higher temperature than the spectrometer. The blackbody emission from the hot source is a continuum that can be a major source of noise. This noise can be greatly reduced by limiting the field of view with cold apertures and by limiting the spectral range with appropriate infrared filters [1]. Fourier transform spectrometers have several advantages over grating spectrometers [17-21], especially in the infrared spectral region. High-resolution Fourier transform emission spectroscopy has proven to be a powerful technique for discovering new molecules in the gas phase [1].

The central component of a Fourier transform spectrometer is a Michelson interferometer, which is shown schematically in Figure 1.3. This device consists of two mirrors whose planes are perpendicular to each other. One of the mirrors is fixed, and the other mirror moves at a constant velocity. There is a beamsplitter between these mirrors that ideally reflects 50% of the incident radiation to one mirror and transmits the other 50% to the second mirror. The radiation returns from the two mirrors and recombines at the beamsplitter

where, on average, 50% of each beam goes back towards the source and 50% is passed to a detector. If collimated light of wavenumber $\tilde{\nu}$ and intensity $I(\tilde{\nu})$ is passed into the interferometer, the signal at the detector as a function of optical path difference (x) is given by:

$$I'(x) = \tfrac{1}{2} I(\tilde{\nu})\left[1 + \cos\left(2\pi\tilde{\nu}x\right)\right]. \tag{1.30}$$

$I'(x)$ consists of a dc component, $\tfrac{1}{2} I(\tilde{\nu})$, and an ac component which is the interferogram:

$$I(x) = \tfrac{1}{2} I(\tilde{\nu})\cos\left(2\pi\tilde{\nu}x\right). \tag{1.31}$$

For a source emitting a continuous spectrum $B(\tilde{\nu})$, the interferogram is given by:

$$I(x) = \tfrac{1}{2}\int_{-\infty}^{+\infty} B(\tilde{\nu})\cos\left(2\pi\tilde{\nu}x\right)d\tilde{\nu}. \tag{1.32}$$

Ideally, $I(x)$ is detected at the detector, and the spectrum, $B(\tilde{\nu})$, is obtained by computing a complex Fourier transform of the interferogram [17-21]:

$$B(\tilde{\nu}) = \tfrac{1}{2}\int_{-\infty}^{+\infty} I(x)\exp\left(-2\pi i\tilde{\nu}x\right)dx. \tag{1.33}$$

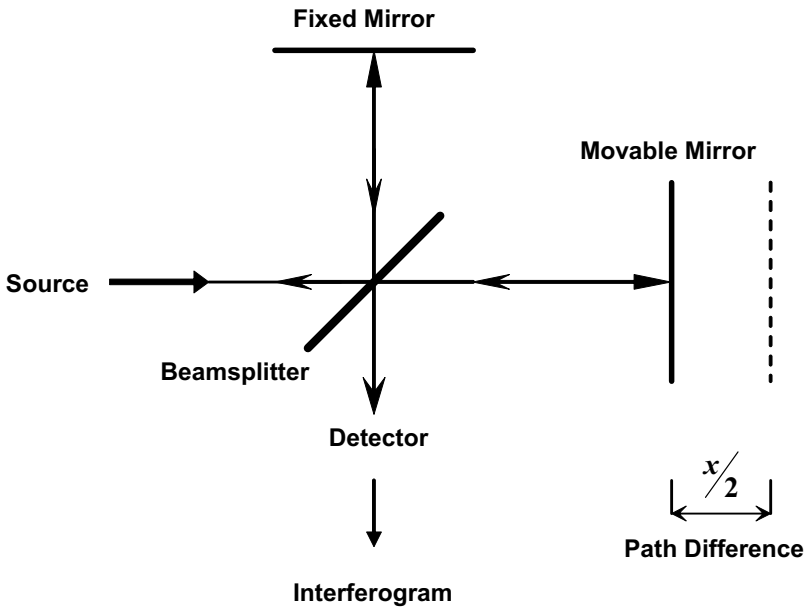

Fig. 1.3. A schematic representation of a basic Michelson interferometer.

The limits of integration in Eq. (1.33) cannot be $-\infty$ and $+\infty$ in practice, and they are replaced by –L and +L, where L is the maximum optical path difference in an experiment. This results in a finite resolution for the spectrum, which is usually defined as the full width at half maximum (FWHM) for spectral lines, and is given by:

$$\mathrm{FWHM\,(cm^{-1})} = \frac{0.6}{\mathrm{L}}. \qquad (1.34)$$

Bruker has chosen to define the resolution as 0.9/L for its instruments. For example, for a spectrum recorded at an instrumental resolution of 0.01 cm^{-1}, the maximum optical path difference (L) is 90 cm for our Bruker IFS 120 HR Fourier transform spectrometer.

For the infrared emission spectra of metal hydrides, the spectrometer was operated under vacuum with either CaF_2 or KBr beamsplitters. Two infrared detectors, cooled by liquid nitrogen, were used: InSb (1750–9000 cm^{-1}) or HgCdTe (800–5000 cm^{-1}). The signal-to-noise ratio for the InSb detector above 1800 cm^{-1} is nearly five times larger than that for the HgCdTe (MCT) detector. Depending on the experiment, appropriate infrared filters were used, e.g., 2900 cm^{-1}, 2200 cm^{-1}, 1700 cm^{-1} or 1600 cm^{-1} longwave-pass filters. Although the path between the emission source and the spectrometer was purged with nitrogen gas and the spectrometer was evacuated, absorption lines due to atmospheric water vapour and carbon dioxide appeared in the spectra.

1.4 Data Analyses

Program WSPECTRA written by Carleer (Université Libre de Bruxelles) was used to measure line positions in the spectra. This program finds peaks based on first and second derivatives. Since the spectrometer was operated under vacuum, no air-vacuum correction was required, but the wavenumber scale of the spectra had to be calibrated. Emission lines from the vibration-rotation transitions of carbon monoxide (impurity) appeared in several spectra of metal hydrides, and were used for absolute wavenumber calibration. The calibration factors for these infrared spectra were typically about 1.000002, based on the accurate CO transition frequencies determined by heterodyne frequency measurements [22].

1.4.1 Rotational assignments

All the vibration-rotation bands analyzed for the metal dihydrides (BeH_2, MgH_2, ZnH_2 and HgH_2) obeyed the $\Delta J = \pm 1$ selection rule. For the vibration-rotation bands of diatomic hydrides (BeH, MgH, CaH, SrH, ZnH and CdH) in $^2\Sigma^+$ ground electronic states, the selection rule is $\Delta N = \pm 1$. The rotational quantum numbers of the lower and upper states are customarily represented by J'' and J', respectively. In the case of $^2\Sigma^+$ states, J'' and J' should be replaced by N'' and N', respectively. The symbol J is used for the rotational quantum number throughout the following paragraphs, and all the equations listed below will be applicable to $^2\Sigma^+$ states if J is replaced by N.

The bands with $\Delta J = \pm 1$ selection rule have a P-branch ($J' = J''-1$) and an R-branch ($J' = J''+1$). The notations $P(J)$ and $R(J)$ for individual lines are equivalent to $P(J'')$ and $R(J'')$, respectively. When the rotational energies of the lower and upper states are represented by $B''J''(J''+1)$ and $B'J'(J'+1)$, respectively, the following general expression is obtained for transition frequencies of P and R branches [6]:

$$\tilde{\nu}_{P,R} = \tilde{\nu}_0 + (B' + B'')m + (B' - B'')m^2 , \qquad (1.35)$$

in which $\tilde{\nu}_0$ is the band origin, $m = J''+1$ for the R-branch and $m = -J''$ for the P-branch. Similarly, when centrifugal distortion terms are added to the rotational energy expression, the transition frequencies are given by a higher-order polynomial in m. An interactive Loomis-Wood program, which fits the observed transition frequencies to simple polynomials, was used to facilitate the rotational assignments.

The transition frequencies given by Eq. (1.35) depend on both lower and upper state constants. In cases in which one of the states is perturbed due to interactions with other nearby states, it may be difficult to assign the rotational lines using Eq. (1.35). An alternative method for rotational assignments is based on "combination differences" defined by the following equations [6]:

$$\Delta_2 F''(J'') \equiv \tilde{\nu}\left[R(J-1)\right] - \tilde{\nu}\left[P(J+1)\right] = 4B''\left(J'' + \tfrac{1}{2}\right), \tag{1.36}$$

$$\Delta_2 F'(J') \equiv \tilde{\nu}\left[R(J)\right] - \tilde{\nu}\left[P(J)\right] = 4B'\left(J' + \tfrac{1}{2}\right). \tag{1.37}$$

$\Delta_2 F''(J'')$ is called the lower state combination difference because it depends only on the lower state rotational constants. Similarly, $\Delta_2 F'(J')$ is called the upper state combination difference. Rotational lines were assigned using Eqs. (1.36) or (1.37) when one of the states was perturbed.

1.4.2 Least-squares fitting of the data

After the rotational assignments of the spectral lines, the data were fitted using the known energy level expressions and spectroscopic constants, i.e., vibrational band origins, rotational constants and centrifugal distortion constants, were determined. The ability of a set of molecular parameters to reproduce the observed transition frequencies accurately is represented by the "dimensionless standard error" of the fit, defined by [23]:

$$\overline{\sigma}_{\mathrm{f}} = \left\{ \frac{1}{\mathrm{N} - \mathrm{M}} \sum_{i=1}^{\mathrm{N}} \left[\frac{y_{\mathrm{calc}}(i) - y_{\mathrm{obs}}(i)}{u(i)} \right]^2 \right\}^{1/2}. \tag{1.38}$$

In the above equation, N and M are the number of experimental data and the number of parameters, respectively, $y_{\mathrm{obs}}(i)$ is an observed transition frequency with an uncertainty of $u(i)$, and $y_{\mathrm{calc}}(i)$ is a transition frequency predicted by the model. A fit of good quality should have $\overline{\sigma}_{\mathrm{f}} \sim 1.0$ because larger values of $\overline{\sigma}_{\mathrm{f}}$ indicate that the molecular model used is inadequate for reproducing the data within their experimental uncertainties.

Since the molecular energy level expressions are usually in the form of polynomials and the observed transition frequencies depend on the energies of both upper and lower states, the molecular parameters obtained from least-squares fitting are often highly correlated. This correlation among the parameters can cause problems in rounding. For example, if all parameters determined from a fit are rounded at their first significant digits, the $\overline{\sigma}_{\mathrm{f}}$ value increases notably. Therefore, it is customary to report one extra digit for spectroscopic

constants. A general solution to this problem has been given by Le Roy [23], and was named "Sequential Rounding and Refitting". In this procedure, the least significant parameter is rounded first at its first significant digit. This parameter is then held fixed, and the fit is repeated for all other parameters. This procedure is repeated iteratively, and the last cycle involves a fit to only one parameter [23]. The sequential rounding and refitting (SRR) technique minimizes the number of digits required to reproduce the experimental data accurately.

Program DParFit [24] written by Le Roy was used to fit the observed vibration-rotation transitions of diatomic hydrides (BeH, MgH, CaH, SrH, ZnH and CdH), and the molecular constants were rounded by the sequential rounding and refitting procedure. The observed transition frequencies of triatomic hydrides (BeH_2, MgH_2, ZnH_2 and HgH_2) were fitted using another least-squares fitting program, and the parameters were rounded with one extra digit. The rounded constants of BeH_2, MgH_2, ZnH_2 and HgH_2 can reproduce the data within the experimental uncertainties.

1.5 References

[1] P.F. Bernath, Chem. Soc. Rev. 25 (1996) 111-115.

[2] P.F. Bernath, Annu. Rep. Prog. Chem., Sect. C 96 (2000) 177-224.

[3] J.D. Kirkpatrick, Annu. Rev. Astron. Astrophys. 43 (2005) 195-245.

[4] P.L. Gay, D. L. Lambert, Astrophys. J. 533 (2000) 260-270.

[5] H. Körsgen, W. Urban, J.M. Brown, J. Chem. Phys. 110 (1999) 3861-3869.

[6] P.F. Bernath, *Spectra of Atoms and Molecules*, 2nd ed., Oxford University Press, New York (2005).

[7] M. Born, R. Oppenheimer, Ann. Physik. 84 (1927) 457-484.

[8] I.M. Mills, in *Molecular Spectroscopy: Modern Research*, ed. K.N. Rao, C.W. Mathews, Academic Press, New York (1972) pp. 115-140.

[9] J.L. Dunham, Phys. Rev. 41 (1932) 721-731.

[10] P.M. Morse, Phys. Rev. 34 (1929) 57-64.

[11] J.L. Dunham, Phys. Rev. 41 (1932) 713-720.

[12] D. Papoušek, M.R. Aliev, *Molecular Vibrational-Rotational Spectra*, Elsevier, Amsterdam (1982).

[13] S.A. Tashkun, V.I. Perevalov, J.-L. Teffo, L.S. Rothman, V.G. Tyuterev, J. Quant. Spectrosc. Radiat. Transfer 60 (1998) 785-801.

[14] G. Blanquet, E. Baeten, I. Cauuet, J. Walrand, C.P. Courtoy, J. Mol. Spectrosc. 112 (1985) 55-70.

[15] S. Yu, A. Shayesteh, P.F. Bernath, J. Koput, J. Chem. Phys. 123 (2005) 134303:1-8.

[16] P.F. Bernath, Annu. Rev. Phys. Chem. 41 (1990) 91-122.

[17] R.J. Bell, *Introductory Fourier Transform Spectroscopy*, Academic Press, New York (1972).

[18] J.E. Bertie, in *Vibrational Spectra and Structure XIV*, ed. J.R. Durig, Elsevier, Amsterdam (1985) pp. 221-253.

[19] P.R. Griffiths, J.A. De Haseth, *Fourier Transform Infrared Spectrometry*, Wiley, New York (1986).

[20] P.R. Griffiths, in *Laboratory Methods in Vibrational Spectroscopy*, ed. H.A. Willis, J.H. van der Maas, R.G.J. Miller, John Wiley & Sons, Chichester (1987) pp. 121-143.

[21] S.P. Davis, M.C. Abrams, J.W. Brault, *Fourier Transform Spectrometry*, Academic Press, San Diego (2001).

[22] A.G. Maki, J.S. Wells, *Wavenumber Calibration Tables from Heterodyne Frequency Measurements*, NIST Special Publication 821, U.S. Government Printing Office, Washington (1991).

[23] R.J. Le Roy, J. Mol. Spectrosc. 191 (1988) 223-231.

[24] R.J. Le Roy, *DParFit 3.0*, A Computer Program for Fitting Multi-Isotopomer Diatomic Molecule Spectra, University of Waterloo Chemical Physics Research Report CP-658 (2004); http://leroy.uwaterloo.ca.

Chapter 2

Infrared Emission Spectra of BeH, MgH, CaH, and SrH

2.1 Introduction

The first laboratory spectra of MgH and CaH free radicals were photographed about a century ago in order to identify strong bands appearing in sunspot spectra [1-4]. MgH and CaH have become important molecules in astrophysics because their visible bands appear strongly in the absorption spectra of the sun and of some stars [5-7]. For example, the green bands of MgH are used routinely to estimate the magnesium isotope abundances in various astronomical objects [8,9]. Most previous experimental work on the alkaline earth monohydrides focused on their electronic spectra. The first series of spectroscopic studies on BeH, MgH, CaH and SrH were carried out in the 1920s and 1930s, shortly after the development of quantum mechanics, and several electronic transitions involving the $X\,^2\Sigma^+$ ground state and the low-lying excited states were observed and analyzed [10-33]. For all alkaline earth monohydride molecules, the strongest bands are from the $A\,^2\Pi - X\,^2\Sigma^+$ system which involves the transition of an unpaired electron between non-bonding π and σ orbitals. A nearly complete summary of the BeH, MgH, CaH and SrH studies prior to 1976 has been compiled by Huber and Herzberg [34].

The visible and ultraviolet spectra of BeH, MgH, CaH and SrH were studied extensively in the 1970s and 1980s using high resolution spectrographs and Fourier transform spectrometers or by laser-induced fluorescence techniques [35-62]. Most of the work on BeH and BeD was carried out by Colin and co-workers [35-41], who identified several excited electronic states and determined rotational constants for high vibrational levels of the $X\,^2\Sigma^+$

ground state. Colin and De Greef [38] also determined a value of 2.03(1) eV for the D_0 dissociation energy of BeH in the ground electronic state (at zero kelvin). The spectra of MgH and MgD were studied mostly by Balfour and co-workers in the 1970s [42-49], and spectroscopic constants for the high vibrational levels of the ground state were obtained. The dissociation energy of MgH in the ground state was determined by Balfour and Lindgren [48] to be 1.27(3) eV. Bernath et al. [50] recorded the $A\ ^2\Pi \rightarrow X\ ^2\Sigma^+$ emission spectrum of MgH at very high resolution using a Fourier transform spectrometer, and predicted highly accurate vibration-rotation and pure rotational transition frequencies for the $X\ ^2\Sigma^+$ ground state of this molecule. The spectra of CaH and CaD were studied in the ultraviolet spectral region, mostly by Kaving and Lindgren [51-54], and several excited electronic states were identified. High resolution visible spectra of CaH were measured by Berg, Klynning and Martin [55-59], and the spectrum of CaD in the red spectral region was reported by Balfour and Klynning [60]. There have been two studies on the visible spectra of SrH and SrD by Appelblad et al. in the 1980s [61,62]. Recently, the visible spectra of BeH/BeD and CaH were re-examined by Focsa et al. [63,64] and Steimle et al. [65,66], respectively.

Diatomic metal hydrides are favourite target molecules for theoretical chemists because of the simplicity of metal-hydrogen bonding. With only five electrons, BeH is one of the smallest diatomic molecules, and is often used to test new ab initio theoretical methods for open-shell systems [67-71]. Parallel to the experimental work on alkaline earth monohydrides, several theoretical studies have been carried out for BeH, MgH, CaH and SrH molecules [71-100]. The equilibrium internuclear distances, vibrational frequencies, dissociation energies and dipole moments of these molecules have been computed by various ab initio theoretical methods, and the experimental assignments of the low-lying excited states have been reconfirmed. Among the numerous ab initio results for the $X\ ^2\Sigma^+$ ground state of these molecules, the molecular parameters of BeH computed by Martin [82] show the best agreement with experiment.

It is only in the past twenty years that the vibration-rotation and pure rotation transitions in the $X\ ^2\Sigma^+$ ground state of some alkaline earth monohydrides have been directly measured [101-114]. Vibration-rotation spectra of MgH, MgD, CaH, CaD, SrH and SrD were recorded in absorption using diode laser infrared spectrometers [101-104]. In addition, the $v = 1 \rightarrow 0$ fundamental bands of CaH and SrH, and the $v = 2 \rightarrow 1$ hot band of CaH were measured by Frum et al. [105,106] using a Fourier transform spectrometer. Pure rotation spectra of MgH,

MgD, CaH, CaD, SrH and SrD in the far-infrared and millimetre-wave spectral regions have been recorded by various research groups [106-112]. However, there were no studies on the vibration-rotation and pure rotation spectra of BeH and BeD.

The investigation of infrared emission spectra of alkaline earth monohydrides in our laboratory was started by searching for the vibration-rotation transitions of BeH and BeD. Infrared emission spectra of BeH and BeD were recorded, and in addition to the metal monohydride molecules, several vibration-rotation bands of the dihydrides, BeH_2 and BeD_2, were observed. There was no previous observation of BeH_2 and BeD_2 molecules in the gas phase, and the only metal dihydride known in the gas phase was FeH_2 [115-117]. Similar experiments were carried out in our laboratory in order to produce the other alkaline earth dihydride molecules, MgH_2, CaH_2, SrH_2 and BaH_2, in the gas phase. However, only MgH_2 and MgD_2 molecules could be generated successfully. In the course of these measurements, new vibration-rotation data were obtained for MgH, MgD, CaH and SrH molecules, which are described in this chapter. The results presented in this chapter have been previously published in Refs. [118-120].

2.2 Experimental Details

The discharge-furnace emission source described in Chapter 1 was used to generate the alkaline earth monohydride molecules, and infrared emission spectra were recorded using a Bruker IFS 120 HR Fourier transform spectrometer.

For the BeH and BeD experiments, about 5 grams of beryllium powder was placed inside a zirconia boat in the central part of the alumina tube. The temperature of the furnace was about 1500°C, and a mixture of helium (about 2 Torr) and hydrogen or deuterium (about 1 Torr) flowed through the cell. The tube was sealed with CaF_2 windows, and a CaF_2 lens was used to focus the emission onto the entrance aperture of the spectrometer. Two infrared emission spectra were recorded for BeH. The first spectrum was recorded with a liquid-nitrogen-cooled HgCdTe (MCT) detector at an instrumental resolution of 0.03 cm^{-1}. The spectral range of this spectrum was limited to the 1200–2200 cm^{-1} by a 2200 cm^{-1} long-wave pass filter and by the transmittance of the CaF_2 beamsplitter used in the spectrometer. The second spectrum of BeH was recorded at the same resolution (0.03 cm^{-1}) with a liquid-nitrogen-cooled InSb detector. The spectral range of the second spectrum was limited to the 1750–2900 cm^{-1} by a 2900 cm^{-1} long-wave pass filter and by the detector response. The infrared emission spectrum of BeD was recorded at exactly the same conditions as the first BeH spectrum. In order to improve the signal-to-noise ratio, 200 scans were co-added for each spectrum in about 3 hours of recording. The signal-to-noise ratios for the strongest lines of BeH and BeD were about 350 and 25, respectively.

For the MgH and MgD experiments, about 50 grams of magnesium (cut from a rod) was placed directly inside the alumina tube, and heated to about 550–650°C. Two infrared emission spectra were recorded for MgH. The first MgH spectrum was obtained at 650°C with 1.6 Torr of argon and 0.9 Torr of hydrogen. CaF_2 lens and windows were used with a CaF_2 beamsplitter along with an MCT detector. The instrumental resolution was 0.01 cm^{-1}, and the spectral range was limited to 1200–2200 cm^{-1} by a 2200 cm^{-1} long-wave pass filter and by the CaF_2 beamsplitter. The signal-to-noise ratio was improved by co-adding 550 scans during 8 hours of recording. The second MgH spectrum (550 scans) was obtained at 550°C with about 1 Torr of pure hydrogen. BaF_2 lens and windows were used with a KBr beamsplitter and an MCT detector. The instrumental resolution was 0.01 cm^{-1}, and the spectral band-pass was set to 800–1700 cm^{-1} by the detector response, the BaF_2 optics, and a

1700 cm^{-1} long-wave pass filter. The infrared spectrum of MgD was recorded at 600°C with about 1 Torr of pure deuterium. All other conditions were the same as those in the second MgH experiment, and in this case 1200 scans were co-added during 18 hours of recording. The signal-to-noise ratios were about 180 and 120 for the strongest lines of MgH and MgD, respectively.

For the CaH and SrH experiments, about 50 grams of calcium or strontium metal was placed inside an alumina boat in the central part of the alumina tube, and heated to 780°C and 850°C, respectively. The alumina tube was sealed with BaF_2 windows, and about 1 Torr of pure hydrogen flowed through the cell. A BaF_2 lens was used to focus the emission from CaH and SrH molecules onto the entrance aperture of the spectrometer. The spectra were recorded using a KBr beamsplitter and an MCT detector at an instrumental resolution of 0.01 cm^{-1}. The spectral range was limited to 800–1700 cm^{-1} by the detector response, the BaF_2 optics, and a 1700 cm^{-1} long-wave pass filter. About 600 scans for CaH and 300 scans for SrH were co-added, and the achieved signal-to-noise ratios for the strongest lines of CaH and SrH were about 50 and 25, respectively.

All spectra contained both atomic and molecular emission lines, as well as blackbody emission from the hot tube and absorption lines from atmospheric water vapour. Overviews of the infrared emission spectra of BeH, BeD, MgH, MgD, CaH and SrH are shown in Figures 2.1 to 2.6, respectively. For some of these spectra, the blackbody emission profile has been subtracted from the original spectrum using the Bruker OPUS software, in order to obtain flat baselines and to display the vibration-rotation bands clearly. In addition to metal monohydride molecules, several vibration-rotation bands of BeH_2, BeD_2, MgH_2 and MgD_2 were observed in the spectra, and their analyses are presented in Chapter 4.

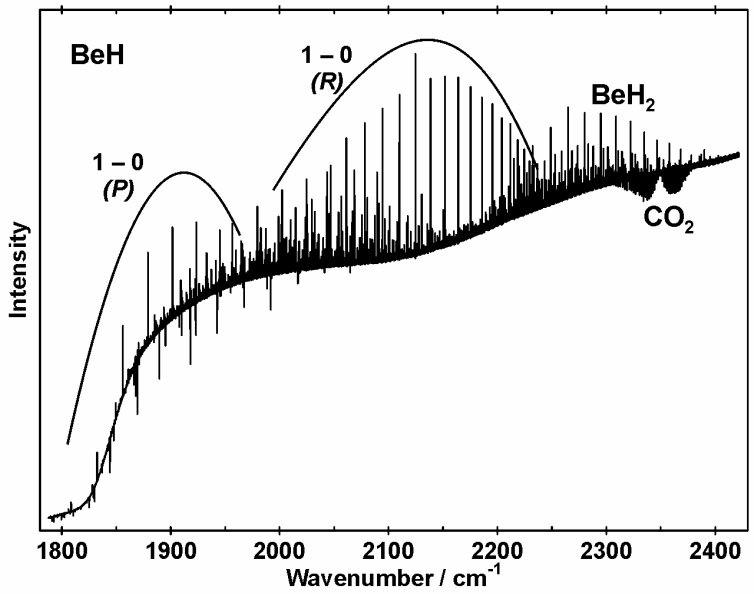

Fig. 2.1. An overview of the infrared emission spectrum of BeH recorded with the InSb detector. Nearly all emission lines above 2240 cm^{-1} are from BeH_2. Absorption lines from atmospheric CO_2 can be seen near 2350 cm^{-1}.

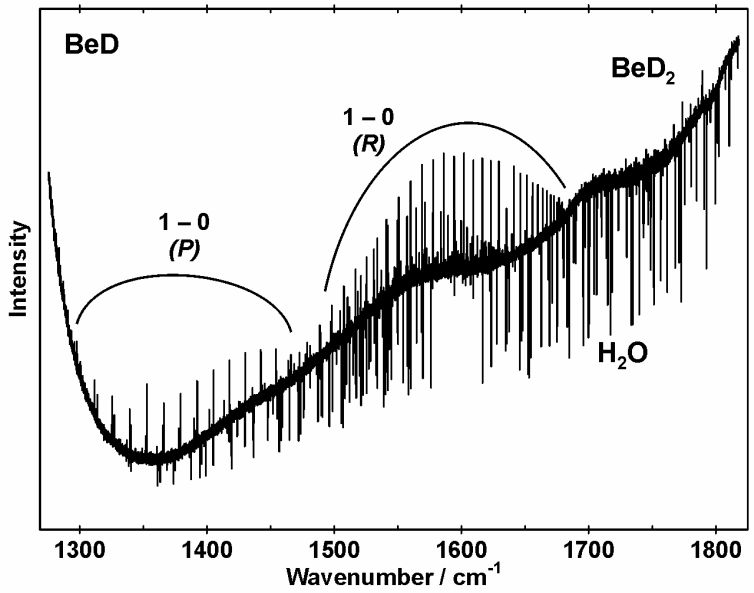

Fig. 2.2. An overview of the infrared emission spectrum of BeD recorded with the MCT detector. The absorption lines are from atmospheric water vapour.

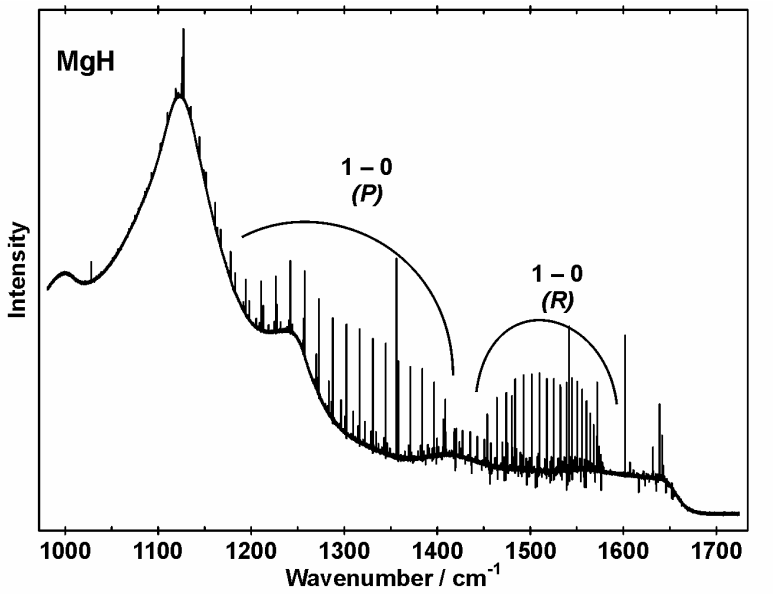

Fig. 2.3. An overview of the infrared emission spectrum of MgH. The absorption lines are from atmospheric water vapour.

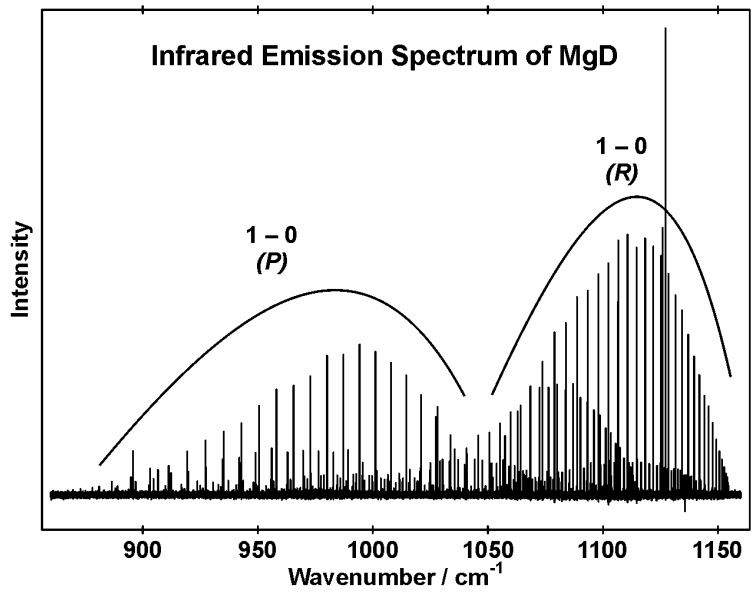

Fig. 2.4. An overview of the infrared emission spectrum of MgD after baseline correction.

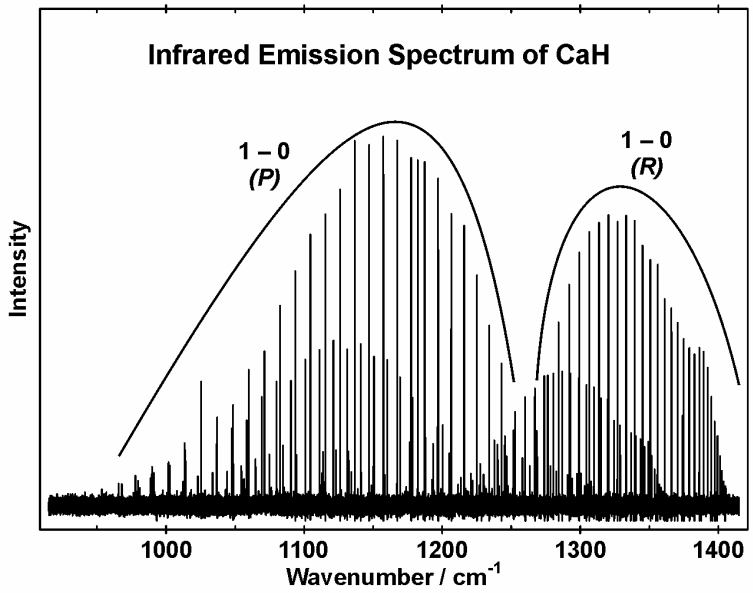

Fig. 2.5. An overview of the infrared emission spectrum of CaH after baseline correction.

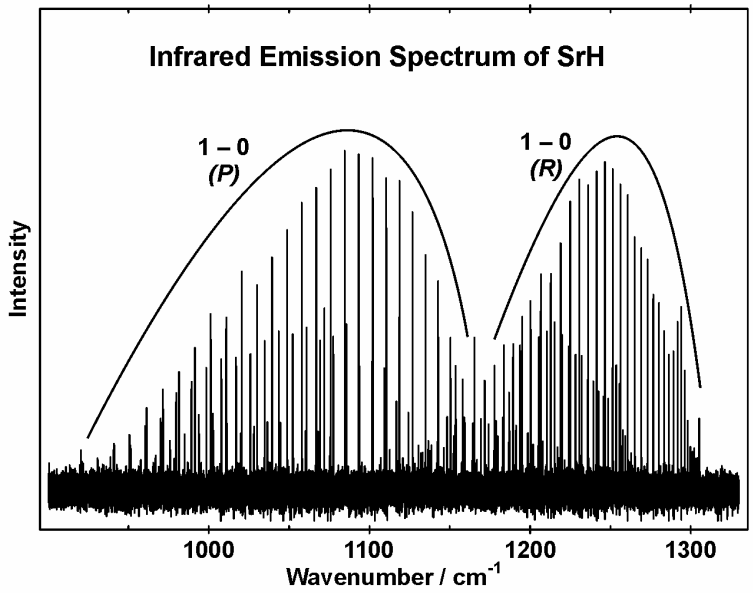

Fig. 2.6. An overview of the infrared emission spectrum of SrH after baseline correction.

2.3 Results and Analyses

Four vibration-rotation bands, v = 1→0, v = 2→1, v = 3→2 and v = 4→3, were observed in emission for the most abundant isotopologues of BeH, BeD, MgH, MgD, CaH, and SrH. In addition, several *R*-branch lines of the v = 5→4 band of ^{24}MgD were found. Fewer bands were detectable for the minor isotopologues of these molecules due to the lower abundances of the metal isotopes. The new infrared emission spectra have substantially extended the available spectroscopic data for the ground electronic states of alkaline earth monohydride molecules. A summary of the observed vibration-rotation bands for all isotopologues, and a comparison with the data from diode laser infrared studies are presented in Table 2.1.

Program WSPECTRA written by Carleer (Université Libre de Bruxelles) was used to measure line positions in the spectra. Molecular emission lines from impurity carbon monoxide appeared near 2100 cm^{-1} in two spectra, i.e., BeH spectrum (1750–2900 cm^{-1}) and MgH spectrum (1200–2200 cm^{-1}), and were used for absolute wavenumber calibration [121]. The spectra of BeD and MgD were then calibrated using several atomic emission lines that were common to both hydride and deuteride spectra. The absolute accuracy of calibrated line positions for BeH, BeD, MgH and MgD is about 0.001 cm^{-1}, and there is no systematic discrepancy between the new MgH/MgD line positions and those measured in diode laser infrared spectra [101]. The spectral range for CaH and SrH molecules was 800–1700 cm^{-1}, and it was therefore not possible to calibrate these spectra with carbon monoxide lines. Both CaH and SrH spectra were calibrated using the line lists of the previous diode laser infrared measurements [102,103], and the absolute accuracy of line positions is about 0.001 cm^{-1}.

The ground electronic state of alkaline earth monohydrides is a $^2\Sigma^+$ state in which the *e* (F_1) and *f* (F_2) spin components are split by spin-rotation interaction, and the magnitude of the spin-rotation interaction constant increases from Be to Sr. Almost all vibration-rotation lines in the SrH spectrum were doubled due to the spin-rotation interaction. In the CaH, MgH, and MgD spectra, all the *P*-branch lines were doubled but the splitting was not resolved for many of the *R*-branch lines. The spin-rotation interaction is very small for the BeH and BeD molecules, and no doublet splitting was observed in their spectra. Expanded views of BeH, MgD, MgH and CaH spectra in Figures 2.7 to 2.10 show the rotational structure, the *R*-branch head, the isotope splitting and the spin doubling, respectively.

Table 2.1. A summary of all vibration-rotation bands used in the analyses.

Molecule	Metal isotope	Natural abundance	New vibration-rotation bands	Bands from diode laser infrared spectra	Ref.
BeH	^{9}Be	100%	v = 1→0 to 4→3	…	
BeD	^{9}Be	100%	v = 1→0 to 4→3	…	
MgH	^{24}Mg	79.0%	v = 1→0 to 4→3	v = 1→0 and 2→1	[101]
MgH	^{25}Mg	10.0%	v = 1→0 to 3→2	v = 1→0 and 2→1	[101]
MgH	^{26}Mg	11.0%	v = 1→0 to 3→2	v = 1→0 and 2→1	[101]
MgD	^{24}Mg	79.0%	v = 1→0 to 5→4	v = 1→0 and 2→1	[101]
MgD	^{25}Mg	10.0%	v = 1→0 to 4→3	v = 1→0 and 2→1	[101]
MgD	^{26}Mg	11.0%	v = 1→0 to 4→3	v = 1→0 and 2→1	[101]
CaH	^{40}Ca	96.9%	v = 1→0 to 4→3	v = 1→0 to 4→3	[102]
CaD	^{40}Ca	96.9%	…	v = 1→0 to 4→3	[102]
SrH	^{88}Sr	82.6%	v = 1→0 to 4→3	v = 1→0 to 3→2	[103]
SrH	^{87}Sr	7.0%	v = 1→0	…	
SrH	^{86}Sr	9.9%	v = 1→0	…	
SrD	^{88}Sr	82.6%	…	v = 1→0 to 3→2	[104]

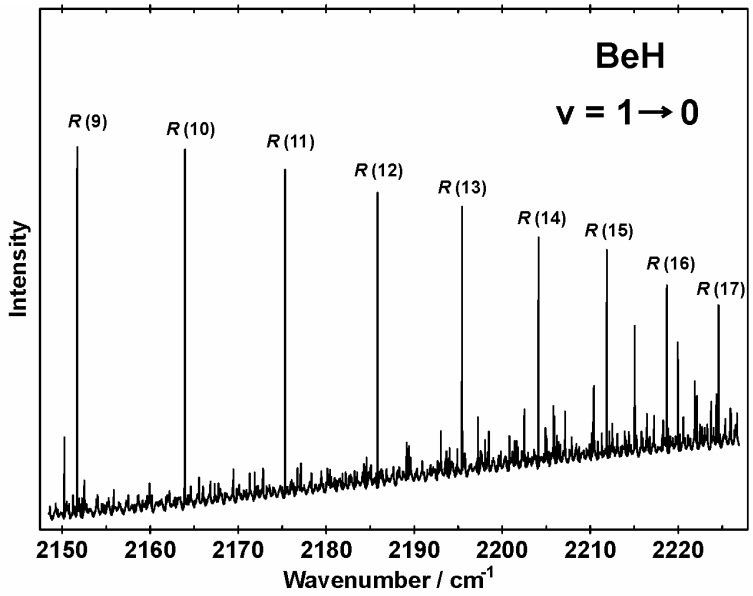

Fig. 2.7. An expanded view of BeH spectrum showing some *R*-branch lines of the v = 1→0 band. The weak lines are from BeH_2.

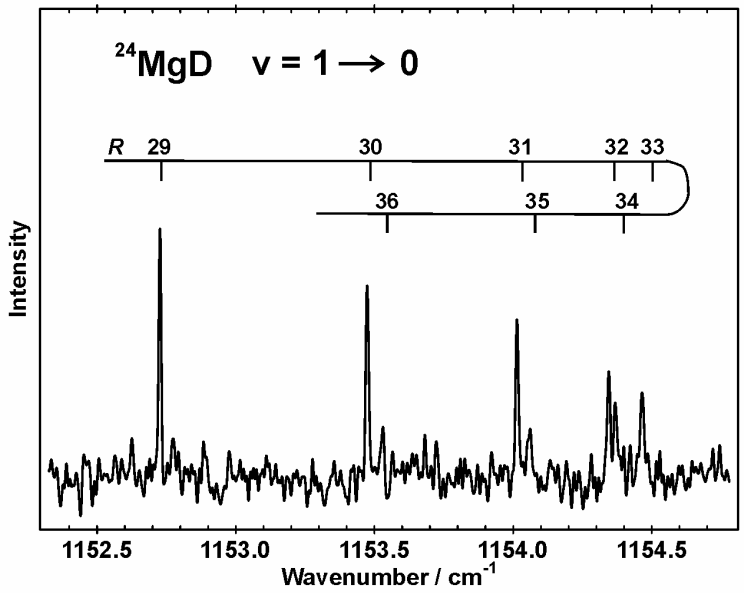

Fig. 2.8. An expanded view of the *R*-branch head in the v = 1→0 band of ^{24}MgD.

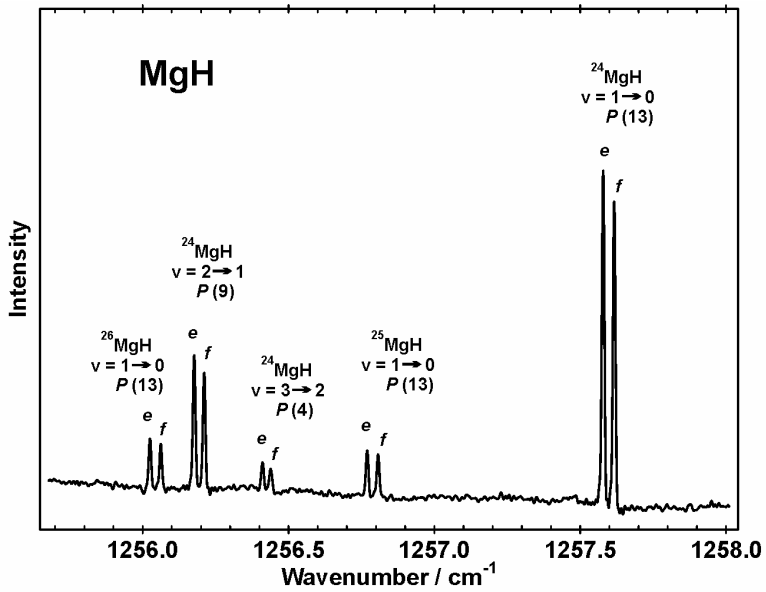

Fig. 2.9. An expanded view of the MgH spectrum showing the isotope splitting and the spin doubling in some *P*-branch lines.

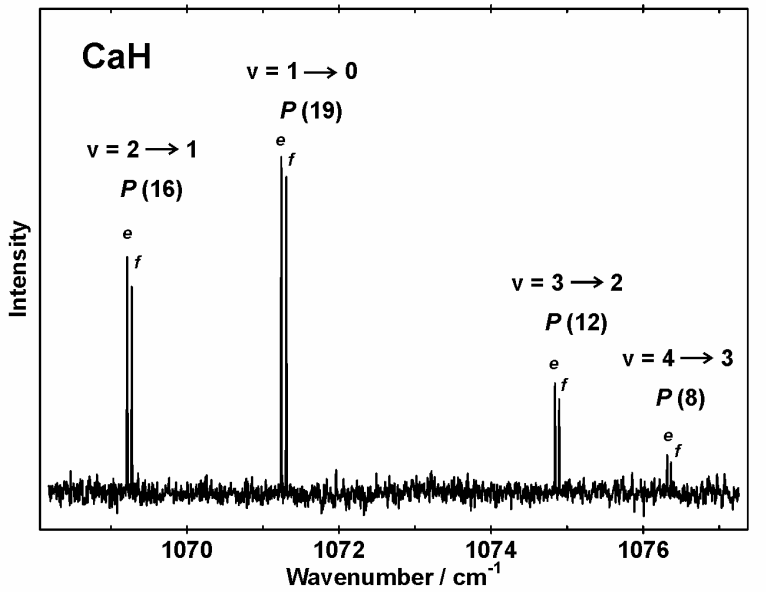

Fig. 2.10. An expanded view of the CaH spectrum showing the spin doubling in all vibration-rotation bands.

Due to the high accuracy of line positions in the pure rotation spectra (~ 10^{-5} cm^{-1}), all the data from pure rotation spectra available in the literature [106-112] were added to the new data set. In all pure rotation spectra, magnetic hyperfine structure arising from the interaction of the H or D nucleus with the unpaired electron was present. In order to combine the pure rotation data properly with the vibration-rotation transitions, it was necessary to calculate the line positions in the absence of hyperfine structure. The hypothetical "hyperfine-free" line positions were calculated from the constants reported in Refs. [106-112], while the hyperfine parameters were set to zero. For completeness, all the data from the diode laser infrared spectra [101-104] were also included in the new data set (see Table 2.1). For all diode laser infrared spectra, the number of rotational lines in each vibration-rotation band was limited due to spectral gaps in the diodes available. For example, only *P*-branch lines were observed in the v = 1←0 and v = 2←1 bands of CaH [102]. Data from the previous Fourier transform infrared spectra of CaH and SrH [105,106] were not added to the new data set, because the signal-to-noise ratios of the new infrared emission spectra for CaH and SrH were significantly larger. Complete lists of all the data used in the analyses have been published in the supplementary tables of Refs. [118-120].

A Hamiltonian operator that includes rotation and spin-rotation interaction terms was used to obtain analytical expressions for the energy levels (see Chapter 1). The rotational energy is expressed as a power series in $N(N+1)$ where N is the rotational angular momentum quantum number for a $^2\Sigma^+$ state, and the degeneracy of the e (F_1) and f (F_2) spin components is lifted due to the spin-rotation interaction. The following energy level expressions in which $x = N(N+1)$ were used for the e ($J = N + ½$) and f ($J = N - ½$) components:

$$E^e_{v,N} = G_v + B_v\, x - D_v\, x^2 + H_v\, x^3 + L_v\, x^4 + ½ N \cdot \left(\gamma_v + \gamma_{D,v} x\right), \qquad (2.1)$$

$$E^f_{v,N} = G_v + B_v\, x - D_v\, x^2 + H_v\, x^3 + L_v\, x^4 - ½ (N+1) \cdot \left(\gamma_v + \gamma_{D,v} x\right). \qquad (2.2)$$

Program DParFit [122] was used to fit the data for all observed vibrational levels of ^{9}BeH, ^{9}BeD, ^{24}MgH, ^{24}MgD, ^{40}CaH and ^{88}SrH, and individual band constants (vibrational energies, rotational constants, centrifugal distortion and spin-rotation interaction constants) were obtained for each vibrational level. Since no *e*/*f* splitting was observed for BeH and BeD, the spin-rotation interaction constants (γ and γ_D in the above equations) were set to zero for these molecules. The band constants of ^{9}BeH, ^{9}BeD, ^{24}MgH, ^{24}MgD, ^{40}CaH and ^{88}SrH are listed in Tables 2.2 to 2.4.

Table 2.2. Band constants (in cm^{-1}) for the $X\,^2\Sigma^+$ ground state of ^{9}BeH and ^{9}BeD.[a]

	^{9}BeH				
	v = 0	v = 1	v = 2	v = 3	v = 4
G_v	0.0	1986.4158(4)	3896.8702(5)	5729.2615(6)	7480.3404(16)
B_v	10.165613(23)	9.855737(21)	9.541635(21)	9.220120(21)	8.886589(46)
$10^4\,D_v$	10.2641(16)	10.1624(14)	10.0982(13)	10.0885(13)	10.1605(34)
$10^8\,H_v$	10.081(39)	9.756(35)	9.327(31)	8.756(30)	7.921(67)
$10^{12}\,L_v$	–11.97(32)	–12.58(28)	–13.68(24)	–16.05(21)	–20.0[b]

	^{9}BeD				
	v = 0	v = 1	v = 2	v = 3	v = 4
G_v	0.0	1488.8426(5)	2936.1897(7)	4341.3758(9)	5703.4618(25)
B_v	5.625285(31)	5.498876(31)	5.371486(32)	5.242539(33)	5.111211(59)
$10^4\,D_v$	3.1290(21)	3.1041(23)	3.0845(24)	3.0729(24)	3.0688(36)
$10^8\,H_v$	1.755(72)	1.716(74)	1.663(72)	1.617(66)	1.516(81)
$10^{12}\,L_v$	–2.06(98)	–1.95(86)	–1.85(74)	–1.90(62)	–1.77(61)

[a] The numbers in parentheses are 2σ uncertainties in the last quoted digits.
[b] Fixed value; this constant was determined by extrapolation of L_v constants for v = 0 to 3.

Table 2.3. Band constants (in cm^{-1}) for the $X\,^2\Sigma^+$ ground state of ^{24}MgH and ^{24}MgD.[a]

	^{24}MgH				
	v = 0	v = 1	v = 2	v = 3	v = 4
G_v	0.0	1431.97778(18)	2800.6770(4)	4102.3284(5)	5331.3869(10)
B_v	5.7365078(4)	5.5552881(5)	5.3675658(79)	5.169804(15)	4.956662(30)
$10^4\,D_v$	3.543234(130)	3.55726(14)	3.60113(53)	3.6895(13)	3.8506(22)
$10^8\,H_v$	1.4537(38)	1.3197(35)	1.107(12)	0.691(38)	–0.28(5)
$10^{12}\,L_v$	–1.38(3)	–1.81(3)	–2.60(8)	–3.6(4)	…
$10^2\,\gamma_v$	2.63897(11)	2.52480(11)	2.401(5)	2.273(8)	2.126(20)
$10^6\,\gamma_{D,v}$	–5.77(10)	–5.79(10)	–5.8(1)	–6.0(3)	–6.0(10)
	^{24}MgD[b]				
	v = 0	v = 1	v = 2	v = 3	v = 4
G_v	0.0	1045.8446(3)	2059.3940(4)	3039.5181(5)	3984.7236(8)
B_v	3.0009455(3)	2.9333697(27)	2.864344(4)	2.793330(7)	2.719587(13)
$10^4\,D_v$	0.961742(130)	0.96251(12)	0.96680(13)	0.97618(22)	0.99172(50)
$10^8\,H_v$	0.1989(15)	0.1787(12)	0.1532(12)	0.123(2)	0.076(5)
$10^2\,\gamma_v$	1.38173(11)	1.338(4)	1.288(8)	1.233(9)	1.19(2)
$10^6\,\gamma_{D,v}$	–1.49(17)	–1.46(15)	–1.2(3)	…	…

[a] The numbers in parentheses are 2σ uncertainties in the last quoted digits.

[b] The following constants were obtained for the v = 5 level of ^{24}MgD: G_5 = 4893.041(6), B_5 = 2.642114(44), and $D_5 = 1.0156(8)\times10^{-4}$ cm^{-1}; the spin-rotation interaction constant γ_5 was set to zero because spin-splitting was not resolved for the v = 5→4 band of ^{24}MgD.

Table 2.4. Band constants (in cm^{-1}) for the $X\,^2\Sigma^+$ ground state of ^{40}CaH and ^{88}SrH.[a]

	^{40}CaH				
	v = 0	v = 1	v = 2	v = 3	v = 4
G_v	0.0	1260.12775(22)	2481.99888(30)	3665.4141(4)	4809.9464(6)
B_v	4.2286902(7)	4.1317220(39)	4.0342454(60)	3.935887(9)	3.836122(12)
$10^4\,D_v$	1.851405(150)	1.84939(19)	1.84957(31)	1.85277(56)	1.86000(64)
$10^8\,H_v$	0.6835(31)	0.6819(32)	0.6774(55)	0.661(13)	0.594(9)
$10^{12}\,L_v$	–0.411(18)	–0.43(2)	–0.47(3)	–0.49(9)	…
$10^2\,\gamma_v$	4.3566(2)	4.211(2)	4.065(4)	3.920(5)	3.777(9)
$10^6\,\gamma_{D,v}$	–5.04(12)	–5.02(13)	–5.02(14)	–5.1(2)	–5.5(3)

	^{88}SrH				
	v = 0	v = 1	v = 2	v = 3	v = 4
G_v	0.0	1172.80311(17)	2311.45036(29)	3415.8717(4)	4485.8394(11)
B_v	3.6334432(16)	3.5531837(17)	3.4726241(50)	3.391531(6)	3.309615(17)
$10^4\,D_v$	1.35664(21)	1.35436(18)	1.35330(27)	1.35282(26)	1.3558(7)
$10^8\,H_v$	0.3959(47)	0.3946(38)	0.3951(50)	0.361(3)	0.346(8)
$10^{12}\,L_v$	–0.152(29)	–0.17(2)	–0.22(3)	…	…
$10^2\,\gamma_v$	12.3991(8)	11.9871(13)	11.580(3)	11.179(5)	10.762(10)
$10^6\,\gamma_{D,v}$	–11.37(13)	–11.23(12)	–11.14(12)	–11.3(2)	–10.7(3)

[a] The numbers in parentheses are 2σ uncertainties in the last quoted digits.

The band constants of Tables 2.3 and 2.4 were sequentially rounded and refitted [123] starting from the highest order parameter of the highest observed vibrational level. This procedure minimizes the number of digits required to accurately reproduce all the data. Since the new data sets for MgH, MgD, CaH and SrH were much more extensive than those used in previous studies, the new band constants are preferred to those reported in Refs. [101-112].

For each molecule, the data from all isotopologues were then combined and fitted simultaneously using Dunham-type energy level expressions [124] modified for $^2\Sigma^+$ states, i.e., the following equations for *e* ($J = N + ½$) and *f* ($J = N – ½$) parities, respectively.

$$E^{e}_{\mathrm{v},N} = \sum_{m=0}\sum_{l=0} Y_{l,m}\left(\mathrm{v}+\tfrac{1}{2}\right)^{l}\left[N(N+1)\right]^{m} + \frac{1}{2}(N)\sum_{m=1}\sum_{l=0}\gamma_{l,m}\left(\mathrm{v}+\tfrac{1}{2}\right)^{l}\left[N(N+1)\right]^{m-1} \qquad (2.3)$$

$$E^{f}_{\mathrm{v},N} = \sum_{m=0}\sum_{l=0} Y_{l,m}\left(\mathrm{v}+\tfrac{1}{2}\right)^{l}\left[N(N+1)\right]^{m} - \frac{1}{2}(N+1)\sum_{m=1}\sum_{l=0}\gamma_{l,m}\left(\mathrm{v}+\tfrac{1}{2}\right)^{l}\left[N(N+1)\right]^{m-1} \qquad (2.4)$$

In Le Roy's formulation of the Born-Oppenheimer breakdown parameters [125] for a diatomic molecule A–B, the Dunham constants for each isotopologue (α) are related to those for a chosen reference isotopologue ($\alpha = 1$) by the following equation:

$$Y^{(\alpha)}_{l,m} = \left\{ Y^{(1)}_{l,m} + \left(\frac{M^{(\alpha)}_{\mathrm{A}} - M^{(1)}_{\mathrm{A}}}{M^{(\alpha)}_{\mathrm{A}}} \right)\delta^{\mathrm{A}}_{l,m} + \left(\frac{M^{(\alpha)}_{\mathrm{B}} - M^{(1)}_{\mathrm{B}}}{M^{(\alpha)}_{\mathrm{B}}} \right)\delta^{\mathrm{B}}_{l,m} \right\} \left(\frac{\mu_1}{\mu_\alpha} \right)^{m+l/2} . \qquad (2.5)$$

In the above equation, $\delta^{\mathrm{A}}_{l,m}$ and $\delta^{\mathrm{B}}_{l,m}$ are the Born-Oppenheimer breakdown correction parameters for atoms A and B, respectively, M_{A} and M_{B} are atomic masses, and μ's are reduced masses. An analogous reduced-mass scaling relationship exists for the spin-rotation interaction constants [126]:

$$\gamma^{(\alpha)}_{l,m} = \gamma^{(1)}_{l,m}\left(\frac{\mu_1}{\mu_\alpha} \right)^{m+l/2} . \qquad (2.6)$$

Program DParFit was used for multi-isotopologue fitting, with the reference isotopologues chosen to be ^{9}BeH, ^{24}MgH, ^{40}CaH and ^{88}SrH. The Dunham constants of the reference isotopologues and the Born-Oppenheimer breakdown correction parameters are presented in Tables 2.5 to 2.8. The sequential rounding and refitting technique [123], starting from the parameter with largest relative uncertainty, has been applied to these constants in order to minimize the number of digits required to reproduce the data accurately. The Dunham constants of ^{9}BeD, ^{24}MgD, ^{40}CaD and ^{88}SrD are derived from those of ^{9}BeH, ^{24}MgH, ^{40}CaH and ^{88}SrH using equations (2.5) and (2.6), and require more digits, as determined by parameter sensitivities [123]. The analogous derived Dunham constants for the minor

isotopologues of MgH and SrH, i.e., ^{25}MgH, ^{26}MgH, ^{25}MgD, ^{26}MgD, ^{87}SrH and ^{86}SrH, are not listed in Tables 2.6 and 2.8, but they can be calculated easily from Eqs. (2.5) and (2.6). Complete lists of all the data used in the analyses, and the Dunham constants for all isotopologues have been published in the supplementary tables of Refs. [118-120]. Note that there are no $\gamma_{l,m}$ constants for BeH in Table 2.5 because the *e*/*f* splitting was not observed for this molecule.

Using the equilibrium rotational constants ($B_e \approx Y_{0,1}$) of ^{9}BeH, ^{24}MgH, ^{40}CaH and ^{88}SrH in Tables 2.5 to 2.8, the associated equilibrium internuclear distances (r_e) of these species were determined to be 1.342424(2) Å, 1.729721(1) Å, 2.002360(1) Å and 2.146057(1) Å, respectively. The r_e distances of ^{9}BeD, ^{24}MgD, ^{40}CaD and ^{88}SrD are expected to be slightly different from those of the corresponding hydrides due to the existence of $\delta_{0,1}^{H}$ correction parameters (see Tables 2.5 to 2.8). Using the derived B_e constants for these isotopologues, r_e distances of 1.341731(2) Å, 1.729157(1) Å, 2.001462(1) Å and 2.145073(1) Å, were obtained for ^{9}BeD, ^{24}MgD, ^{40}CaD and ^{88}SrD, respectively.

Table 2.5. Dunham and Born-Oppenheimer breakdown constants (in cm^{-1}) for the $X\ ^2\Sigma^+$ ground state of ^{9}BeH and ^{9}BeD (all uncertainties are 2σ).

Dunham	^{9}BeH	^{9}BeD	Born-Oppenheimer breakdown	
$Y_{1,0}$	2061.09967(640)	1529.885642	$\delta^H_{1,0}$	1.2117(41)
$Y_{2,0}$	–37.07713(720)	–20.4184359	$\delta^H_{2,0}$	–0.0088(25)
$Y_{3,0}$	–0.1401(35)	–0.0569793	$\delta^H_{3,0}$	0.0013(5)
$Y_{4,0}$	–0.0103(8)	–0.00312296		
$Y_{5,0}$	–0.0030043(640)	–0.000675936		
$Y_{0,1}$	10.31977(3)	5.6883084	$\delta^H_{0,1}$	0.02133(7)
$Y_{1,1}$	–0.3081114(450)	–0.125983629	$\delta^H_{1,1}$	–0.000439(13)
$Y_{2,1}$	–0.000224(44)	–0.000069129	$\delta^H_{2,1}$	–0.000008(3)
$Y_{3,1}$	–0.00042038(1900)	–0.0000945811		
$Y_{4,1}$	0.000018(4)	0.00000300516		
$Y_{5,1}$	–0.00000608(29)	–0.000000753235		
$10^4\ Y_{0,2}$	–10.32836(200)	–3.1429087	$10^4\ \delta^H_{0,2}$	–0.0749(25)
$10^4\ Y_{1,2}$	0.13911(160)	0.031658	$10^4\ \delta^H_{1,2}$	0.0032(4)
$10^4\ Y_{2,2}$	–0.01993(91)	–0.003327376		
$10^4\ Y_{3,2}$	0.0018(3)	0.000222997		
$10^4\ Y_{4,2}$	–0.0005326(260)	–0.0000489622		
$10^8\ Y_{0,3}$	10.264(52)	1.713607		
$10^8\ Y_{1,3}$	–0.419(35)	–0.0519088		
$10^8\ Y_{2,3}$	0.066(9)	0.00606741		
$10^8\ Y_{3,3}$	–0.0199(12)	–0.00135752		
$10^{12}\ Y_{0,4}$	–12.1(4)	–1.11236		
$10^{12}\ Y_{1,4}$	0.7(3)	0.047752		
$10^{12}\ Y_{2,4}$	–0.52(6)	–0.0263225		

Table 2.6. Dunham and Born-Oppenheimer breakdown constants (in cm^{-1}) for the $X\ ^2\Sigma^+$ ground state of ^{24}MgH and ^{24}MgD (all uncertainties are 2σ).

Dunham	^{24}MgH	^{24}MgD	Born-Oppenheimer breakdown	
$Y_{1,0}$	1492.77634(720)	1077.297606	$\delta^{H}_{1,0}$	0.8092(87)
$Y_{2,0}$	–29.84682(800)	–15.5211147	$\delta^{H}_{2,0}$	0.058(8)
$Y_{3,0}$	–0.30481(390)	–0.118386	$\delta^{H}_{3,0}$	–0.02086(270)
$Y_{4,0}$	–0.01580(84)	–0.00389659	$\delta^{H}_{4,0}$	0.00284(32)
$Y_{5,0}$	–0.004642(67)	–0.000907448		
$Y_{0,1}$	5.8255229(82)	3.034343576	$\delta^{H}_{0,1}$	0.0076044(31)
$Y_{1,1}$	–0.1772981(270)	–0.066606603	$\delta^{H}_{1,1}$	–0.000117(2)
$Y_{2,1}$	–0.001229(28)	–0.0003330008		
$Y_{3,1}$	–0.00048579(1200)	–0.0000949654		
$Y_{4,1}$	0.0000370(24)	0.00000521845		
$Y_{5,1}$	–0.000009232(180)	–0.000000939419		
$10^4\ Y_{0,2}$	–3.54557(34)	–0.9624685	$10^4\ \delta^{H}_{0,2}$	–0.0132(2)
$10^4\ Y_{1,2}$	0.01140(92)	0.00222855		
$10^4\ Y_{2,2}$	–0.014237(690)	–0.00200798		
$10^4\ Y_{3,2}$	0.00180(18)	0.000183162		
$10^4\ Y_{4,2}$	–0.0005758(160)	–0.0000422725		
$10^8\ Y_{0,3}$	1.5126(65)	0.213336	$\delta^{Mg}_{1,0}$	–0.018(2)
$10^8\ Y_{1,3}$	–0.1253(130)	–0.0127501	$\delta^{Mg}_{0,1}$	0.000273(8)
$10^8\ Y_{2,3}$	0.0210(78)	0.00154172		
$10^8\ Y_{3,3}$	–0.01507(100)	–0.00079822		
$10^{12}\ Y_{0,4}$	–1.26(4)	–0.0925		
$10^{12}\ Y_{1,4}$	–0.16(7)	–0.008475		
$10^{12}\ Y_{2,4}$	–0.14(3)	–0.0053501		
$10^2\ \gamma_{0,1}$	2.69318(33)	1.401884		
$10^2\ \gamma_{1,1}$	–0.1061(9)	–0.039846		
$10^2\ \gamma_{2,1}$	–0.0041(5)	–0.0011109		
$10^6\ \gamma_{0,2}$	–5.78(10)	–1.566		

Table 2.7. Dunham and Born-Oppenheimer breakdown constants (in cm^{-1}) for the $X\ ^2\Sigma^+$ ground state of ^{40}CaH and ^{40}CaD (all uncertainties are 2σ).

Dunham	^{40}CaH	^{40}CaD	Born-Oppenheimer breakdown	
$Y_{1,0}$	1298.34821(300)	929.893973	$\delta^{H}_{1,0}$	0.7269(10)
$Y_{2,0}$	–19.12286(350)	–9.802826	$\delta^{H}_{2,0}$	0.0038(3)
$Y_{3,0}$	0.014(2)	0.00513914		
$Y_{4,0}$	–0.003328(400)	–0.000874715		
$Y_{5,0}$	–0.000487(33)	–0.00009165		
$Y_{0,1}$	4.2770434(38)	2.19469905	$\delta^{H}_{0,1}$	0.007686(3)
$Y_{1,1}$	–0.0966314(97)	–0.03548718	$\delta^{H}_{1,1}$	–0.000085(7)
$Y_{2,1}$	–0.0001486(57)	–0.0000390573		
$Y_{3,1}$	0.0000000(14)	0.0000000		
$Y_{4,1}$	–0.000007473(130)	–0.00000100698		
$10^4\ Y_{0,2}$	–1.85266(20)	–0.48831	$10^4\ \delta^{H}_{0,2}$	–0.0104(7)
$10^4\ Y_{1,2}$	0.00242(26)	0.00045543		
$10^4\ Y_{2,2}$	0.00013(8)	0.000017517		
$10^4\ Y_{3,2}$	–0.0002429(81)	–0.000234354		
$10^8\ Y_{0,3}$	0.6814(38)	0.0918178		
$10^8\ Y_{1,3}$	0.0077(31)	0.0007429		
$10^8\ Y_{2,3}$	–0.00358(36)	–0.00024731		
$10^{12}\ Y_{0,4}$	–0.40(2)	–0.027633		
$10^{12}\ Y_{1,4}$	–0.03(1)	–0.0014839		
$10^2\ \gamma_{0,1}$	4.4280(8)	2.270122		
$10^2\ \gamma_{1,1}$	–0.1425(18)	–0.052309		
$10^2\ \gamma_{2,1}$	–0.0009(4)	–0.000237		
$10^6\ \gamma_{0,2}$	–5.0(1)	–1.314		

Table 2.8. Dunham and Born-Oppenheimer breakdown constants (in cm^{-1}) for the $X\ ^2\Sigma^+$ ground state of ^{88}SrH and ^{88}SrD (all uncertainties are 2σ).

Dunham	^{88}SrH	^{88}SrD	Born-Oppenheimer breakdown	
$Y_{1,0}$	1206.99399(440)	858.881476	$\delta^{H}_{1,0}$	0.7372(17)
$Y_{2,0}$	–17.1193(50)	–8.662496	$\delta^{H}_{2,0}$	0.0027(5)
$Y_{3,0}$	0.0182(25)	0.00655176		
$Y_{4,0}$	–0.0017(5)	–0.000435343		
$Y_{5,0}$	–0.0003843(440)	–0.000070008		
$Y_{0,1}$	3.6734953(35)	1.86067005	$\delta^{H}_{0,1}$	0.006752(5)
$Y_{1,1}$	–0.0800603(78)	–0.0288356	$\delta^{H}_{1,1}$	–0.000083(7)
$Y_{2,1}$	–0.0000881(56)	–0.000022561		
$Y_{3,1}$	0.0000000(15)	0.0000000		
$Y_{4,1}$	–0.000004459(160)	–0.00000057784		
$10^4\ Y_{0,2}$	–1.35785(23)	–0.348901	$10^4\ \delta^{H}_{0,2}$	–0.0092(11)
$10^4\ Y_{1,2}$	0.00237(16)	0.00043174		
$10^4\ Y_{2,2}$	0.00016(7)	0.000020735		
$10^4\ Y_{3,2}$	–0.000135(8)	–0.0000124452		
$10^8\ Y_{0,3}$	0.3956(52)	0.0512661		
$10^8\ Y_{1,3}$	0.003(2)	0.00027656		
$10^8\ Y_{2,3}$	–0.00202(29)	–0.00013247		
$10^{12}\ Y_{0,4}$	–0.15(3)	–0.009837		
$10^{12}\ Y_{1,4}$	–0.018(8)	–0.0008397		
$10^2\ \gamma_{0,1}$	12.6051(13)	6.37878		
$10^2\ \gamma_{1,1}$	–0.4131(18)	–0.148711		
$10^2\ \gamma_{2,1}$	0.0009(4)	0.00023		
$10^6\ \gamma_{0,2}$	–11.4(2)	–2.919		
$10^6\ \gamma_{1,2}$	0.13(2)	0.02368		

2.4 Discussion

A few Dunham constants for BeH, MgH, CaH and SrH are compared with those determined from the diode laser infrared spectra [101-104] in Table 2.9. Although the constants of CaH/CaD and SrH/SrD reported in Refs. [102,104] were in the form of mass-independent Dunham-type coefficients ($U_{l,m}$ and $\Delta_{l,m}$) formulated by Bunker [127] and Watson [128], it was straightforward to transform them to regular Dunham ($Y_{l,m}$) constants [125]. The new $Y_{l,0}$ coefficients that represent the vibrational energy are different from those reported in Refs. [101–104] because the new data sets were more extensive than the diode laser infrared data, and higher order polynomials were used to fit the vibrational energy. The new B_e constants of MgH, CaH and SrH have much higher precisions than those obtained from diode laser infrared data [101-104], because all the pure rotation data were included in the new data sets. Consequently, the values for internuclear distance (r_e) have been improved significantly. Small differences between the r_e values of metal hydrides and the corresponding deuterides (Table 2.9) are clearly due to the breakdown of the Born-Oppenheimer approximation.

Several Born-Oppenheimer breakdown correction parameters for the hydrogen atom ($\delta^H_{l,m}$) were required in the multi-isotopologue fits. This is not unusual for diatomic hydrides because of their small reduced masses. In most cases, the total number of parameters required to fit the vibrational energies, i.e., $Y_{l,0}$ and $\delta^H_{l,0}$ coefficients, was equal to the total number of observed vibrational intervals. For example, a total of eight vibrational intervals were measured for BeH and BeD, and eight parameters were required to fit the vibrational energies (G_v) of BeH and BeD together: five Dunham constants ($Y_{1,0}$ to $Y_{5,0}$) and three Born-Oppenheimer breakdown constants ($\delta^H_{1,0}$ to $\delta^H_{3,0}$). In our 2003 paper on BeH/BeD, we had chosen to fit the vibrational energies using four Dunham constants ($Y_{1,0}$ to $Y_{4,0}$) and four correction parameters ($\delta^H_{1,0}$ to $\delta^H_{4,0}$). However, we later realized that a higher order polynomial for the Dunham constants ($Y_{l,0}$), which requires fewer Born-Oppenheimer breakdown correction parameters, is a more realistic model for representing the vibrational energies (see the discussions of the following chapter regarding CdH/CdD). For the same reason, the $Y_{l,0}$ constants of CaH/CaD and SrH/SrD in Tables 2.7 and 2.8 differ from those previously published by our group [120]; the order of $Y_{l,0}$ polynomial has now increased and the number of $\delta^H_{l,0}$ correction parameters decreased. The Dunham constants of BeH/BeD, CaH/CaD and SrH/SrD in Tables 2.5, 2.7 and 2.8 are preferred to those reported in Refs.

[118,120]. Rotational and centrifugal distortion constants required fewer correction parameters compared to the vibrational Dunham constants.

The contribution of Born-Oppenheimer breakdown correction parameters to the vibrational energy of metal deuteride isotopologues can be calculated using the following equation.

$$\begin{aligned}\delta G_{\mathrm{v}}^{\mathrm{BOB}}(\mathrm{MD}) &= \sum_{l}\left\{Y_{l,0}^{\mathrm{MD}} - Y_{l,0}^{\mathrm{MH}}\left(\frac{\mu_{\mathrm{MH}}}{\mu_{\mathrm{MD}}}\right)^{l/2}\right\}\cdot\left(\mathrm{v}+\frac{1}{2}\right)^{l} \\ &= \sum_{l}\left\{\left(\frac{M_{\mathrm{D}}-M_{\mathrm{H}}}{M_{\mathrm{D}}}\right)\delta_{l,0}^{\mathrm{H}}\left(\frac{\mu_{\mathrm{MH}}}{\mu_{\mathrm{MD}}}\right)^{l/2}\right\}\cdot\left(\mathrm{v}+\frac{1}{2}\right)^{l}\end{aligned} \tag{2.7}$$

In the above equation, MH and MD represent the metal hydride and deuteride isotopologues, respectively, M_{H} and M_{D} are atomic masses of hydrogen and deuterium, and the $\delta_{l,0}^{\mathrm{H}}$ coefficients are Born-Oppenheimer breakdown correction parameters defined with MH as the reference isotopologue. This correction function is plotted (Figure 2.11) versus the vibrational quantum number (v) of MD for several molecules, i.e., ^{9}BeD, ^{24}MgD, ^{40}CaD, ^{88}SrD, ^{64}ZnD and ^{114}CdD, in their ground electronic states. The Born-Oppenheimer breakdown constants ($\delta_{l,0}^{\mathrm{H}}$) of ^{64}ZnD and ^{114}CdD were taken from the following chapter (Chapter 3). In all cases, the hydride was the reference isotopologue in the associated fit, and the zeroth order (electronic energy) correction $\delta_{0,0}^{\mathrm{H}}$ was set to zero. The analogous contribution of Born-Oppenheimer breakdown parameters to the rotational constants (B_{v}) has also been calculated for these molecules using the following equation,

$$\begin{aligned}\delta B_{\mathrm{v}}^{\mathrm{BOB}}(\mathrm{MD}) &= \sum_{l}\left\{Y_{l,1}^{\mathrm{MD}} - Y_{l,1}^{\mathrm{MH}}\left(\frac{\mu_{\mathrm{MH}}}{\mu_{\mathrm{MD}}}\right)^{1+l/2}\right\}\cdot\left(\mathrm{v}+\frac{1}{2}\right)^{l} \\ &= \sum_{l}\left\{\left(\frac{M_{\mathrm{D}}-M_{\mathrm{H}}}{M_{\mathrm{D}}}\right)\delta_{l,1}^{\mathrm{H}}\left(\frac{\mu_{\mathrm{MH}}}{\mu_{\mathrm{MD}}}\right)^{1+l/2}\right\}\cdot\left(\mathrm{v}+\frac{1}{2}\right)^{l}\end{aligned} \tag{2.8}$$

and the associated plots are presented in Figure 2.12.

The Born-Oppenheimer breakdown correction parameters for metal atoms ($\delta_{l,m}^{\mathrm{M}}$) should be much smaller than the $\delta_{l,m}^{\mathrm{H}}$ coefficients, because of the large masses of the metal atoms. Although data from two minor isotopes of strontium were included in the data set, no correction parameter was required for the Sr atom ($\delta_{l,m}^{\mathrm{Sr}} = 0$). On the other hand, due to the high quality of the data for MgH isotopologues, two Born-Oppenheimer breakdown correction parameters for the magnesium atom ($\delta_{1,0}^{\mathrm{Mg}}$ and $\delta_{0,1}^{\mathrm{Mg}}$) were determined (see Table

2.6). Although the relative magnitudes of $\delta_{1,0}^{Mg}$ and $\delta_{0,1}^{Mg}$ are small, their presence implies that the simple reduced-mass scaling relationship is not exactly correct for the ω_e and B_e constants, even within different isotopes of magnesium, ^{24}Mg, ^{25}Mg and ^{26}Mg. The reduced-mass scaling ratio of Eq. (2.6) for the spin-rotation interaction constants ($\gamma_{l,m}$) fully accounted for their isotopologue dependence, and no mass-scaled correction parameter was required for the spin-rotation interaction constants.

Table 2.9. Comparison of the Dunham constants for BeH, MgH, CaH and SrH.

Constant	^{9}BeH	^{9}BeD
$Y_{1,0}$ (cm^{-1})	2061.100(6)	1529.886(4)
$Y_{2,0}$ (cm^{-1})	–37.077(7)	–20.418(4)
$Y_{3,0}$ (cm^{-1})	–0.140(4)	–0.057(2)
$Y_{4,0}$ (cm^{-1})	–0.0103(8)	–0.0031(2)
$Y_{5,0}$ (cm^{-1})	–0.00300(6)	–0.00068(2)
B_e (cm^{-1})	10.31977(3)	5.68831(2)
r_e (Å)	1.342424(2)	1.341731(2)

Constant	^{24}MgH	^{24}MgH, Ref. [101]	^{24}MgD	^{24}MgD, Ref. [101]
$Y_{1,0}$ (cm^{-1})	1492.776(7)	1495.263(4)	1077.298(5)	1078.140(2)
$Y_{2,0}$ (cm^{-1})	–29.847(8)	–31.641(2)	–15.521(4)	–16.1474(5)
$Y_{3,0}$ (cm^{-1})	–0.305(4)	…	–0.118(1)	…
$Y_{4,0}$ (cm^{-1})	–0.0158(8)	…	–0.0039(2)	…
$Y_{5,0}$ (cm^{-1})	–0.00464(7)	…	–0.00091(1)	…
B_e (cm^{-1})	5.825523(8)	5.824801(34)	3.034344(4)	3.034178(12)
r_e (Å)	1.729721(1)	1.729828(4)	1.729157(1)	1.729204(4)

Constant	^{40}CaH	^{40}CaH, Ref. [102]	^{40}CaD	^{40}CaD, Ref. [102]
$Y_{1,0}$ (cm^{-1})	1298.348(3)	1298.400(20)	929.894(2)	929.931(13)
$Y_{2,0}$ (cm^{-1})	–19.123(4)	–19.184(8)	–9.803(2)	–9.834(4)
$Y_{3,0}$ (cm^{-1})	0.014(2)	0.044(2)	0.0051(7)	0.0161(6)
$Y_{4,0}$ (cm^{-1})	–0.0033(4)	–0.0096(2)	–0.0009(1)	–0.00253(5)
$Y_{5,0}$ (cm^{-1})	–0.00049(3)	…	–0.000092(6)	…
B_e (cm^{-1})	4.277043(4)	4.277017(488)	2.194699(2)	2.194644(220)
r_e (Å)	2.002360(1)	…	2.001462(1)	…

Constant	^{88}SrH	^{88}SrH, Ref. [104]	^{88}SrD	^{88}SrD, Ref. [104]
$Y_{1,0}$ (cm^{-1})	1206.994(4)	1206.887(10)	858.881(3)	858.862(5)
$Y_{2,0}$ (cm^{-1})	–17.119(5)	–17.025(8)	–8.662(3)	–8.644(3)
$Y_{3,0}$ (cm^{-1})	0.018(3)	–0.012(3)	0.0066(9)	0.00034(46)
$Y_{4,0}$ (cm^{-1})	–0.0017(5)	…	–0.0004(2)	…
$Y_{5,0}$ (cm^{-1})	–0.00038(4)	…	–0.000070(8)	…
B_e (cm^{-1})	3.673495(4)	3.673497(118)	1.860670(2)	1.860627(47)
r_e (Å)	2.146057(1)	…	2.145073(1)	…

[a] The numbers in parentheses are 2σ uncertainties in the last quoted digits.

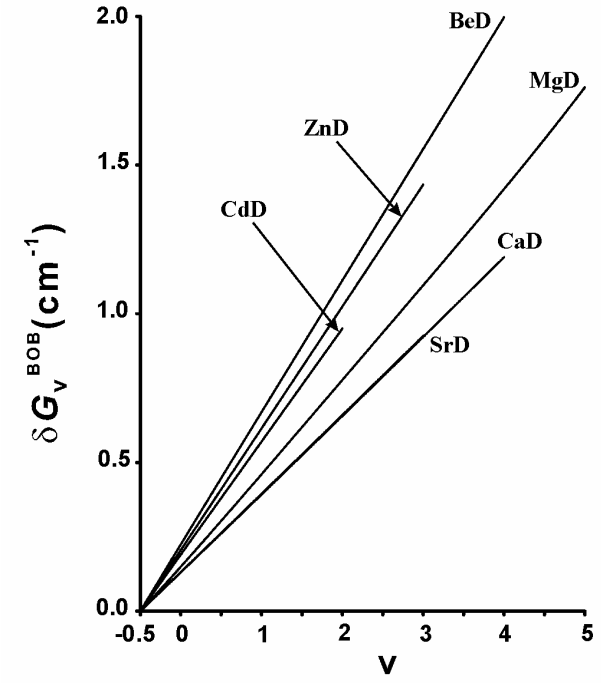

Figure 2.11. The contribution of Born-Oppenheimer breakdown correction parameters to the vibrational energies (G_v) of ^{9}BeD, ^{24}MgD, ^{40}CaD, ^{88}SrD, ^{64}ZnD and ^{114}CdD in their ground electronic states, calculated from Eq. (2.7) and plotted versus the vibrational quantum number of these species. In all cases, the associated fit used the corresponding hydride as the reference isotopologue.

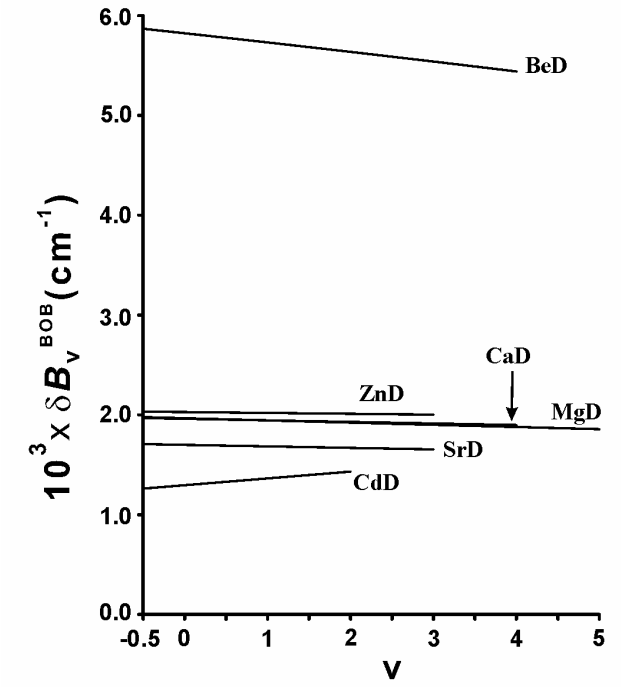

Figure 2.12. The contribution of Born-Oppenheimer breakdown correction parameters to the rotational constants (B_v) of ^{9}BeD, ^{24}MgD, ^{40}CaD, ^{88}SrD, ^{64}ZnD and ^{114}CdD in their ground electronic states, calculated from Eq. (2.8) and plotted versus the vibrational quantum number of these species. In all cases, the associated fit used the corresponding hydride as the reference isotopologue.

2.5 Summary

High-resolution infrared emission spectra of BeH, BeD, MgH, MgD, CaH and SrH were recorded with a Fourier transform spectrometer, and several vibration-rotation bands, v = 1→0 to v = 4→3, were observed in the $X\,^2\Sigma^+$ ground electronic state. The new data were combined with all the previous ground-state data from diode laser infrared spectra and pure rotation spectra available in the literature. Individual band constants were determined for each observed vibrational level by least-squares fitting of all the data. In addition, the data from all isotopologues were fitted together using a Dunham-type energy level expression for $^2\Sigma^+$ states, and Born-Oppenheimer breakdown correction parameters were obtained. Using the equilibrium rotational constants (B_e), the associated equilibrium internuclear distances (r_e) were determined. The equilibrium internuclear distances of ^{9}BeH, ^{24}MgH, ^{40}CaH and ^{88}SrH are 1.342424(2) Å, 1.729721(1) Å, 2.002360(1) Å and 2.146057(1) Å, respectively, while the corresponding r_e distances for ^{9}BeD, ^{24}MgD, ^{40}CaD and ^{88}SrD are 1.341731(2) Å, 1.729157(1) Å, 2.001462(1) Å and 2.145073(1) Å, respectively.

2.6 References

[1] A. Fowler, Mon. Not. R. Astron. Soc. 67 (1907) 530-534.

[2] C.M. Olmsted, Astrophys. J. 27 (1908) 66-69.

[3] A. Fowler, Phil. Trans. R. Soc. London A, 209 (1909) 447-478.

[4] A. Eagle, Astrophys. J. 30 (1909) 231-236.

[5] P. Sotirovski, Astron. Astrophys. Suppl. 6 (1972) 85-115.

[6] L. Wallace, K. Hinkle, G. Li, P.F. Bernath, Astrophys. J. 524 (1999) 454-461.

[7] J. D. Kirkpatrick, Annu. Rev. Astron. Astrophys. 43 (2005) 195-245.

[8] A.M. Boesgaard, Astrophys. J. 154 (1968) 185-190.

[9] P.L. Gay, D.L. Lambert, Astrophys. J. 533 (2000) 260-270.

[10] W.W. Watson, Phys. Rev. 32 (1928) 600-606.

[11] W.W. Watson, A. E. Parker, Phys. Rev. 37 (1931) 167-175.

[12] E. Olsson, Z. Physik. 73 (1932) 732-746.

[13] P.G. Koontz, Phys. Rev. 48 (1935) 707-713.

[14] W.W. Watson, R. F. Humphreys, Phys. Rev. 52 (1937) 318-321.

[15] W.W. Watson, P. Rudnick, Astrophys. J. 63 (1926) 20-32.

[16] W.W. Watson, P. Rudnick, Phys. Rev. 29 (1927) 413-418.

[17] R.S. Mulliken, Phys. Rev. 32 (1928) 388-416.

[18] R.W.B. Pearse, Proc. Roy. Soc. A. 122 (1928) 442-455.

[19] Y. Fujioka, Y. Tanaka, Sci. Pap. Inst. Phys. Chem. Res. 30 (1936) 121-137.

[20] B. Grundstrőm, Nature 137 (1936) 108-109.

[21] A. Guntsch, Z. Physik. 104 (1937) 584-591.

[22] L.A. Turner, W.T. Harris, Phys. Rev. 52 (1937) 626-631.

[23] A. Guntsch, Z. Physik. 107 (1937) 420-424.

[24] R.S. Mulliken, Phys. Rev. 25 (1925) 509-522.

[25] E. Hulthèn, Phys. Rev. 29 (1927) 97-111.

[26] R.S. Mulliken, A. Christy, Phys. Rev. 38 (1931) 87-119.

[27] W.W. Watson, Phys. Rev. 47 (1935) 27-32.

[28] W.W. Watson, R.L. Weber, Phys. Rev. 48 (1935) 732-734.

[29] W.W. Watson, W.R. Fredrickson, Phys. Rev. 39 (1932) 765-776.

[30] W.R. Fredrickson, M.E. Hogan, Jr., W.W. Watson, Phys. Rev. 48 (1935) 602-606.

[31] W.W. Watson, W.R. Fredrickson, M.E. Hogan, Jr., Phys. Rev. 49 (1936) 150-155.

[32] R.F. Humphreys, W.R. Fredrickson, Phys. Rev. 50 (1936) 542-545.

[33] K.R. More, S.D. Cornell, Phys. Rev. 53 (1938) 806-811.

[34] K.P. Huber, G. Herzberg, *Molecular Spectra and Molecular Structure IV. Constants of Diatomic Molecules*, Van Nostrand, New York (1979).

[35] R. Horne, R. Colin, Bull. Soc. Chim. Belges. 81 (1972) 93-107.

[36] R. Colin, D. De Greef, P. Goethals, G. Verhaegen, Chem. Phys. Lett. 25 (1974) 70-73.

[37] D. De Greef, R. Colin, J. Mol. Spectrosc. 53 (1974) 455-465.

[38] R. Colin, D. De Greef, Can. J. Phys. 53 (1975) 2142-2169.

[39] H. Lefebvre-Brion, R. Colin, J. Mol. Spectrosc. 65 (1977) 33-45.

[40] R. Colin, C. Dreze, M. Steinhauer, Can. J. Phys. 61 (1983) 641-655.

[41] C. Clerbaux, R. Colin, Mol. Phys. 72 (1991) 471-486.

[42] W.J. Balfour, Astrophys. J. 162 (1970) 1031-1035.

[43] W.J. Balfour, J. Phys. B: Atom. Mol. Phys. 3 (1970) 1749-1756.

[44] W.J. Balfour, H.M. Cartwright, Chem. Phys. Lett. 32 (1975) 82-85.

[45] W.J. Balfour, H.M. Cartwright, Can. J. Phys. 53 (1975) 1477-1482 .

[46] W.J. Balfour, H.M. Cartwright, Can. J. Phys. 54 (1976) 1898-1904.

[47] W.J. Balfour, H.M. Cartwright, Astron. Astrophys. Suppl. 26 (1976) 389-397.

[48] W.J. Balfour, B. Lindgren, Can. J. Phys. 56 (1978) 767-779.

[49] W.J. Balfour, J. Mol. Spectrosc. 79 (1980) 507-511.

[50] P.F. Bernath, J.H. Black, J.W. Brault, Astrophys. J. 298 (1985) 375-381.

[51] B. Kaving, B. Lindgren, D.A. Ramsay, Phys. Scr. 10 (1974) 73-79.

[52] B. Kaving, B. Lindgren, Phys. Scr. 10 (1974) 81-85.

[53] B. Kaving, B. Lindgren, Phys. Scr. 13 (1976) 39-46.

[54] B. Kaving, B. Lindgren, Phys. Scr. 24 (1981) 752-754.

[55] L.-E. Berg, L. Klynning, Astron. Astrophys. Suppl. 13 (1974) 325-344.

[56] L.-E. Berg, L. Klynning, Phys. Scr. 10 (1974) 331-336.

[57] L.-E. Berg, L. Klynning, H. Martin, Opt. Commun. 17 (1976) 320-324.

[58] H. Martin, J. Mol. Spectrosc. 108 (1984) 66-81.

[59] H. Martin, J. Chem. Phys. 88 (1988) 1797-1806.

[60] W.J. Balfour, L. Klynning, Astrophys. J. 424 (1994) 1049-1053.

[61] O. Appelblad, R.F. Barrow, Phys. Scr. 29 (1984) 456-463.

[62] O. Appelblad, L. Klynning, J.W.C. Johns, Phys. Scr. 33 (1986) 415-419.

[63] C. Focsa, S. Firth, P.F. Bernath, R. Colin, J. Chem. Phys. 109 (1998) 5795-5802.

[64] C. Focsa, P.F. Bernath, R. Mitzner, R. Colin, J. Mol. Spectrosc. 192 (1998) 348-358

[65] T.C. Steimle, J. Gengler, J. Chen, Can. J. Chem. 82 (2004) 779-790.

[66] T.C. Steimle, J. Chen, J. Gengler, J. Chem. Phys. 121 (2004) 829-834.

[67] A.A. Svidzinsky, M.O. Scully, D.R. Herschbach, Proc. Natl. Acad. Sci. USA 102 (2005) 11985-11988.

[68] A.A. Svidzinsky, M.O. Scully, D.R. Herschbach, Phys. Rev. Lett. 95 (2005) 080401:1-4.

[69] R. Martinazzo, A. Famulari, M. Raimondi, E. Bodo, F.A. Gianturco, J. Chem. Phys. 115 (2001) 2917-2925.

[70] P.G. Szalay, J. Gauss, J. Chem. Phys. 112 (2000) 4027-4036.

[71] X. Li, J. Paldus, J. Chem. Phys. 102 (1995) 2013-2023.

[72] H.E. Popkie, J. Chem. Phys. 54 (1971) 4597-4605.

[73] P.S. Bagus, C.M. Moser, P. Goethals, G. Verhaegen, J. Chem. Phys. 58 (1973) 1886-1897.

[74] W. Meyer, P. Rosmus, J. Chem. Phys. 63 (1975) 2356-2375.

[75] D.L. Cooper, J. Chem. Phys. 80 (1984) 1961-1963.

[76] C. Henriet, G. Verhaegen, J. Mol. Struct. (Theochem) 107 (1984) 63-73.

[77] M. Larsson, J. Chem. Phys. 81 (1984) 6409-6410.

[78] M. Larsson, Phys. Scr. 32 (1985) 97-102.

[79] C. Henriet, G. Verhaegen, Phys. Scr. 33 (1986) 299-309.

[80] I.D. Petsalaskis, G. Theodorakopoulos, C.A. Nicolaides, J. Chem. Phys. 97 (1992) 7623-7628.

[81] J.M.L. Martin, Chem. Phys. Lett. 273 (1997) 98-106.

[82] J.M.L. Martin, Chem. Phys. Lett. 283 (1998) 283-293.

[83] F.B.C. Machado, O. Roberto-Neto, F.R. Ornellas, Chem. Phys. Lett. 305 (1999) 156-162.

[84] A.C.H. Chan, E.R. Davidson, J. Chem. Phys. 52 (1970) 4108-4121.

[85] M.L. Sink, A.D. Bandrauk, W.H. Henneker, H. Lefebvre-Brion, G. Raseev, Chem. Phys. Lett. 39 (1976) 505-510.

[86] R.P. Saxon, K. Kirby, B. Liu, J. Chem. Phys. 69 (1978) 5301-5309.

[87] K. Kirby, R.P. Saxon, B. Liu, Astrophys. J. 231 (1979) 637-641.

[88] M.L. Sink, A.D. Bandrauk, Can. J. Phys. 57 (1979) 1178-1184.

[89] P.F. Weck, A. Schweitzer, P.C. Stancil, P.H. Hauschildt, K. Kirby, Astrophys. J. 582 (2003) 1059-1065.

[90] P.F. Weck, P.C. Stancil, K. Kirby, Astrophys. J. 582 (2003) 1263-1268.

[91] P.F. Weck, A. Schweitzer, P.C. Stancil, P.H. Hauschildt, and K. Kirby, Astrophys. J. 584 (2003) 459-464.

[92] S. Skory, P.F. Weck, P.C. Stancil, K. Kirby, Astrophys. J. Suppl. Ser. 148 (2003) 599-606.

[93] N. Honjou, M. Takagi, M. Makita, K. Ohno, J. Phys. Soc. Japan 50 (1981) 2095-2100.

[94] P. Fuentealba, O. Reyes, H. Stoll, H. Preuss, J. Chem. Phys. 87 (1987) 5338-5345.

[95] A. Boutalib, J.P. Daudey, M. El Mouhtadi, Chem. Phys. 167 (1992) 111-120.

[96] T. Leininger, G.-H. Jeung. Phys. Rev. A. 49 (1994) 2415-2420.

[97] T. Leininger, G.-H. Jeung, J. Chem. Phys. 103 (1995) 3942-3949.

[98] H. Uehara, J. Mol. Spectrosc. 192 (1998) 417-423.

[99] C. Carslund-Levin, N. Elander, A. Nunez, A. Scrinzi, Phys. Scr. 65 (2002) 306-322.

[100] P.F. Weck, P.C. Stancil, K. Kirby, J. Chem. Phys. 118 (2003) 9997-10005.

[101] B. Lemoine, C. Demuynck, J.L. Destombes, P.B. Davies, J. Chem. Phys. 89 (1988) 673-677.

[102] D. Petitprez, B. Lemoine, C. Demuynck, J.L. Destombes, B. Macke, J. Chem. Phys. 91 (1989) 4462-4467.

[103] U. Magg, H. Birk, H. Jones, Chem. Phys. Lett. 151 (1988) 263-266.

[104] H. Birk, R.-D. Urban, P. Polomsky, H. Jones, J. Chem. Phys. 94 (1991) 5435-5442.

[105] C.I. Frum, H.M. Pickett, J. Mol. Spectrosc. 159 (1993) 329-336.

[106] C.I. Frum, J.J. Oh, E.A. Cohen, H.M. Pickett, J. Mol. Spectrosc. 163 (1994) 339-348.

[107] K.R. Leopold, L.R. Zink, K.M. Evenson, D.A. Jennings, M. Mizushima, J. Chem. Phys. 84 (1986) 1935-1937.

[108] L.R. Zink, Ph.D. Thesis, University of Colorado (1986).

[109] L.R. Zink, D.A. Jennings, K.M. Evenson, K.R. Leopold, Astrophys. J. 359 (1990) L65-L66.

[110] C.I. Frum, J.J. Oh, E.A. Cohen, H.M. Pickett, Astrophys. J. 408 (1993) L61-L64.

[111] L.M. Ziurys, W.L. Barclay, Jr., and M.A. Anderson, Astrophys. J. 402 (1993) L21-L24.

[112] W.L. Barclay, Jr., M.A. Anderson, L.M. Ziurys, Astrophys. J. 408 (1993) L65-L67.

[113] U. Magg, H. Birk, H. Jones, Chem. Phys. Lett. 149 (1988) 321-325.

[114] K.A. Walker, H.G. Hedderich, P.F. Bernath, Mol. Phys. 78 (1993) 577-589.

[115] H. Körsgen, P. Mürtz, K. Lipus, W. Urban, J.P. Towle, J.M. Brown, J. Chem. Phys. 104 (1996) 4859-4861.

[116] H. Körsgen, K.M. Evenson, J.M. Brown, J. Chem. Phys. 107 (1997) 1025-1027.

[117] H. Körsgen, W. Urban, J.M. Brown, J. Chem. Phys. 110 (1999) 3861-3869.

[118] A. Shayesteh, K. Tereszchuk, P.F. Bernath, R. Colin, J. Chem. Phys. 118 (2003) 1158-1161.

[119] A. Shayesteh, D.R.T. Appadoo, I. Gordon, R.J. Le Roy, P.F. Bernath, J. Chem. Phys. 120 (2004) 10002-10008.

[120] A. Shayesteh, K.A. Walker, I. Gordon, D.R.T. Appadoo, P.F. Bernath, J. Mol. Struct. 695/696 (2004) 23-37.

[121] A.G. Maki, J.S. Wells, *Wavenumber Calibration Tables from Heterodyne Frequency Measurements*, NIST Special Publication 821, U.S. Government Printing Office, Washington (1991).

[122] R.J. Le Roy, DParFit 3.0, A Computer Program for Fitting Multi-Isotopomer Diatomic Molecule Spectra, University of Waterloo Chemical Physics Research Report CP-658 (2004); http://leroy.uwaterloo.ca.

[123] R.J. Le Roy, J. Mol. Spectrosc. 191 (1988) 223-231.

[124] J.L. Dunham, Phys. Rev. 41 (1932) 721-731.

[125] R.J. Le Roy, J. Mol. Spectrosc. 194 (1999) 189-196.

[126] J.M. Brown, J.K.G. Watson, J. Mol. Spectrosc. 65 (1977) 65-74.

[127] P.R. Bunker, J. Mol. Spectrosc. 68 (1977) 367-371.

[128] J.K.G. Watson, J. Mol. Spectrosc. 80 (1980) 411-421.

Chapter 3

Infrared Emission Spectra of ZnH and CdH

3.1 Introduction

The ZnH and CdH molecules were first observed in the 1920s through their electronic spectra in the visible/near-ultraviolet region [1-7], their identification being primarily based on the large line spacings [2] and the isotope effects [3]. Rotational analyses of the spectra by Mulliken and Hulthén [5-7] resulted in spectroscopic constants for the $X\,^2\Sigma^+$ ground state and the $A\,^2\Pi$ excited state of each species. Further investigations were undertaken in the 1930s, and two electronic transitions, $A\,^2\Pi \rightarrow X\,^2\Sigma^+$ and $B\,^2\Sigma^+ \rightarrow X\,^2\Sigma^+$, were studied in detail [8-16]. The most complete analyses of the *A*-*X* and *B*-*X* bands of ZnH and CdH were performed by Stenvinkel [11] and Svensson [12], respectively. The 0-0 bands of the $A\,^2\Pi \rightarrow X\,^2\Sigma^+$ transitions of ZnD and CdD were analyzed by Fujioka and Tanaka [13] and Deile [14], respectively. The absorption spectra of ZnH, ZnD, CdH and CdD in the far-ultraviolet region were analyzed by Khan [17,18], and a new electronic transition, $C\,^2\Sigma^+ \leftarrow X\,^2\Sigma^+$, was assigned for these molecules. Huber and Herzberg [19] compiled a nearly complete summary of the ZnH and CdH studies prior to 1975.

The $A\,^2\Pi \rightarrow X\,^2\Sigma^+$ and $B\,^2\Sigma^+ \rightarrow X\,^2\Sigma^+$emission spectra of ZnD and CdD were recorded by Balfour and co-workers in the 1980s [20-23], and several vibrational bands were analyzed. The molecules were generated in an arc source, and the spectra were recorded by classical spectrographs. Balfour's data spanned the v = 0 to 3 levels of the $X\,^2\Sigma^+$ ground states of ZnD and CdD. A few years later, O'Brien et al. [24] measured the 0-0 band of the $A\,^2\Pi \rightarrow X\,^2\Sigma^+$ system of ZnD at high resolution using a hollow cathode discharge lamp and a Fourier

transform spectrometer. The equilibrium internuclear distances, vibrational frequencies, dissociation energies and dipole moments of the ZnH and CdH molecules have been computed in several ab initio theoretical studies [25-29]. These calculations further confirmed the experimental assignments of the $A\ ^2\Pi$, $B\ ^2\Sigma^+$ and $C\ ^2\Sigma^+$ states [27-29]. Of astrophysical interest, Wojslaw and Peery [30] claim to have detected some branches of the 0-0 and 1-0 bands of the *A*-*X* system of ZnH in the absorption spectrum of the star 19 Piscium.

Zinc and cadmium have several naturally-abundant isotopes, and high resolution spectra of ZnH, ZnD, CdH and CdD are valuable for studying small isotope effects due to both metal and hydrogen atoms. The only previous high resolution infrared spectra of zinc and cadmium monohydrides are those obtained by Jones and co-workers [31,32]. They used a diode-laser infrared spectrometer and observed the v = 1←0 and v = 2←1 bands of ZnH, ZnD, CdH and CdD in the $X\ ^2\Sigma^+$ ground state. However, the number of rotational lines observed in each band was limited by the spectral ranges of the diodes available. Millimeter-wave and far-infrared spectra of ZnH and ZnD were obtained by Goto et al. [33] and Tezcan et al. [34], respectively, and several rotational lines in the v = 0 level of the $X\ ^2\Sigma^+$ ground state were measured. Recently, Varberg and Roberts [35] recorded the far-infrared spectra of CdH and CdD, and observed rotational transitions in the v = 0 level of the $X\ ^2\Sigma^+$ ground state. They performed a multi-isotopologue fit to their data, but overlooked the vibrational dependence of the rotational and spin-rotation interaction constants. This resulted in an anomalously large number of correction parameters being attributed to the breakdown of the Born-Oppenheimer approximation.

The hydrides of Group 12 elements were studied in our laboratory, and the primary goal was to detect ZnH_2, CdH_2 and HgH_2 in the gas phase. These molecules were generated in the gas phase and their infrared emission spectra were recorded (see Chapter 5). The spectra also contained a few vibration-rotation bands of ZnH, ZnD, CdH and CdD in the $X\ ^2\Sigma^+$ ground state, which are described in this chapter. The results presented in this chapter have been previously published in Ref. [36].

3.2 Experimental Details

Zinc and cadmium hydride molecules were generated in the discharge-furnace emission source described in Chapter 1, and infrared emission spectra were recorded using a Bruker IFS 120 HR Fourier transform spectrometer. A small tantalum boat containing about 100 grams of zinc or cadmium was placed inside the central part of an alumina tube, and heated to 470°C or 350°C, respectively, in order to produce about 0.5 Torr of metal vapour. Pure hydrogen or deuterium (total pressure ~ 0.5–2.5 Torr) flowed slowly through the cell, and a BaF_2 or KBr lens was used to focus the emission onto the entrance aperture of the spectrometer. Infrared emission spectra were recorded using a KBr beamsplitter and a liquid-nitrogen-cooled MCT detector. Infrared longwave-pass filters were used to limit the spectral range to the 1200–2200 cm^{-1} region for ZnH/CdH, and to the 800–1600 cm^{-1} region for ZnD/CdD. The instrumental resolution was set to 0.01 cm^{-1}, and a few hundred spectra were co-added in order to improve the signal-to-noise ratio. The signal-to-noise ratios for the strongest emission lines of ZnH, ZnD, CdH and CdD were about 60, 50, 15 and 10, respectively. The blackbody emission profile was subtracted from the original spectra using the Bruker OPUS software, in order to obtain flat baselines. Overviews of the infrared emission spectra of ZnH, CdH and CdD are shown in Figures 3.1 to 3.3, respectively, and the *R*-branch of the fundamental band of ZnD is shown in Figure 3.4.

In addition to the infrared emission spectra, new far-infrared absorption spectra of CdH and CdD were recorded using the NIST tuneable-far-infrared spectrometer in Boulder, Colorado. The experimental conditions were exactly the same as those described in Ref. [35], and several rotational transitions in the v = 1 level of CdH and CdD were measured.

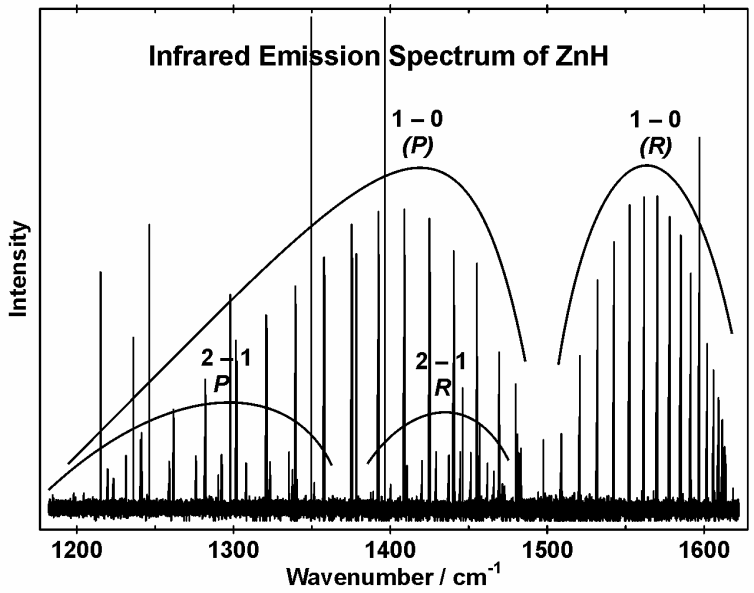

Fig. 3.1. An overview of the infrared emission spectrum of ZnH after baseline correction.

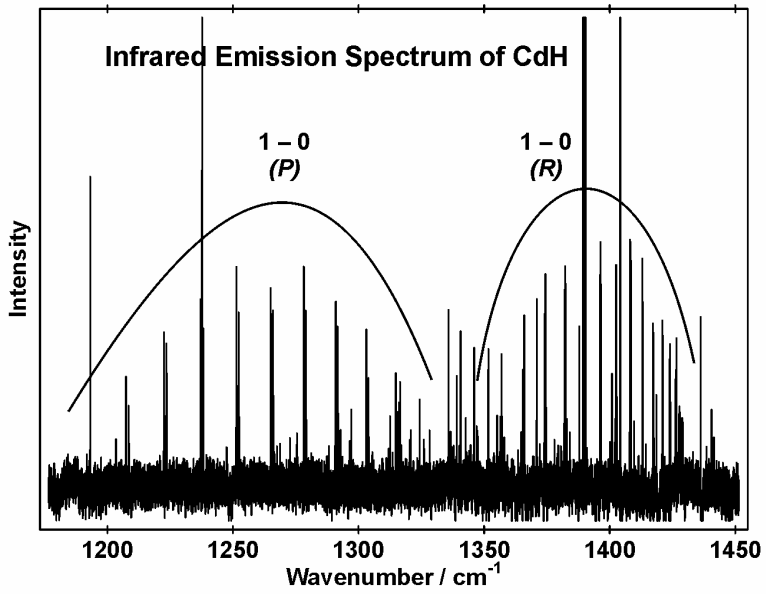

Fig. 3.2. An overview of the infrared emission spectrum of CdH after baseline correction.

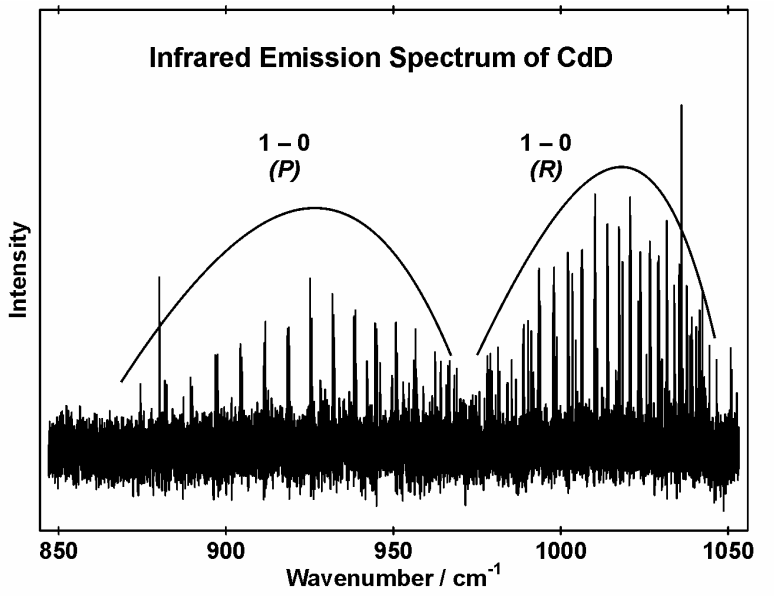

Fig. 3.3. An overview of the infrared emission spectrum of CdD after baseline correction.

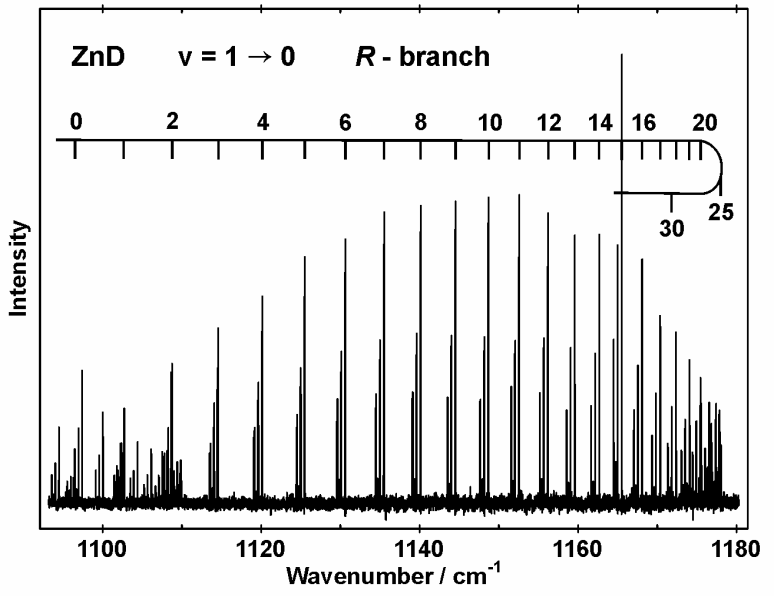

Fig. 3.4. A portion of the infrared emission spectrum of ZnD showing the *R*-branch head of the fundamental band.

3.3 Results and Analyses

The infrared emission spectra contained atomic and molecular emission lines, as well as blackbody emission from the hot tube and absorption lines from atmospheric water vapour. In order to obtain flat baselines, the blackbody emission profile was subtracted from the spectra using the Bruker OPUS software. The v = 1→0 and v = 2→1 bands of ZnH, ZnD, CdH and CdD, as well as the v = 3→2 band of ZnD in the $X\,^2\Sigma^+$ ground state were observed in emission.

Zinc has five stable isotopes with the following terrestrial abundances: ^{64}Zn (48.6%), ^{66}Zn (27.9%), ^{67}Zn (4.1%), ^{68}Zn (18.8%), and ^{70}Zn (0.6%). The terrestrial abundances for the eight isotopes of cadmium are: ^{106}Cd (1.3%), ^{108}Cd (0.9%), ^{110}Cd (12.5%), ^{111}Cd (12.8%), ^{112}Cd (24.1%), ^{113}Cd (12.2%), ^{114}Cd (28.7%), and ^{116}Cd (7.5%). Lines from most of these isotopes (all except ^{70}Zn, ^{106}Cd and ^{108}Cd) were observed in the spectra, and the isotope splittings were completely resolved. A doublet splitting was observed in almost all vibration-rotation lines due to the spin-rotation interaction that lifts the degeneracy of the *e* (F_1) and *f* (F_2) spin components. The isotope splitting and spin splitting in one rotational line of CdH and of ZnD are shown in Figures 3.5 and 3.6, respectively.

Line positions were measured using the WSPECTRA program. In addition to ZnH, ZnD, CdH and CdD, molecular emission lines from ZnH_2, ZnD_2, CdH_2 and CdD_2 were observed, and the analyses of their spectra have been published [37-41]. The ZnH and CdH spectra also contained strong CO (impurity) emission lines, which were used for absolute wavenumber calibration [42]. The ZnD and CdD spectra were then calibrated using several atomic emission lines that were common to both hydride and deuteride spectra. The absolute accuracy of calibrated line positions in ZnH and ZnD spectra is about 0.0005 cm^{-1}. The calibrated CdH and CdD line positions have an accuracy of about 0.001 cm^{-1}.

The published diode laser infrared spectra of ZnH, ZnD, CdH and CdD contained the v = 1←0 and v = 2←1 bands for these species [31,32]. The number of rotational lines in each band was limited, due to spectral gaps in the diodes available. For example, only one rotational line was observed in the *P*-branch of the v = 2←1 bands of ZnD and CdD [31,32]. All the diode laser infrared lines were included in the new data sets, and there was no systematic discrepancy between those lines and the calibrated line positions in the infrared emission spectra. All pure rotation data available in the literature [33-35] were also included

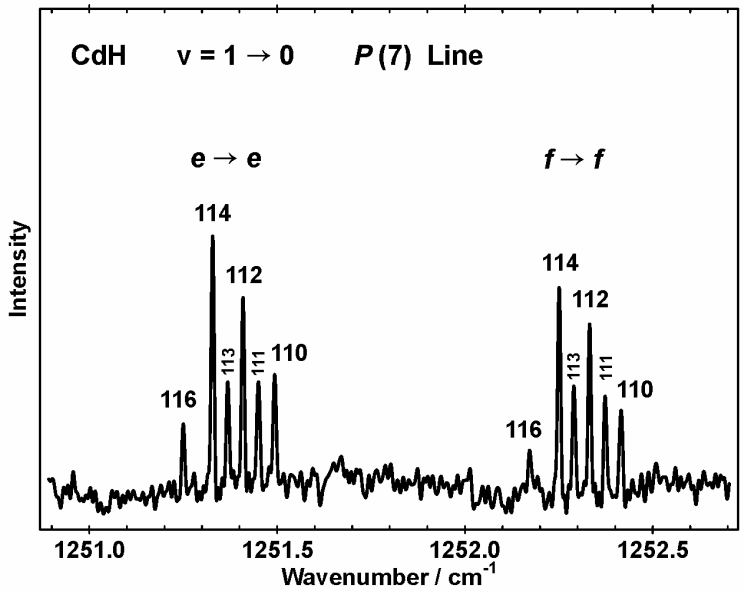

Fig. 3.5. An expanded view of one rotational line in the CdH infrared spectrum showing the spin doubling (*e*/*f*) and the isotope splitting. Lines have been marked by the mass numbers of cadmium isotopes.

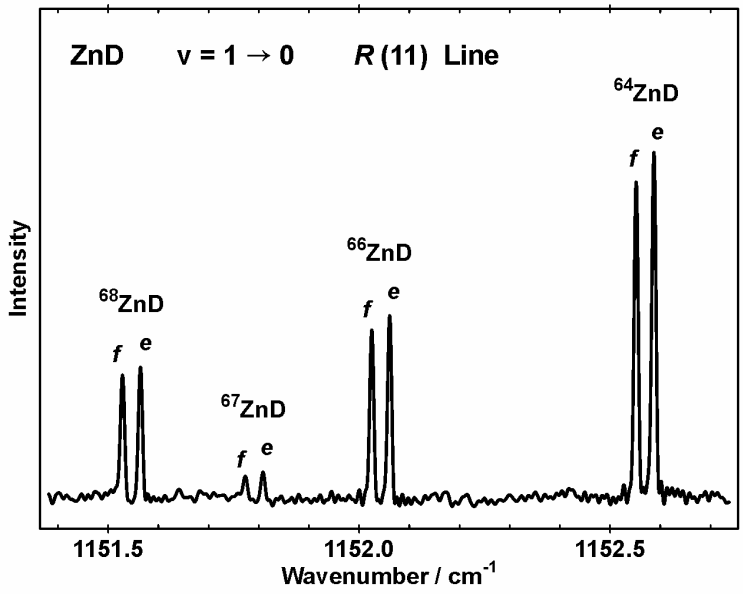

Fig. 3.6. An expanded view of one rotational line in the ZnD infrared spectrum showing the isotope splitting and the spin doubling (*e*/*f*).

in the new data sets as hypothetical "hyperfine-free" line positions calculated in the same manner as explained in Chapter 2.

Program DParFit [43] was used to fit all the data to the following energy level expressions in which $x = N(N+1)$:

$$E^{e}_{v,N} = G_v + B_v\, x - D_v\, x^2 + H_v\, x^3 + L_v\, x^4 + \tfrac{1}{2} N \cdot \left(\gamma_v + \gamma_{D,v} x + \gamma_{H,v} x^2\right), \qquad (3.1)$$

$$E^{f}_{v,N} = G_v + B_v\, x - D_v\, x^2 + H_v\, x^3 + L_v\, x^4 - \tfrac{1}{2}(N+1) \cdot \left(\gamma_v + \gamma_{D,v} x + \gamma_{H,v} x^2\right), \qquad (3.2)$$

and individual band constants were determined for each observed vibrational level. In order to minimize the number of digits required to reproduce the data accurately, the band constants were sequentially rounded and refitted [44], starting from the highest order parameter of the highest observed vibrational level. The rounded constants for ^{64}ZnH, ^{64}ZnD, ^{114}CdH and ^{114}CdD are listed in Tables 3.1 and 3.2.

The data for all isotopologues were then combined and fitted simultaneously using Dunham-type energy level expressions for $^2\Sigma^+$ states. The energy expressions [45] and the reduced-mass-scaling relationships [46,47] were identical to those in Eqs. (2.3) to (2.6). Program DParFit was used for multi-isotopologue fitting, with the reference isotopologues chosen to be ^{64}ZnH and ^{114}CdH. The Dunham constants of the reference isotopologues and the Born-Oppenheimer breakdown correction parameters are listed in Tables 3.3 and 3.4. The constants of Tables 3.3 and 3.4 have also been sequentially rounded and refitted [44], starting from the parameter with largest relative uncertainty. The Dunham constants of ^{64}ZnD and ^{114}CdD are derived from those of ^{64}ZnH and ^{114}CdH using equations (2.5) and (2.6), and require more digits, as determined by parameter sensitivities [44]. Complete lists of all the data used in the analyses, and the Dunham constants for all isotopologues have been published as supplementary tables in Ref. [36].

The equilibrium rotational constants ($B_e \approx Y_{0,1}$) of ^{64}ZnH and ^{114}CdH in Tables 3.3 and 3.4 have high precision, mainly because the pure rotational data were included in the data sets. Using the B_e constants of ^{64}ZnH and ^{114}CdH, the associated equilibrium internuclear distances (r_e) of these species were determined to be 1.593478(2) Å and 1.760098(3) Å, respectively. Similarly, r_e distances of 1.593001(2) Å and 1.759695(2) Å were obtained for ^{64}ZnD and ^{114}CdD, respectively, using the derived B_e constants in Tables 3.3 and 3.4. The r_e distances of ^{64}ZnD and ^{114}CdD are slightly different from those of ^{64}ZnH and ^{114}CdH due to the breakdown of the Born-Oppenheimer approximation. The $\delta^{H}_{0,1}$ correction parameters are responsible for these discrepancies in the r_e values.

Table 3.1. Band constants (in cm^{-1}) for the $X\,^2\Sigma^+$ ground state of ^{64}ZnH and ^{64}ZnD.[a]

	^{64}ZnH		
	v = 0	v = 1	v = 2
G_v	0.0	1496.47788(22)	2873.7218(5)
B_v	6.5476308(9)	6.2420626(78)	5.900569(25)
$10^4\,D_v$	4.72631(14)	4.96334(72)	5.3998(34)
$10^8\,H_v$	0.708(8)	–0.173(24)	–2.25(16)
$10^{12}\,L_v$	–3.99(14)	–9.8(3)	–21(3)
γ_v	0.253108(4)	0.23366(4)	0.21193(8)
$10^4\,\gamma_{D,v}$	–0.7930(7)	–0.806(2)	–0.868(4)
$10^8\,\gamma_{H,v}$	0.51(4)	…	…

	^{64}ZnD			
	v = 0	v = 1	v = 2	v = 3
G_v	0.0	1089.91437(14)	2122.38807(21)	3092.1493(8)
B_v	3.35036133(49)	3.2425018(28)	3.127117(5)	3.001227(16)
$10^4\,D_v$	1.21635(3)	1.25213(14)	1.30817(30)	1.3905(7)
$10^8\,H_v$	0.10632(84)	0.0364(24)	–0.078(7)	–0.426(9)
$10^{12}\,L_v$	–0.225(7)	–0.42(1)	–0.78(5)	…
γ_v	0.129973(3)	0.123093(18)	0.11579(3)	0.10781(8)
$10^4\,\gamma_{D,v}$	–0.20372(18)	–0.2032(4)	–0.2119(6)	–0.225(2)
$10^8\,\gamma_{H,v}$	0.066(3)	…	…	…

[a] The numbers in parentheses are 2σ uncertainties in the last quoted digits.

Table 3.2. Band constants (in cm^{-1}) for the $X\,^2\Sigma^+$ ground state of ^{114}CdH and ^{114}CdD.[a]

	^{114}CdH		
	v = 0	v = 1	v = 2
G_v	0.0	1336.9576(2)	2549.9724(16)
B_v	5.3254120(3)	5.0631697(11)	4.76031(7)
$10^4\,D_v$	3.171414(39)	3.4278(2)	3.961(6)
$10^8\,H_v$	–0.1265(24)	–1.036(13)	…
$10^{12}\,L_v$	–2.65(5)	–6.8(3)	…
γ_v	0.604595(3)	0.55218(1)	0.4916(4)
$10^4\,\gamma_{D,v}$	–1.71829(29)	–1.8101(5)	–1.99(5)
$10^8\,\gamma_{H,v}$	0.641(9)	…	…

	^{114}CdD		
	v = 0	v = 1	v = 2
G_v	0.0	973.5970(2)	1888.6176(16)
B_v	2.70739863(20)	2.6165496(30)	2.517426(31)
$10^4\,D_v$	0.80227(2)	0.84119(27)	0.908(1)
$10^8\,H_v$	–0.0056(8)	–0.0590(96)	…
$10^{12}\,L_v$	–0.13(1)	–0.4(1)	…
γ_v	0.308833(3)	0.290693(24)	0.2707(3)
$10^4\,\gamma_{D,v}$	–0.43525(19)	–0.4474(6)	–0.46(2)
$10^8\,\gamma_{H,v}$	0.091(3)	…	…

[a] The numbers in parentheses are 2σ uncertainties in the last quoted digits.

Table 3.3. Dunham and Born-Oppenheimer breakdown constants (in cm^{-1}) for the $X\ ^2\Sigma^+$ ground state of ^{64}ZnH and ^{64}ZnD (all uncertainties are 2σ).

Dunham	^{64}ZnH	^{64}ZnD	Born-Oppenheimer breakdown	
$Y_{1,0}$	1603.1813(70)	1143.218719	$\delta^{H}_{1.0}$	1.1504(6)
$Y_{2,0}$	–50.50089(940)	–25.6614425		
$Y_{3,0}$	–1.5064(50)	–0.545649		
$Y_{4,0}$	–0.1612(9)	–0.04162259		
$Y_{0,1}$	6.69133166(1700)	3.402155578	$\delta^{H}_{0,1}$	0.0080074(62)
$Y_{1,1}$	–0.2825981(670)	–0.102371518	$\delta^{H}_{1,1}$	–0.000048(6)
$Y_{2,1}$	–0.0089738(860)	–0.002317077		
$Y_{3,1}$	–0.00113(5)	–0.0002079857		
$Y_{4,1}$	–0.0002689(81)	–0.0000352807		
$10^4\ Y_{0,2}$	–4.648825(690)	–1.2028793	$10^4\ \delta^{H}_{0,2}$	–0.01962(21)
$10^4\ Y_{1,2}$	–0.14087(220)	–0.02539308	$10^4\ \delta^{H}_{1,2}$	0.00582(15)
$10^4\ Y_{2,2}$	–0.0191(17)	–0.00250599		
$10^4\ Y_{3,2}$	–0.01801(37)	–0.001684422		
$10^8\ Y_{0,3}$	1.0804(220)	0.1440468	$10^8\ \delta^{H}_{0,3}$	0.035(5)
$10^8\ Y_{1,3}$	–0.866(66)	–0.0809944		
$10^8\ Y_{2,3}$	0.33(5)	0.022001		
$10^8\ Y_{3,3}$	–0.202(8)	–0.0096		
$10^{12}\ Y_{0,4}$	–3.19(20)	–0.212676	$\delta^{Zn}_{0,1}$	0.000141(2)
$10^{12}\ Y_{1,4}$	0.0(6)	0.0		
$10^{12}\ Y_{2,4}$	–3.0(3)	–0.101632		
$\gamma_{0,1}$	0.26258(4)	0.13342699		
$\gamma_{1,1}$	–0.019538(160)	–0.00707706		
$\gamma_{2,1}$	0.00182(25)	0.00046993		
$\gamma_{3,1}$	–0.001362(150)	–0.00025069		
$\gamma_{4,1}$	0.00021(3)	0.000027553		
$10^4\ \gamma_{0,2}$	–0.78782(110)	–0.2034188		
$10^4\ \gamma_{1,2}$	–0.005(2)	–0.00092		
$10^4\ \gamma_{2,2}$	–0.0120(9)	–0.0015744		
$10^8\ \gamma_{0,3}$	0.639(23)	0.08384		
$10^8\ \gamma_{1,3}$	–0.21(4)	–0.01964		

Table 3.4. Dunham and Born-Oppenheimer breakdown constants (in cm^{-1}) for the $X\ ^2\Sigma^+$ ground state of ^{114}CdH and ^{114}CdD (all uncertainties are 2σ).

Dunham	^{114}CdH	^{114}CdD	Born-Oppenheimer breakdown	
$Y_{1,0}$	1443.47421(310)	1025.923761	$\delta^{H}_{1.0}$	1.0707(11)
$Y_{2,0}$	–48.3345(25)	–24.397623		
$Y_{3,0}$	–3.0301(6)	–1.0866568		
$Y_{0,1}$	5.4470743(180)	2.750760873	$\delta^{H}_{0,1}$	0.00500315(1300)
$Y_{1,1}$	–0. 23936712(5700)	–0.085773934	$\delta^{H}_{1,1}$	0.00038(2)
$Y_{2,1}$	–0.006349(50)	–0.001617655		
$Y_{3,1}$	–0.0031315(140)	–0.000566863		
$10^4\ Y_{0,2}$	–3.085445(650)	–0.78711618	$10^4\ \delta^{H}_{0,2}$	–0.00769(19)
$10^4\ Y_{1,2}$	–0.1604(24)	–0.02903555		
$10^4\ Y_{2,2}$	–0.012(3)	–0.00154331		
$10^4\ Y_{3,2}$	–0.02216(94)	–0.002024817		
$10^8\ Y_{0,3}$	0.013(8)	0.0045634	$10^8\ \delta^{H}_{0,3}$	0.045(3)
$10^8\ Y_{1,3}$	–0.07(2)	–0.0063961		
$10^8\ Y_{2,3}$	–0.4186(100)	–0.0271744		
$10^{12}\ Y_{0,4}$	–0.56(8)	–0.036354	$\delta^{Cd}_{0,1}$	0.0000495(9)
$10^{12}\ Y_{1,4}$	–4.17(14)	–0.192328		
$\gamma_{0,1}$	0.6304422(330)	0.31822593		
$\gamma_{1,1}$	–0.055197(170)	–0.01979479		
$\gamma_{2,1}$	0.01053(31)	0.00268293		
$\gamma_{3,1}$	–0.007754(200)	–0.00140363		
$\gamma_{4,1}$	0.00139(4)	0.000178766		
$10^4\ \gamma_{0,2}$	–1.6891(8)	–0.430364		
$10^4\ \gamma_{1,2}$	–0.046(2)	–0.0083269		
$10^4\ \gamma_{2,2}$	–0.0244(7)	–0.0031381		
$10^8\ \gamma_{0,3}$	0.899(21)	0.115619		
$10^8\ \gamma_{1,3}$	–0.52(4)	–0.047514		

3.4 Discussion

The new Dunham constants for ZnH and CdH are compared with those determined from the diode laser infrared spectra [31,32] in Table 3.5. The constants reported in Ref. [32] were in the form of mass-independent $U_{l,m}$ and $\Delta_{l,m}$ coefficients [48,49], and were transformed to regular $Y_{l,m}$ constants [46] for comparison. Only the B_e constants and the $Y_{l,0}$ coefficients that represent the vibrational energy are compared. There is no point in comparing higher-order $Y_{l,m}$ constants with $m>0$, because the new data sets were much more extensive than the diode laser infrared data alone. It is interesting to note that although the $Y_{1,0}$ and $Y_{2,0}$ coefficients have very small relative uncertainties, their values depend strongly on the model, i.e., on the order of polynomial used for vibrational energy, see Table 3.5. In the ZnH/ZnD multi-isotopologue fits, the new $Y_{l,0}$ constants are clearly preferred to those reported in diode laser infrared studies [31,32] because there was an extra vibration-rotation band in the new data set, i.e., the v = 3→2 band of ZnD, which led to determination of higher order Dunham coefficients. In the CdH/CdD fits, the vibrational range of the data set used in the new fit was the same as that used in the diode laser infrared studies, i.e., v = 0 to 2 for both CdH and CdD, but a different model was used here. Instead of fitting the vibrational energies of CdH and CdD to two Dunham constants ($Y_{1,0}$ and $Y_{2,0}$) and introducing two Born-Oppenheimer breakdown correction parameters ($\delta^{H}_{1,0}$ and $\delta^{H}_{2,0}$), a third-order polynomial was used for $Y_{l,0}$ with only one correction parameter $\delta^{H}_{1,0}$. The new $Y_{1,0}$ and $Y_{2,0}$ coefficients are therefore considerably different from those of Urban et al. [31] and Birk et al. [32]. Fortunately, it is possible to ascertain which model is more reliable in this case, because the v = 3→2 vibrational interval of ^{114}CdD is known with relatively high accuracy (± 0.05 cm^{-1}) from Balfour's work [21]. He studied the $A\ ^2\Pi \rightarrow X\ ^2\Sigma^+$ electronic spectrum of CdD and observed a vibrational energy difference of 849.93 cm^{-1} between the v = 3 and 2 levels of ^{114}CdD [21]. Somewhat surprisingly, the derived Dunham constants for ^{114}CdD in Table 3.4 predict the v = 3→2 vibrational interval to be 849.927 cm^{-1}, equal to Balfour's measured value within its experimental uncertainty. On the other hand, using the CdD Dunham constants reported by Birk et al. [32] one predicts 856.413 cm^{-1} for the v = 3→2 vibrational interval, which differs from the observed value by more than 6 cm^{-1}. This indicates that a second-order polynomial is inadequate for representing the vibrational energy levels of CdH or CdD, and proves that a

third-order polynomial for $Y_{l,0}$ coefficients with only one correction parameter ($\delta^{H}_{1,0}$) is a more realistic model for those vibrational energies.

As for other diatomic hydrides in Chapter 2, several Born-Oppenheimer breakdown correction parameters for the hydrogen atom ($\delta^{H}_{l,m}$) were required in the multi-isotopologue fits for ZnH and CdH. Due to the presence of high quality rotational data (less than 10^{-5} cm^{-1} uncertainties), small correction parameters due to zinc and cadmium isotopes could be determined for the B_e constants (see the $\delta^{Zn}_{0,1}$ and $\delta^{Cd}_{0,1}$ values in Tables 3.3 and 3.4). The presence of these small correction parameters implies that the equilibrium internuclear distances (r_e) are not exactly the same, even within different isotopes of zinc and cadmium.

In a previous study, Varberg and Roberts [35] reported that four Born-Oppenheimer breakdown parameters for $\gamma_{l,m}$ constants were required in order to fit all the pure rotation data in the v = 0 of CdH and CdD together. It is now clear that these correction parameters only appeared to be required because the vibrational dependence of the γ, γ_D and γ_H constants had been overlooked in their analysis. The v = 0 ground state of CdD lies about 200 cm^{-1} lower than that of CdH, and the reduced mass scaling ratio in Eq. (2.6), derived by Brown and Watson [47], applies only to the equilibrium $\gamma_{l,m}$ constants associated with the bottom of the potential well, and not to the effective γ values at v = 0. The present work shows that when the vibrational dependence of the spin-rotation interaction constants is taken into account properly, no Born-Oppenheimer breakdown correction parameter is required for the $\gamma_{l,m}$ constants, and Eq. (2.6) accounts fully for the isotopologue dependence of these parameters. The effective γ_v constant for each individual vibrational level is calculated from the following equation, in which the $\gamma_{l,m}$ coefficients of different isotopologues are related by Eq. (2.6).

$$\gamma_v = \gamma_{0,1} + \gamma_{1,1}\left(v + \tfrac{1}{2}\right) + \gamma_{2,1}\left(v + \tfrac{1}{2}\right)^2 + \gamma_{3,1}\left(v + \tfrac{1}{2}\right)^3 + \gamma_{4,1}\left(v + \tfrac{1}{2}\right)^4 . \qquad (3.3)$$

If one plots $\gamma_v^{\alpha}\left(\mu_\alpha/\mu_1\right)$ versus $\left(v + \tfrac{1}{2}\right)\sqrt{\left(\mu_1/\mu_\alpha\right)}$ for different isotopologues, all the points should fall on a single curve, providing Eq. (2.6) holds exactly. This is in fact the case for ZnH/ZnD and CdH/CdD isotopologues, as is illustrated in Figures 3.7 and 3.8. The individual γ_v constants are taken from Tables 3.1 and 3.2 (independent fits) and the solid curves are calculated from the $\gamma_{l,m}$ constants of Tables 3.3 and 3.4 (multi-isotopologue fits). The plots of Figures 3.7 and 3.8 provide further confirmation for Eq. (2.6), which was derived by Brown and Watson [47]. Thus, the Born-Oppenheimer breakdown correction parameters for the spin-rotation interaction constants reported by Varberg and Roberts [35] were artefacts of their neglect of the vibrational dependence of γ.

Table 3.5. A comparison of the new Dunham constants of ZnH, ZnD, CdH and CdD with those obtained in previous studies (all uncertainties are 2σ).

Constant	^{64}ZnH	^{64}ZnH, Ref. [32][a]	^{64}ZnD	^{64}ZnD, Ref. [32][a]
$Y_{1,0}$ (cm^{-1})	1603.181(7)	1615.748(23)	1143.219(5)	1147.398(12)
$Y_{2,0}$ (cm^{-1})	–50.501(9)	–59.636(12)	–25.661(5)	–28.736(5)
$Y_{3,0}$ (cm^{-1})	–1.506(5)	…	–0.546(2)	…
$Y_{4,0}$ (cm^{-1})	–0.1612(9)	…	–0.0416(2)	…
B_e (cm^{-1})	6.69133(2)	6.68686(33)	3.402156(7)	3.401588(136)
r_e (Å)	1.593478(2)	…	1.593001(2)	…

Constant	^{114}CdH	^{114}CdH, Ref. [32][a]	^{114}CdD	^{114}CdD, Ref. [32][a]
$Y_{1,0}$ (cm^{-1})	1443.474(3)	1460.945(8)	1025.924(2)	1032.200(4)
$Y_{2,0}$ (cm^{-1})	–48.334(3)	–61.994(5)	–24.398(1)	–29.298(2)
$Y_{3,0}$ (cm^{-1})	–3.0301(6)	…	–1.0867(2)	…
B_e (cm^{-1})	5.44707(2)	5.44073(18)	2.750761(6)	2.749767(69)
r_e (Å)	1.760098(3)	…	1.759695(2)	…

[a] The $U_{l,m}$ and $\Delta_{l,m}$ constants reported in Ref. [32] were used to calculate these Dunham coefficients, and the uncertainties were obtained by propagation of errors.

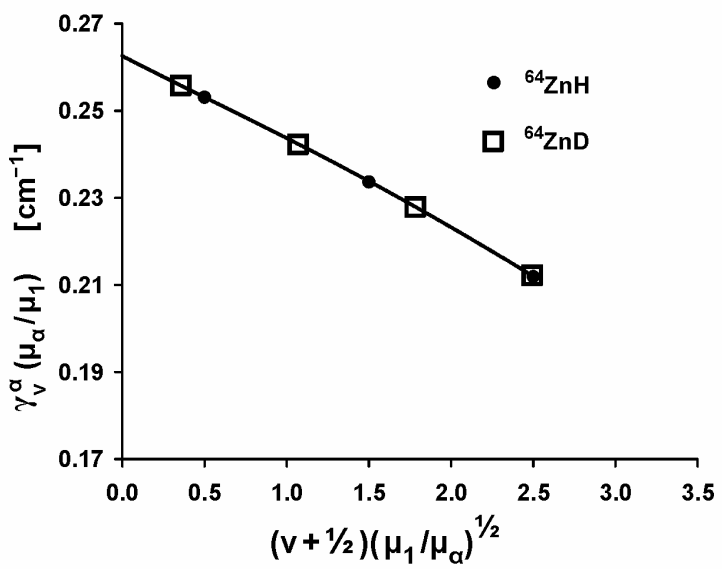

Fig. 3.7. The γ_v constants of ^{64}ZnH and ^{64}ZnD (from Table 3.1) are scaled by reduced masses and plotted versus the reduced-mass-scaled vibrational quantum numbers. The reference isotopologue ($\alpha = 1$) is ^{64}ZnH, and the solid curve is calculated from Eq. (3.3) using the constants of Table 3.3.

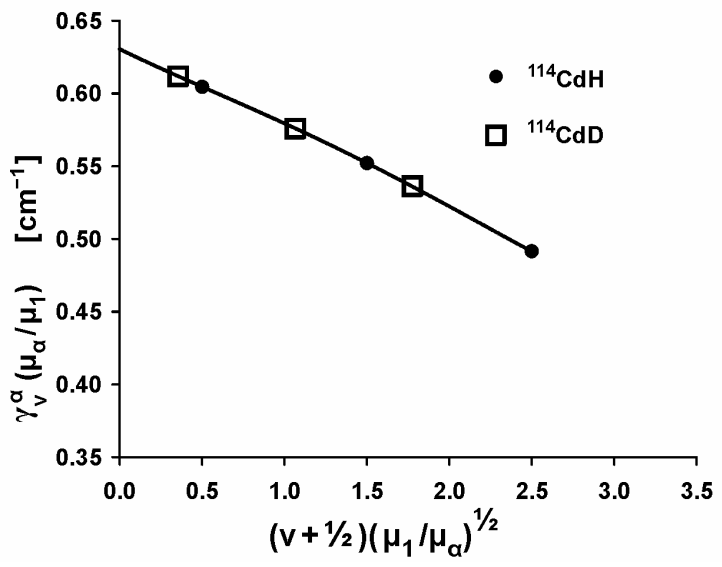

Fig. 3.8. The γ_v constants of ^{114}CdH and ^{114}CdD (from Table 3.2) are scaled by reduced masses and plotted versus the reduced-mass-scaled vibrational quantum numbers. The reference isotopologue ($\alpha = 1$) is ^{114}CdH, and the solid curve is calculated from Eq. (3.3) using the constants of Table 3.4.

3.5 Summary

High resolution infrared emission spectra of ZnH, ZnD, CdH and CdD were recorded with a Fourier transform spectrometer, and a few vibration-rotation bands in the $X\,^2\Sigma^+$ ground state were observed for these species. In addition, new measurements of pure rotational transitions in the v = 1 level of the $X\,^2\Sigma^+$ ground state were obtained for CdH and CdD. The new data were combined with the previous data from diode laser infrared spectra and pure rotational spectra of ZnH/ZnD and CdH/CdD available in the literature. Band constants were determined for each observed vibrational level by least-squares fitting of all the data. In addition, empirical Dunham constants and Born-Oppenheimer breakdown correction parameters were obtained simultaneously from multi-isotopologue fits to the data. Using the equilibrium rotational constants (B_e), the associated equilibrium internuclear distances (r_e) of ^{64}ZnH, ^{64}ZnD, ^{114}CdH and ^{114}CdD were determined to be 1.593478(2) Å, 1.593001(2) Å, 1.760098(3) Å and 1.759695(2) Å, respectively. The reduced-mass scaling ratio for the spin-rotation interaction constants derived by Brown and Watson [47] was further confirmed, as all isotopic data could be fitted together without any mass-scaled correction parameters for the $\gamma_{l,m}$ constants. Many of the Born-Oppenheimer breakdown parameters reported previously for CdH and CdD vanished when the vibrational dependences of the rotational and spin-rotation interaction constants were taken into account properly.

3.6 References

[1] E. Hulthén, Z. Physik. 11 (1922) 284-293.

[2] A. Kratzer, Ann. Physik. 71 (1923) 72-103.

[3] R.S. Mulliken, Nature 113 (1924) 489-490.

[4] E. Hulthén, Nature 116 (1925) 642.

[5] R.S. Mulliken, Proc. Natl. Acad. Sci. USA. 12 (1926) 151-158.

[6] E. Hulthén, Z. Physik. 45 (1927) 331-336.

[7] R.S. Mulliken, Phys. Rev. 32 (1928) 388-416.

[8] E. Svensson, Z. Physik. 59 (1930) 333-352.

[9] E. Svensson, Nature 131 (1933) 28.

[10] G. Stenvinkel, E. Svensson, Nature 135 (1935) 955.

[11] G. Stenvinkel, Doctoral Dissertation, University of Stockholm (1936).

[12] E. Svensson, Doctoral Dissertation, University of Stockholm (1935).

[13] Y. Fujioka, Y. Tanaka, Sci. Pap. Inst. Phys. Chem. Res. 32 (1937) 143-156.

[14] O. Deile, Z. Physik. 106 (1937) 405-417.

[15] G. Stenvinkel, E. Svensson, E. Olsson, Ark. Mat. Astr. Fys. 26A (1938) 1-15.

[16] S. Mrozowski, Phys. Rev. 58 (1940) 597-599.

[17] M.A. Khan, Proc. Phys. Soc. 80 (1962) 599-607.

[18] M.A. Khan, Proc. Phys. Soc. 80 (1962) 1264-1268.

[19] K.P. Huber, G. Herzberg, Molecular Spectra and Molecular Structure IV. Constants of Diatomic Molecules, Van Nostrand, New York (1979).

[20] W.J. Balfour, A.W. Taylor, J. Mol. Spectrosc. 91 (1982) 9-21.

[21] W.J. Balfour, Phys. Scr. 25 (1982) 257-267.

[22] W.J. Balfour, K.S. Chandrasekhar, B. Lindgren, J. Mol. Spectrosc. 119 (1986) 126-136.

[23] W.J. Balfour, R.S. Ram, J. Mol. Spectrosc. 121 (1987) 199-208.

[24] L.C. O'Brien, W.T.M.L. Fernando, P.F. Bernath, J. Mol. Spectrosc. 139 (1990) 424-431.

[25] D.P. Chong, S.R. Langhoff, J. Chem. Phys. 84 (1986) 5606-5610.

[26] D.P. Chong, S.R. Langhoff, C.W. Bauschilcher, Jr., S.P. Walch, H. Partridge, J. Chem. Phys. 85 (1986) 2850-2860.

[27] K. Balasubramanian, J. Chem. Phys. 93 (1990) 8061-8072.

[28] Ch. Jamorski, A. Dargelos, Ch. Teichteil, J.P. Daudey, J. Chem. Phys. 100 (1994) 917-925.

[29] E. Eliav, U. Kaldor, B.A. Hess, J. Chem. Phys. 108 (1998) 3409-3415.

[30] R.S. Wojslaw, B.F. Peery, Jr., Astrophys. J. Suppl. Ser. 31 (1976) 75-92.

[31] R.-D. Urban, U. Magg, H. Birk, H. Jones, J. Chem. Phys. 92 (1990) 14-21.

[32] H. Birk, R.-D. Urban, P. Polomsky, H. Jones, J. Chem. Phys. 94 (1991) 5435-5442.

[33] M. Goto, K. Namiki, S. Saito, J. Mol. Spectrosc. 173 (1995) 585-590.

[34] F.A. Tezcan, T.D. Varberg, F. Stroh, K.M. Evenson, J. Mol. Spectrosc. 185 (1997) 290-295.

[35] T.D. Varberg, J.C. Roberts, J. Mol. Spectrosc. 223 (2004) 1-8.

[36] A. Shayesteh, R.J. Le Roy, T.D. Varberg, P.F. Bernath, J. Mol. Spectrosc. 237 (2006) 87-96.

[37] A. Shayesteh, D.R.T. Appadoo, I.E. Gordon, P.F. Bernath, J. Am. Chem. Soc. 126 (2004) 14356-14357.

[38] A. Shayesteh, S. Yu, P.F. Bernath, Chem.-Eur. J. 11 (2005) 4709-4712.

[39] S. Yu, A. Shayesteh, P.F. Bernath, J. Chem. Phys. 122 (2005) 194301:1-6.

[40] A. Shayesteh, I.E. Gordon, D.R.T. Appadoo, P.F. Bernath, Phys. Chem. Chem. Phys. 7 (2005) 3132-3142.

[41] A. Shayesteh, S. Yu, P.F. Bernath, J. Phys. Chem. A 109 (2005) 10280-10286.

[42] A.G. Maki, J.S. Wells, Wavenumber Calibration Tables from Heterodyne Frequency Measurements, NIST Special Publication 821, U.S. Government Printing Office, Washington (1991).

[43] R.J. Le Roy, DParFit 3.0, A Computer Program for Fitting Multi-Isotopomer Diatomic Molecule Spectra, University of Waterloo Chemical Physics Research Report CP-658 (2004); http://leroy.uwaterloo.ca.

[44] R.J. Le Roy, J. Mol. Spectrosc. 191 (1988) 223-231.

[45] J.L. Dunham, Phys. Rev. 41 (1932) 721-731.

[46] R.J. Le Roy, J. Mol. Spectrosc. 194 (1999) 189-196.

[47] J.M. Brown, J.K.G. Watson, J. Mol. Spectrosc. 65 (1977) 65-74.

[48] P.R. Bunker, J. Mol. Spectrosc. 68 (1977) 367-371.

[49] J.K.G. Watson, J. Mol. Spectrosc. 80 (1980) 411-421.

Chapter 4

Infrared Emission Spectra of BeH_2 and MgH_2

4.1 Introduction

BeH_2 is a famous molecule. The chemical bonding in BeH_2 is discussed in introductory chemistry textbooks, in the context of the formation of *sp* hybrid orbitals [1]. With only six electrons, BeH_2 is the smallest neutral polyatomic molecule, and it is a favourite target molecule for quantum chemists to test new ab initio theoretical methods [2-6]. Theoretical calculations on BeH_2 have predicted a linear H–Be–H geometry with a closed-shell $\widetilde{X}\ ^1\Sigma_g^+$ ground electronic state for this molecule [7-9]. However, the high toxicity of beryllium-containing compounds [10] has inhibited experimental work. The gas phase reaction of beryllium atoms with molecular hydrogen has been studied by ab initio theoretical calculations [11-14]. The insertion of ground state Be atoms into the H_2 bond has a barrier of 48.6 kcal/mol [13], but the overall reaction, $Be(g) + H_2(g) \rightarrow BeH_2(g)$, is predicted to be favourable and to be exoergic [9] by 37.6 kcal/mol. In spite of the strong interest in BeH_2, the molecule remained unknown except for the detection of its infrared spectrum in a solid argon matrix [15] at 10 K. In the series of first-row hydrides, LiH, BeH_2, BH_3, CH_4, NH_3, OH_2 and FH, gaseous BeH_2 was the only free molecule remaining to be discovered.

The reaction of magnesium vapour with molecular hydrogen has been studied extensively both by theoretical calculations [16-20] and by laser pump-probe techniques [21-31]. Magnesium atoms in the $3s3p$ excited electronic states (^3P and ^1P) react with H_2 to produce MgH and H radicals, and a bent MgH_2 complex is assumed to be the reaction intermediate [30]. The gas phase reaction of ground state Mg with H_2 is inhibited by a large

barrier to insertion [17], and the overall reaction, $Mg(g) + H_2(g) \rightarrow MgH_2(g)$ is predicted to be endoergic by a few kcal/mol [7,32,33]. Ab initio theoretical calculations also predicted a linear H–Mg–H geometry with a closed-shell $\widetilde{X}\ ^1\Sigma_g^+$ ground electronic state [7,34] for MgH_2. Infrared absorption spectra of MgH_2 trapped in solid argon [35], krypton and xenon matrices [36] at 10-12 K were recorded, but the gas phase molecule remained unknown.

Solid alkaline earth dihydrides are well-known [37-39]. Solid BeH_2 can be synthesized either by the reaction of $Be(CH_3)_2$ with $LiAlH_4$ in ether or by pyrolysis of $Be(C_2H_5)_2$ [37]. There are several methods for preparing solid MgH_2, including the direct reaction of solid Mg with molecular hydrogen at high pressures [37]. Solid CaH_2, SrH_2 and BaH_2 can also be prepared directly from the elements [37]. Recently, MgH_2-based materials have been proposed for hydrogen storage due to their low costs and large hydrogen-storage capacities [40,41]. Chemical properties of alkaline earth hydrides and other main-group hydrides have been reviewed recently by Aldridge and Downs [42]. The crystalline structure of solid BeH_2 is based on corner-sharing BeH_4 tetrahedra [39], while solid MgH_2 has a rutile structure, and CaH_2, SrH_2 and BaH_2 have orthorhombic $PbCl_2$-type structures [42]. All solid alkaline earth dihydrides decompose to their constituent elements at high temperatures [42], e.g., 200°C for BeH_2 and 100°C for MgH_2. Therefore, it is not possible to produce gaseous BeH_2, MgH_2, CaH_2, SrH_2 or BaH_2 molecules by vaporizing the corresponding solids.

Although gaseous BeH_2 and MgH_2 are definitely linear, the other alkaline earth dihydrides may have bent structures in the gas phase, as suggested by several ab initio calculations [43-47]. Recently, Wang and Andrews obtained infrared absorption spectra of BeH_2, MgH_2, CaH_2, SrH_2 and BaH_2 trapped in solid hydrogen and neon matrices [48-50], and provided weak evidence for the bent structures of CaH_2, SrH_2 and BaH_2. There has been no report on experimental identification of CaH_2, SrH_2 and BaH_2 molecules in the gas phase, and their bent structures have not been confirmed by experiment with certainty.

In this chapter, the discovery of gaseous BeH_2, BeD_2, MgH_2 and MgD_2 molecules, and detailed analyses of their high-resolution infrared emission spectra are reported. The molecules were generated from direct gas phase reactions of excited Be and Mg atoms with molecular hydrogen or deuterium in a furnace-discharge cell. Similar experiments were carried out for Ca, Sr and Ba metals, but proved unsuccessful. The results presented in this chapter have been previously published in Refs. [51-55].

4.2 Experiments and Results

Emission lines of BeH_2, BeD_2, MgH_2 and MgD_2 were observed in the same spectra recorded for BeH, BeD, MgH and MgD molecules, respectively, so the experimental conditions are exactly the same as those described in Chapter 2. The instrumental resolution was 0.03 cm^{-1} for BeH_2 and BeD_2 spectra, and 0.01 cm^{-1} for MgH_2 and MgD_2 spectra. The emission lines of CO (impurity) were used for absolute wavenumber calibration, as described in Chapter 2. The signal-to-noise ratios for the strongest vibration-rotation lines of BeH_2 and $^{24}MgH_2$ were 150 and 10, respectively. Lines from the minor isotopes of Mg were too weak to be observed.

The strongest molecular emission lines were assigned to the antisymmetric stretching fundamental bands, $001(\Sigma_u^+)\rightarrow000(\Sigma_g^+)$, of BeH_2, BeD_2, MgH_2 and MgD_2 for the following reasons: *a*) the observed band origins in the spectra match the peaks observed in matrix isolation experiments [15,35] if matrix shifts are taken into account, and the general appearance of the spectra (single *P* and *R* branches only) is consistent with a closed-shell $^1\Sigma_g^+$ electronic state; *b*) the rotational constants obtained from the spectra match the values predicted by ab initio theoretical calculations [8,34], and are consistent with a linear H–M–H structure; *c*) the adjacent rotational lines for MH_2 and MD_2 have alternating 3:1 and 1:2 intensity ratios, respectively, due to the *ortho-para* nuclear spin statistical weights, $(I+1)/I$, associated with hydrogen (I = ½) and deuterium (I = 1) nuclei [56]. Expanded views of BeH_2, BeD_2 and MgH_2 spectra in Figures 4.1 to 4.3 show the intensity alternations.

In addition to the antisymmetric stretching fundamental band, $001(\Sigma_u^+)\rightarrow000(\Sigma_g^+)$, the following hot bands were assigned and analyzed for BeH_2, see Figure 4.4.

$002(\Sigma_g^+)\rightarrow001(\Sigma_u^+)$, $01^11(\Pi_g)\rightarrow01^10(\Pi_u)$,
$003(\Sigma_u^+)\rightarrow002(\Sigma_g^+)$, $01^12(\Pi_u)\rightarrow01^11(\Pi_g)$,
$101(\Sigma_u^+)\rightarrow100(\Sigma_g^+)$, $11^11(\Pi_g)\rightarrow11^10(\Pi_u)$,
$02^21(\Delta_u)\rightarrow02^20(\Delta_g)$, $02^01(\Sigma_u^+)\rightarrow02^00(\Sigma_g^+)$,
$02^22(\Delta_g)\rightarrow02^21(\Delta_u)$, $02^02(\Sigma_g^+)\rightarrow02^01(\Sigma_u^+)$.

Four vibration-rotation hot bands were analyzed for BeD_2 and MgH_2,

$002(\Sigma_g^+)\rightarrow001(\Sigma_u^+)$, $01^11(\Pi_g)\rightarrow01^10(\Pi_u)$,
$02^21(\Delta_u)\rightarrow02^20(\Delta_g)$, $02^01(\Sigma_u^+)\rightarrow02^00(\Sigma_g^+)$,

and only the $001(\Sigma_u^+)\rightarrow000(\Sigma_g^+)$ fundamental band was observed for the MgD_2 molecule. Complete lists of line positions and constants have been published in Refs. [54,55].

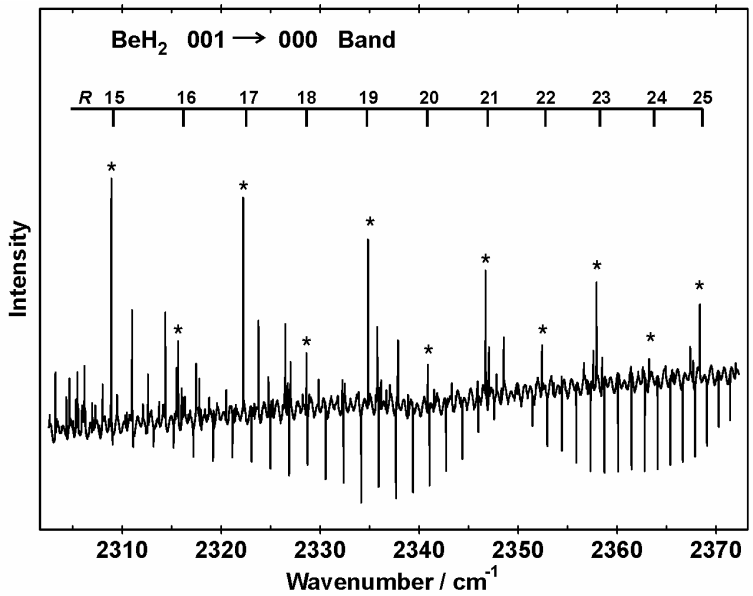

Figure 4.1. An expanded view of BeH_2 spectrum showing the 3:1 intensity alternation in the *R*-branch lines. The absorption lines are from atmospheric CO_2.

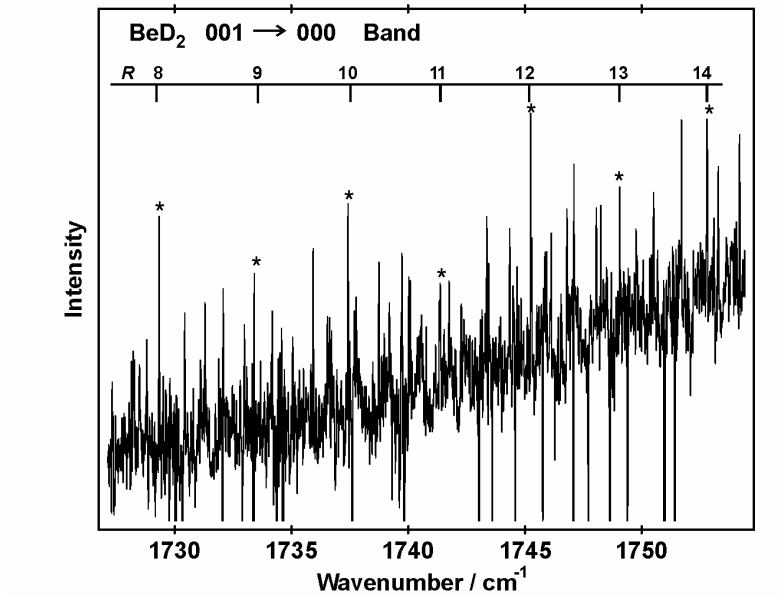

Figure 4.2. An expanded view of BeD_2 spectrum showing the 1:2 intensity alternation in the *R*-branch lines. The absorption lines are from atmospheric water vapour.

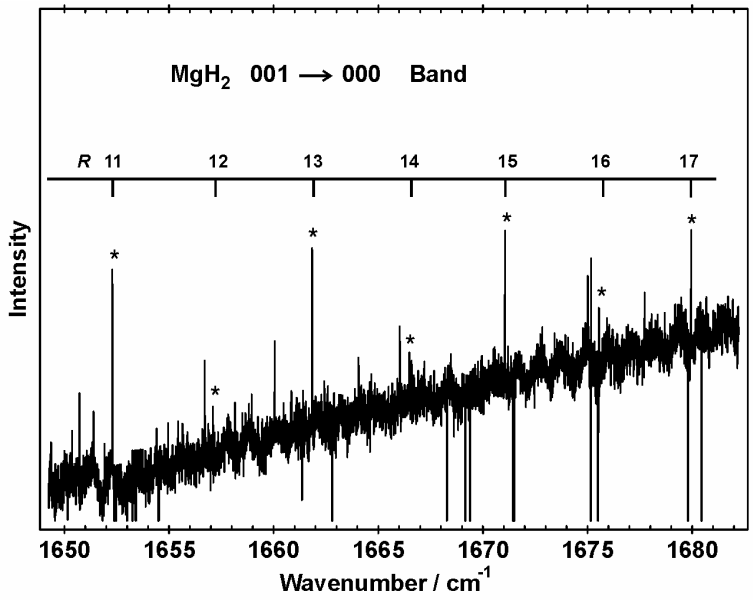

Figure 4.3. An expanded view of MgH_2 spectrum showing the 3:1 intensity alternation in adjacent rotational lines. The absorption lines are from atmospheric water vapour.

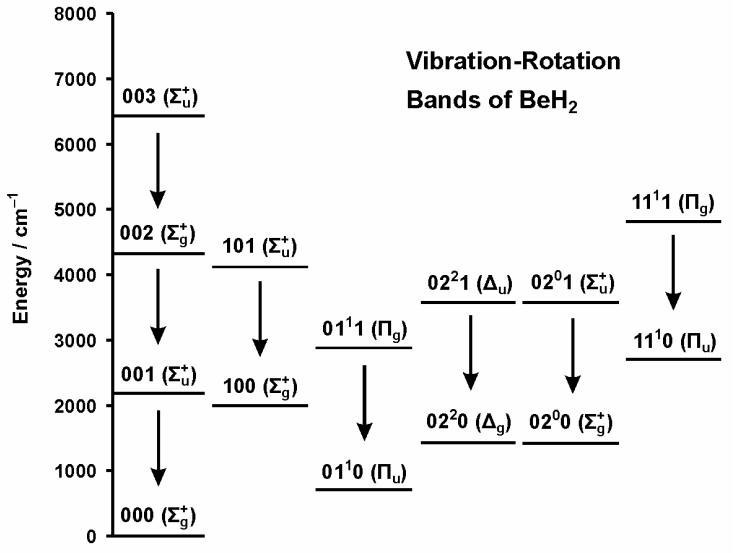

Figure 4.4. An approximate energy level diagram showing the observed vibration-rotation bands of BeH_2.

4.3 Analyses of BeH_2 and BeD_2 Spectra

The total energy of a linear triatomic molecule in its ground electronic state can be separated into vibrational and rotational parts:

$$E_{\text{vib-rot}} = G(\mathrm{v}_1, \mathrm{v}_2^{\ell}, \mathrm{v}_3) + F_{[\mathrm{v}]}(J). \tag{4.1}$$

The vibrational energy expression includes first-order harmonic and second-order anharmonic terms [56]:

$$\begin{aligned} G(\mathrm{v}_1, \mathrm{v}_2^{\ell}, \mathrm{v}_3) = {} & \omega_1\left(\mathrm{v}_1 + \tfrac{1}{2}\right) + \omega_2\left(\mathrm{v}_2 + 1\right) + \omega_3\left(\mathrm{v}_3 + \tfrac{1}{2}\right) \\ & + x_{11}\left(\mathrm{v}_1 + \tfrac{1}{2}\right)^2 + x_{22}\left(\mathrm{v}_2 + 1\right)^2 + x_{33}\left(\mathrm{v}_3 + \tfrac{1}{2}\right)^2 + g_{22}\ell^2 \\ & + x_{12}\left(\mathrm{v}_1 + \tfrac{1}{2}\right)\left(\mathrm{v}_2 + 1\right) + x_{13}\left(\mathrm{v}_1 + \tfrac{1}{2}\right)\left(\mathrm{v}_3 + \tfrac{1}{2}\right) + x_{23}\left(\mathrm{v}_2 + 1\right)\left(\mathrm{v}_3 + \tfrac{1}{2}\right). \end{aligned} \tag{4.2}$$

In this equation, v_1, v_2 and v_3 are the vibrational quantum numbers for the symmetric stretching (σ_g), bending (π_u), and antisymmetric stretching (σ_u) modes, respectively, and ℓ is the vibrational angular momentum quantum number. For the vibrational states with Σ ($\ell = 0$) or Π ($\ell = 1$) symmetry, the following expression was used for rotational energy levels [57],

$$\begin{aligned} F_{[\mathrm{v}]}(J) = {} & B\left[J(J+1) - \ell^2\right] - D\left[J(J+1) - \ell^2\right]^2 + H\left[J(J+1) - \ell^2\right]^3 \\ & \pm \frac{1}{2}\left[qJ(J+1) + q_{\mathrm{D}}J^2(J+1)^2 + q_{\mathrm{H}}J^3(J+1)^3\right], \end{aligned} \tag{4.3}$$

in which B is the inertial rotational constant, D and H are centrifugal distortion constants, and J is the total angular momentum quantum number (including rotation). The rotational ℓ-type doubling parameters, q, q_{D} and q_{H}, are zero for the Σ states, and the + (–) sign refers to the e (f) parity component of the Π states [58].

4.3.1 Vibration-rotation bands of BeH_2 and BeD_2

The absolute rotational assignment of the $001(\Sigma_u^+) \rightarrow 000(\Sigma_g^+)$ fundamental band of BeH_2 was easily obtained because all the rotational lines near the band origin were observed. The intensity alternation in adjacent rotational lines and a small local perturbation at the $J = 22$ level of the $001(\Sigma_u^+)$ state of BeH_2 further confirmed the absolute J assignment. Similarly, the rotational assignment for BeD_2 was confirmed by intensity alternation and by observation of a small perturbation at the $J = 29$ of the $001(\Sigma_u^+)$ state. Line positions of the ν_3 fundamental bands of BeH_2 and BeD_2 are listed in Tables A1 and A2 of the Appendix. The local perturbations observed in the 001 level are caused by the nearby 030 level (Π_u or Φ_u states), as both theoretical calculations [8,34] and matrix isolation experiments [15,35] had

found that the frequency of the antisymmetric stretching mode is close to three times the frequency of the bending mode, i.e., $\nu_3 \approx 3\nu_2$. Rotational lines of the $001(\Sigma_u^+) \rightarrow 000(\Sigma_g^+)$ fundamental bands were fitted using the energy expression in Eq. (4.3) with $\ell = 0$, and the ground state vibrational energy was set to zero. The rotational assignment of the $002(\Sigma_g^+) \rightarrow 001(\Sigma_u^+)$ and $003(\Sigma_u^+) \rightarrow 002(\Sigma_g^+)$ hot bands were obtained consecutively using lower state combination differences (see Chapter 1).

The second strongest bands in both BeH_2 and BeD_2 spectra had large ℓ-type doubling, and were assigned as the $01^11(\Pi_g) \rightarrow 01^10$ (Π_u) hot bands. The absolute J assignments for these bands were obtained based on the intensity alternations and the fact that e and f parity components must have the same band origins. Rotational lines of the $01^11(\Pi_g) \rightarrow 01^10(\Pi_u)$ bands were fitted using the energy expression in Eq. (4.3) with $\ell = 1$. The vibrational energy of the 01^10 level was set to zero, since only the difference between the 01^11 and 01^10 vibrational energies can be determined from these data. The rotational assignment of the $01^12(\Pi_u) \rightarrow 01^11(\Pi_g)$ hot band of BeH_2 was readily obtained using lower-state combination differences. Rotational constants and the ℓ-type doubling constants of the 01^10, 01^11 and 01^12 states are reported in Tables 4.1 and 4.2 for BeH_2 and BeD_2, respectively.

The absolute rotational assignment of the $101(\Sigma_u^+) \rightarrow 100(\Sigma_g^+)$ hot band of BeH_2 was also based on intensity alternation, and the energy expression in Eq. (4.3) with $\ell = 0$ was used to fit this band. Similar to the $01^11(\Pi_g) \rightarrow 01^10(\Pi_u)$ hot band, the unknown vibrational energy of the lower state (100, Σ_g^+) was set to zero in the least-squares fitting (see Table 4.1). The rotational constant of a particular vibrational level with v_1, v_2 and v_3 quantum numbers, $B_{[v]}$, is related to the equilibrium rotational constant (B_e) by the following linear equation, in which α_1, α_2 and α_3 are the vibration-rotation interaction constants [56]:

$$B_{[v]} = B_e - \alpha_1\left(v_1 + \tfrac{1}{2}\right) - \alpha_2\left(v_2 + 1\right) - \alpha_3\left(v_3 + \tfrac{1}{2}\right). \qquad (4.4)$$

Using the rotational constants of the 000, 100, 01^10 and 001 levels, the vibration-rotation interaction constants were determined for BeH_2. These constants were then used to predict the rotational constants of other vibrational levels. Rotational assignments of all other bands of BeH_2 were based on the $B_{[v]}$ values predicted by Eq. (4.4). Similarly, the α_2 constant of BeD_2 was used to assign the $02^21(\Delta_u) \rightarrow 02^20(\Delta_g)$ and $02^01(\Sigma_u^+) \rightarrow 02^00(\Sigma_g^+)$ bands. Band constants for most of the observed vibrational levels of BeH_2 and BeD_2 are presented in Tables 4.1 and 4.2, respectively. All vibrational levels of BeH_2 and BeD_2 with $v_2 = 2$ showed rotational ℓ-type resonance, which is described in the following section.

Table 4.1. Spectroscopic constants (in cm^{-1}) for BeH_2; all uncertainties are 1σ.

	Vibrational levels			
$^9BeH_2$	000 (Σ_g^+)	001 (Σ_u^+)	002 (Σ_g^+)	003 (Σ_u^+)
G	0.0	2178.8659(2)	4323.7828(3)	6434.1088(5)
B	4.7013985(75)	4.6321872(69)	4.5642590(69)	4.497254(11)
$10^4\ D$	1.04999(17)	1.03312(15)	1.01703(14)	0.99846(51)
$10^9\ H$	2.7175(100)	2.6317(82)	2.5717(77)	2.001(73)
$^9BeH_2$	010 (Π_u) [a]	011 (Π_g)	012 (Π_u)	
G	ν_2	2165.8133(2) + ν_2	4298.1060(3) + ν_2	
B	4.7120158(61)	4.6427478(58)	4.5747486(60)	
$10^4\ D$	1.09087(12)	1.07473(11)	1.05931(12)	
$10^9\ H$	3.0486(74)	2.9880(64)	2.9479(65)	
$10^2\ q$	–9.1406(12)	–9.0988(12)	–9.0603(12)	
$10^6\ q_D$	8.121(24)	8.035(23)	7.976(23)	
$10^{10}\ q_H$	–8.00(14)	–7.99(13)	–8.17(13)	
$^9BeH_2$	100 (Σ_g^+) [a]	101 (Σ_u^+)	110 (Π_u) [a]	111 (Π_g)
G	ν_1	2120.1532(3) + ν_1	c	2106.7877(2) + c
B	4.644418(14)	4.574112(13)	4.654489(14)	4.584194(13)
$10^4\ D$	1.04241(27)	1.02603(25)	1.08199(44)	1.06689(38)
$10^9\ H$	2.789(17)	2.656(14)	3.090(38)	3.055(32)
$10^2\ q$	…	…	–9.0219(28)	–8.9738(27)
$10^6\ q_D$	…	…	8.639(85)	8.596(76)
$10^{10}\ q_H$	…	…	–13.37(75)	–13.77(63)

[a] The wavenumbers of ν_1 and ν_2 can not be determined from the data. The best ab initio value [64] for ν_1 is 1992 cm^{-1}, and the neon matrix value [48] for ν_2 is 708.5 cm^{-1}; $c \approx \nu_1 + \nu_2$.

Table 4.2. Spectroscopic constants (in cm^{-1}) for BeD_2; all uncertainties are 1σ.

		Vibrational levels	
$^9BeD_2$	000 (Σ_g^+)	001 (Σ_u^+)	002 (Σ_g^+)
G	0.0	1689.6788(4)[a]	3356.7353(6)
B	2.360987(13)	2.330283(14)	2.299906(16)
$10^4\ D$	0.26206(28)	0.25900(31)	0.25165(41)
$10^9\ H$	0.321(18)	0.518(23)	0.288(31)

$^9BeD_2$	010 (Π_u) [a]	011 (Π_g)
G	ν_2	1680.5576(4) + ν_2
B	2.367791(18)	2.337082(19)
$10^4\ D$	0.26933(42)	0.26710(45)
$10^9\ H$	0.157(29)	0.519(33)
$10^2\ q$	–3.0175(37)	–3.0299(37)
$10^6\ q_D$	1.901(83)	2.013(89)
$10^{10}\ q_H$	–4.71(58)	–6.21(66)

[a] The neon matrix value [48] for ν_2 is 538.2 cm^{-1}.

4.3.2 Rotational ℓ-type resonance in BeH_2 and BeD_2

For all the vibrational levels of BeH_2 and BeD_2 with $v_2 = 2$, large splittings were observed between the *e* and *f* parity components of the Δ states, i.e., $02^20(\Delta_g)$, $02^21(\Delta_u)$ and $02^22(\Delta_g)$ states. These splittings are due to rotational ℓ-type resonances between these Δ states and the associated nearby Σ^+ states, $02^00(\Sigma_g^+)$, $02^01(\Sigma_u^+)$ and $02^02(\Sigma_g^+)$, respectively. The detailed theory of rotational ℓ-type resonance between Σ^+ ($\ell = 0$) and Δ ($\ell = 2$) states was first derived by Amat and Nielsen [59]. Since all the rotational levels of a Σ^+ state have *e* parity, they interact only with the *e* parity component of the nearby Δ state, and thus the Δ(*f*) levels are not perturbed. Following Maki and Lide, who analyzed rotational ℓ-type resonances for the HCN molecule [60], a 2×2 Hamiltonian matrix was used for the *e* levels, while the rotational energy expression for the *f* levels was the customary power series in $[J(J+1) - \ell^2]$ with $\ell = 2$. The 2×2 Hamiltonian matrix used for the $\Sigma^+(e)$ and $\Delta(e)$ levels, and the associated matrix elements are given in the following equations, in which $x = J(J+1)$,

$$\mathbf{H} = \begin{pmatrix} E_\Delta^0 & \sqrt{2}W_{20} \\ \sqrt{2}W_{20} & E_\Sigma^0 \end{pmatrix}, \tag{4.5}$$

$$E_\Delta^0 = G_\Delta + B_\Delta(x-4) - D_\Delta(x-4)^2 + H_\Delta(x-4)^3, \tag{4.6}$$

$$E_\Sigma^0 = (G_\Delta - 4g_{22}) + B_\Sigma x - D_\Sigma x^2 + H_\Sigma x^3, \tag{4.7}$$

$$W_{20} = \frac{1}{\sqrt{2}}\left(q + q_D x + q_H x^2\right)\sqrt{x(x-2)}, \tag{4.8}$$

and the energy expression for the Δ(*f*) levels is exactly the same as Eq. (4.6). The term $4g_{22}$ in Eq. (4.7) comes from the vibrational energy level expression in Eq. (4.2).

The Δ(*f*) component of the $02^21(\Delta_u) \rightarrow 02^20(\Delta_g)$ and $02^22(\Delta_g) \rightarrow 02^21(\Delta_u)$ bands were assigned readily using the α_2 constants obtained in the previous section, but it was difficult to distinguish the coupled $\Sigma^+(e)$ and Δ(*e*) components. The common method for assigning nearby $\Sigma^+(e)$ and Δ(*e*) states is based on the first observed line (lowest *J*) in each branch, since $J = 0$ and 1 do not exist for Δ states. For BeH_2, however, the spectrum was congested because of other overlapping bands, and it was difficult to ascertain which lines were missing. In the BeD_2 case, the low *J* lines ($J < 4$) were not observed at all because of the low signal-to-noise ratio of the spectrum. The energy level expressions in Eqs. (4.6) and (4.7) show that the separation between $\Sigma^+(e)$ and Δ(*e*) levels is approximately equal to $4[g_{22} - B]$ in the absence of perturbations, because the values of B_Σ and B_Δ should be very close to each other. The $\Sigma^+(e)$ and Δ(*e*) levels of BeH_2 were assigned based on the g_{22} constant predicted by ab

initio calculations [8]. The theoretical value [8] for the g_{22} constant of BeH_2 was 2.46 cm^{-1}, which means that [$g_{22} - B$] is negative and the rotational levels of the $02^00(\Sigma_g^+)$ state of BeH_2 lie higher than those of the $02^20(\Delta_g)$ state.

Lines from the $02^21(\Delta_u) \rightarrow 02^20(\Delta_g)$, $02^01(\Sigma_u^+) \rightarrow 02^00(\Sigma_g^+)$, $02^22(\Delta_g) \rightarrow 02^21(\Delta_u)$ and $02^02(\Sigma_g^+) \rightarrow 02^01(\Sigma_u^+)$ bands of BeH_2 were fitted using energy expressions in Eqs. (4.5) to (4.8), and the corresponding constants were determined. When the assignments of $\Sigma^+(e)$ and $\Delta(e)$ levels were switched in a separate fit, the standard deviation of the fit increased drastically. Similarly, two separate fits were performed for BeD_2, and it was found that rotational levels of the $02^00(\Sigma_g^+)$ state of BeD_2 lie lower than those of the $02^20(\Delta_g)$ state. The constants obtained from ℓ-type resonance fits of BeH_2 and BeD_2 are reported in Tables 4.3 and 4.4, respectively.

CO_2, CS_2 and BeF_2 are good examples of symmetric linear triatomic molecules for which experimental data are available for the $02^20(\Delta_g)$ and $02^00(\Sigma_g^+)$ states [61-63]. There is no ambiguity in the assignments for these molecules because their $02^00(\Sigma_g^+)$ states are in strong Fermi resonance with the nearby $10^00(\Sigma_g^+)$ states, and thus lie much lower in energy compared to the $02^20(\Delta_g)$ states. It is interesting to note that the relative locations of the rotational levels of the $02^00(\Sigma_g^+)$ and $02^20(\Delta_g)$ states are opposite for BeH_2 and BeD_2. This is simply because the g_{22} constants for BeH_2 and BeD_2 have similar values, but the B value of BeH_2 is almost twice as large as that of BeD_2. The g_{22} constant of BeD_2 is just slightly larger than its B value, causing the Δ state rotational levels to be above those of the Σ^+ state. These assignments for the relative positions of the Δ and the Σ^+ states of BeH_2 and BeD_2 are very strongly supported by recent ab initio calculations of Li and Le Roy [64], because the g_{22} values predicted by their calculations differ from those of Tables 4.3 and 4.4 by less than 0.02 cm^{-1}. There is also a small vibrational dependence for the g_{22} constants, as implied by the constants of Tables 4.3 and 4.4.

Small local perturbations (at J = 18 to 23) were observed in the 021 vibrational level (Σ_u^+ and Δ_u) of BeH_2, and are caused by the nearby 050 vibrational level. The 050 level has three states with Π_u, Φ_u and H_u symmetries, but it is not possible to ascertain which state is causing these perturbations using these data. The total energies of the perturbed rotational levels were fitted as individual term values, and are not listed here. Complete lists of line positions and constants for BeH_2 and BeD_2 have been published in the supplementary tables of Ref. [55].

Table 4.3. Spectroscopic constants (in cm^{-1}) for the rotational ℓ-type resonance in BeH_2; all uncertainties are 1σ.

	Vibrational levels		
$^9BeH_2$	020 [a]	021	022
G_Δ	a	2152.6898(5) + a	4272.3113(9) + a
g_{22}	2.6412(29)	2.6107(29)	2.5816(29)
B_Δ	4.721519(23)	4.652203(22)	4.584109(37)
$10^4\ D_\Delta$	1.13373(52)	1.11828(50)	1.1012(22)
$10^9\ H_\Delta$	3.586(35)	3.549(32)	3.33(42)
B_Σ	4.723694(38)	4.654358(37)	4.586316(57)
$10^4\ D_\Sigma$	1.13964(93)	1.12318(86)	1.1104(34)
$10^9\ H_\Sigma$	3.701(64)	3.563(56)	3.99(67)
$10^2\ q$	–9.1924(31)	–9.1482(30)	–9.1053(36)
$10^6\ q_D$	8.378(62)	8.334(58)	8.31(16)
$10^{10}\ q_H$	–8.17(38)	–8.46(34)	–10.8(32)

[a] The absolute vibrational energy of the 020 level can not be determined from the data; $a \approx 2\nu_2$.

Table 4.4. Spectroscopic constants (in cm^{-1}) for the rotational ℓ-type resonance in BeD_2; all uncertainties are 1σ.

	Vibrational levels	
$^9BeD_2$	020 [a]	021
G_Δ	b	1671.4484(21) + b
g_{22}	2.5276(85)	2.5134(89)
B_Δ	2.374187(49)	2.343354(54)
$10^4\ D_\Delta$	0.2757(6)	0.2690(7)
B_Σ	2.374879(89)	2.344138(94)
$10^4\ D_\Sigma$	0.2804(11)	0.2758(12)
$10^2\ q$	–2.9795(43)	–2.9858(43)
$10^6\ q_D$	1.199(54)	1.157(55)

[a] The absolute vibrational energy of the 020 level can not be determined from the data; $b \approx 2\nu_2$.

4.3.3 Internuclear distances of BeH_2 and BeD_2

The B_{000} constants of BeH_2 and BeD_2, taken from Tables 4.1 and 4.2, were used to determine the r_0 internuclear distances directly from the moment of inertia equation, Eq. (1.28). The r_0 values obtained for BeH_2 and BeD_2 are 1.333758(1) Å and 1.331361(4) Å, respectively. Their difference is in the fourth significant figure, and is due to the fact that the 000 ground state of BeD_2 lies lower than that of BeH_2 on the potential energy surface.

The vibration-rotation interaction constants (α_1, α_2 and α_3 in Eq. (4.4)) were determined for BeH_2 by taking the differences between the ground state rotational constant (B_{000}) and the $B_{[v]}$ values of the 100, 01^10 and 001 states, respectively. The equilibrium rotational constant (B_e) was then calculated for BeH_2 using its B_{000} value and the three α_i values. Similarly, the equilibrium centrifugal distortion constant (D_e) of BeH_2 was calculated using a linear equation analogous to Eq. (4.4) for the $D_{[v]}$ values. Using the B_e value of 4.753877(25) cm^{-1}, the equilibrium Be–H internuclear distance (r_e) was determined to be 1.326376(3) Å for BeH_2. However, only α_2 and α_3 could be determined for the BeD_2 isotopologue, and an independent determination of r_e was not possible for BeD_2.

In polyatomic molecules for which equilibrium internuclear distances are not available, it is common to calculate the average r_s structure by using the moments of inertia of isotopically substituted molecules [65-68]. The experimental data for BeH_2 were sufficient to determine its equilibrium internuclear distance (r_e), and an average r_s structure was not necessary. However, an average r_s distance was calculated for this molecule for comparison with the r_0 and r_e distances. The following equation [67] was used to estimate r_s:

$$I_0^{\mathrm{D}} - I_0^{\mathrm{H}} = 2r_s^2\left(m_{\mathrm{D}} - m_{\mathrm{H}}\right). \qquad (4.9)$$

In this equation, I_0^{D} and I_0^{H} are the moments of inertia calculated from the B_{000} values of BeD_2 and BeH_2, respectively, and m_{D} and m_{H} are the atomic masses for deuterium and hydrogen. The average r_s distance calculated from Eq. (4.9) is 1.32896 Å, which lies between the r_0 and r_e values, qualitatively consistent with the predictions of Watson [68] for relative magnitudes of r_0, r_s and r_e.

4.3.4 Vibrational analyses for BeH_2 and BeD_2

A few anharmonicity constants in Eq. (4.2) were directly calculated from the experimental band origins. The x_{13} constant was obtained for BeH_2 by taking the difference between the 101→100 and 001→000 band origins. Similarly, the x_{23} constants of BeH_2 and BeD_2 were calculated by taking the difference between the $01^11 \rightarrow 01^10$ and 001→000 band origins. Furthermore, the difference between the 002→001 and 001→000 band origins is equal to $2x_{33}$, see Eq. (4.2).

The equilibrium vibrational frequency of the antisymmetric stretching mode (ω_3) was calculated for BeH_2 using the equation,

$$\nu_3(\text{obs.}) = G_{001} - G_{000} = \omega_3 + \tfrac{1}{2} x_{13} + x_{23} + 2x_{33}, \qquad (4.10)$$

which is derived from Eq. (4.2). The equilibrium vibrational frequency of the symmetric stretching mode (ω_1) was estimated using Kratzer's equation, which applies to diatomic and symmetric linear triatomic molecules [57]:

$$D_e \approx \frac{4B_e^3}{\omega_1^2}. \qquad (4.11)$$

The B_e and D_e constants of BeH_2 were used to estimated ω_1. The bending mode vibrational frequency (ω_2) was also estimated for BeH_2 by solving the following equation that relates the ℓ-type doubling constant to B_e, ω_2 and ω_3 [69,70]:

$$q_{010} \approx \frac{-2B_e^2}{\omega_2}\left(1 + \frac{4\omega_2^2}{\omega_3^2 - \omega_2^2}\right). \qquad (4.12)$$

The molecular constants obtained for BeH_2 and BeD_2 are listed in Table 4.5, and are compared with the corresponding values predicted by ab initio calculations.

Table 4.5. Molecular constants of BeH_2 and BeD_2 (in cm^{-1}).

Const.	BeH_2 This Work	BeH_2 Ref. [64]	BeH_2 Ref. [71]	BeH_2 Ref. [8]	BeD_2 This Work	BeD_2 Ref. [64]	BeD_2 Ref. [71]
B_{000}	4.701399(8)	4.7023	4.70407	4.65979	2.36099(2)	2.36034	2.36115
r_0 / Å	1.333758(1) [a]	1.3336	1.33338	1.3397	1.331361(4)	1.33154	1.33131
α_1	0.05698(2)		0.05705	0.05576	…		0.02002
α_2	–0.01062(1)		–0.01067	–0.01183	–0.00680(2)		–0.00687
α_3	0.06921(1)		0.06936	0.06996	0.03070(2)		0.03072
B_e	4.75388(2)			4.71117	…		
r_e / Å	1.326376(3)	1.3265	1.32618	1.3324	…	1.3265	1.32618
$10^4 D_e$	1.0213(5)			1.0079	…		
$10^9 H_e$	2.39(3)			2.5	…		
q_{010}	–0.09141(1)	–0.09148	–0.09154	–0.00271	–0.03018(4)	–0.02985	–0.02987
$\nu_1(\sigma_g)$	…	1991.97	1991.48	1979.6	…	1425.24	1424.83
$\nu_2(\pi_u)$	…	711.77	716.24	716.8	…	548.36	550.50
$\nu_3(\sigma_u)$	2178.8659(2)	2178.79	2178.70	2167.2	1689.6788(4)	1689.27	1689.23
$\omega_1(\sigma_g)$	2051 [b]		2052.22	2037.3	…		1450.59
$\omega_2(\pi_u)$	717 [c]		717.18	717.7	…		551.31
$\omega_3(\sigma_u)$	2255.224(1)		2254.75	2249.4	…		1736.26
x_{11}	…		–15.16	–14.29	…		–7.05
x_{12}	…		–1.25	1.80	…		3.73
x_{13}	–58.7127(3)		–58.35	–61.84	…		–30.79
x_{22}	…		–0.40	–0.52	…		–1.06
x_{23}	–13.0527(3)		–12.99	–11.68	–9.1212(5)		–9.05
x_{33}	–16.9745(3)		–16.94	–19.78	–11.3111(5)		–11.29
g_{22}	2.641(3)	2.65		2.46	2.528(9)	2.54	

[a] The numbers in parentheses are one standard deviation statistical uncertainties, calculated by propagation of errors.

[b] Estimated from B_e and D_e, using Eq. (4.11).

[c] Estimated from q_{010}, B_e and ω_3, using Eq. (4.12).

4.4 Analyses of MgH_2 and MgD_2 Spectra

4.4.1 Vibration-rotation bands of MgH_2 and MgD_2

The rotational assignment of the $001(\Sigma_u^+)\rightarrow000(\Sigma_g^+)$ fundamental band of MgH_2 was confirmed by the 3:1 intensity alternation in the adjacent rotational lines, and the $002(\Sigma_g^+)\rightarrow001(\Sigma_u^+)$ hot band was assigned using lower state combination differences. The MgD_2 lines were very weak, and only the $001(\Sigma_u^+)\rightarrow000(\Sigma_g^+)$ fundamental band was observed for this isotopologue. Line positions of the ν_3 fundamental bands of $^{24}MgH_2$ and $^{24}MgD_2$ are listed in Tables A3 and A4 of the Appendix. The $01^11(\Pi_g)\rightarrow01^10$ (Π_u) hot band of MgH_2 was assigned based on the large ℓ-type doubling between the e and f parity components of the Π states. The rotational energy level expression in Eq. (4.3) with $\ell = 0$ for the Σ states and $\ell = 1$ for the Π states was used to fit the vibration-rotation bands of MgH_2 and MgD_2. The band constants for the observed vibrational levels of MgH_2 and MgD_2 are listed in Tables 4.6 and 4.7, respectively. Unlike the BeH_2 and BeD_2 molecules, no perturbation was observed in the $001(\Sigma_u^+)$ levels of MgH_2 and MgD_2.

4.4.2 Rotational ℓ-type resonance in MgH_2

Similar to the BeH_2 and BeD_2 molecules, rotational ℓ-type resonance was observed in the $02^21(\Delta_u)\rightarrow02^20(\Delta_g)$ and $02^01(\Sigma_u^+)\rightarrow02^00(\Sigma_g^+)$ bands of MgH_2. The energy level expressions in Eqs. (4.5) to (4.8) were used to fit these bands. The low J rotational lines ($J < 3$) were not observed due to the low signal-to-noise ratio of the spectrum, and the relative assignments of the $\Sigma^+(e)$ and $\Delta(e)$ levels were difficult to obtain. There was also no ab initio theoretical value for the g_{22} constant of MgH_2 available in the literature. Both assignments were tried, and only one of them resulted in a satisfactory fit. The constants obtained from this fit are listed in Table 4.8. Similar to the BeH_2 molecule, the g_{22} constant of MgH_2 was found to be smaller than its B value, which means that the $02^00(\Sigma_g^+)$ state rotational levels lie higher than those of the $02^20(\Delta_g)$ state.

Table 4.6. Spectroscopic constants (in cm^{-1}) for MgH_2; all uncertainties are 1σ.

		Vibrational levels	
$^{24}MgH_2$	000 (Σ_g^+)	001 (Σ_u^+)	002 (Σ_g^+)
G	0.0	1588.6716(2)	3165.4200(5)
B	2.882607(11)	2.848667(11)	2.815078(13)
$10^5\,D$	3.9178(25)	3.8919(28)	3.8664(39)
$10^{10}\,H$	6.49(17)	6.53(21)	6.57(35)

$^{24}MgH_2$	010 (Π_u) [a]	011 (Π_g)
G	ν_2	1582.6615(3) + ν_2
B	2.891475(15)	2.857418(15)
$10^5\,D$	4.0863(47)	4.0579(50)
$10^{10}\,H$	7.20(45)	6.84(52)
$10^2\,q$	–5.0460(19)	–4.9976(20)
$10^6\,q_D$	3.239(29)	3.212(33)

[a] The neon matrix value [49] for ν_2 is 450.4 cm^{-1}.

Table 4.7. Spectroscopic constants (in cm^{-1}) for MgD_2; all uncertainties are 1σ.

	Vibrational levels	
$^{24}MgD_2$	000 (Σ_g^+)	001 (Σ_u^+)
G	0.0	1176.5028(5)
B	1.446575(14)	1.433237(14)
$10^5\,D$	0.95872(92)	0.95221(94)

4.4.3 Internuclear distances of MgH_2 and MgD_2

The B_{000} constants of MgH_2 and MgD_2, taken from Tables 4.6 and 4.7, were used to determine the r_0 internuclear distances. The r_0 values obtained for MgH_2 and MgD_2 are 1.703327(3) Å and 1.700874(8) Å, respectively, their difference being in the fourth significant figure. A few vibration-rotation interaction constants (α_2 and α_3 for MgH_2 and only α_3 for MgD_2) were determined from the $B_{[v]}$ values of the 000, 01^10 and 001 states. It was not possible to determine the equilibrium rotational constant (B_e) and the equilibrium internuclear distance (r_e) for MgH_2 because α_1 was not determined. An average r_s distance was determined for this molecule using Eq. (4.9). The moments of inertia, I_0^D and I_0^H, were calculated from the B_{000} values of MgD_2 and MgH_2, respectively, and an average r_s distance of 1.69841 Å was obtained.

4.4.4 Vibrational analyses for MgH_2 and MgD_2

Two anharmonicity constants in Eq. (4.2), i.e., x_{23} and x_{33}, were determined for MgH_2 from the experimental band origins. It was not possible to determine ω_3 because the x_{13} constant was not available. In order to estimate the vibrational frequencies of the symmetric stretching (ω_1) and bending (ω_2) modes from Eqs. (4.11) and (4.12), respectively, the equilibrium constants B_e, D_e and ω_3 were required. However, these constants were not available for MgH_2 and MgD_2. A few molecular constants obtained for MgH_2 and MgD_2 are listed in Table 4.9, and compared with the corresponding constants predicted by ab initio calculations.

Table 4.8. Spectroscopic constants (in cm^{-1}) for the rotational ℓ-type resonance in MgH_2; all uncertainties are 1σ.

	Vibrational levels	
$^{24}MgH_2$	020 [a]	021
G_Δ	a	1576.5725(8) + a
g_{22}	0.8007(91)	0.7935(91)
B_Δ	2.899710(33)	2.865577(34)
$10^5\ D_\Delta$	4.1742(50)	4.1530(57)
B_Σ	2.900666(58)	2.866519(59)
$10^5\ D_\Sigma$	4.2343(88)	4.2094(89)
$10^2\ q$	–5.0713(62)	–5.0200(61)
$10^6\ q_D$	3.153(66)	3.052(65)

[a] The absolute vibrational energy of the 020 level can not be determined from the data; $a \approx 2\nu_2$.

Table 4.9. Molecular constants of MgH_2 and MgD_2 (in cm^{-1}).

	MgH_2	MgH_2	MgD_2	MgD_2
Const.	This Work	ab initio, Ref. [33]	This Work	ab initio, Ref. [33]
B_{000}	2.882607(11)		1.446575(14)	
r_0 / Å	1.703327(3) [a]		1.700874(8)	
α_2	–0.00887(2)		…	
α_3	0.03394(2)		0.01334(2)	
r_e / Å	…	1.7096	…	1.7096
q_{010}	–0.05046(2)		…	
$\nu_1(\sigma_g)$	…	1552.42	…	1108.38
$\nu_2(\pi_u)$	…	433.74	…	318.72
$\nu_3(\sigma_u)$	1588.6716(2)	1575.55	1176.5028(5)	1166.53
x_{23}	–6.0100(4)		…	
x_{33}	–5.9616(4)		…	
g_{22}	0.8007(91)		…	

[a] The numbers in parentheses are one standard deviation statistical uncertainties, calculated by propagation of errors.

4.5 Discussion

4.5.1 Comparison with theoretical predictions

Very high level ab initio theoretical calculations have been performed recently for BeH_2, BeD_2 and BeHD [64,71]. Li and Le Roy [64] computed the potential energy for the ground electronic state of BeH_2 at 6864 points using the multi-reference configuration interaction (MRCI) method with very large basis sets. The potential energy surface was constructed from the ab initio points, and the vibration-rotation energy levels were obtained for $J = 0$ to 8 of BeH_2, BeD_2 and BeHD by solving the exact vibration-rotation Schrödinger equation variationally on this surface [64]. The molecular constants of BeH_2 and BeD_2 obtained from the ab initio calculations of Li and Le Roy [64] are listed in Table 4.5. The agreement between the theoretical constants and the experimental constants determined in the present work is very striking. For example, theoretical values for the ν_3 fundamental of BeH_2 and BeD_2 are 2178.8 cm^{-1} and 1689.3 cm^{-1}, respectively, which differ from experimental values by less than 0.4 cm^{-1}. The ab initio calculations of Koput and Peterson [71] were very similar to those of Li and Le Roy [64]. They computed the potential energy at 215 points using a coupled-cluster method (CCSD(T)) and obtained the vibration-rotation energy levels (for $J =$ 0 to 4) variationally. The theoretical constants reported by Koput and Peterson [71] are also in excellent agreement with experiment (see Table 4.5). In another theoretical study, Martin and Lee [8] used the CCSD(T) method for the ground state potential energy, and determined the force constants of BeH_2 from 25 ab initio points. Analytic formulae obtained from second-order perturbation theory were then used to calculate the spectroscopic constants of BeH_2 from the force constants [8]. Theoretical constants of Martin and Lee [8] are also listed in Table 4.5 for comparison.

The molecular constants of MgH_2, MgD_2 and HMgD have been computed by Li et al. [33] using a variational method similar to the calculations of Li and Le Roy [64]. However, only the vibrational energies at $J = 0$ were computed for MgH_2, MgD_2 and MgHD. A few molecular constants obtained from these calculations are listed in Table 4.9. The theoretical and experimental constants of MgH_2 and MgD_2 are reasonably close to each other, but the agreement is definitely not as good as the one for BeH_2 and BeD_2. For example, theoretical values for the ν_3 fundamental of MgH_2 and MgD_2 are 1575.6 cm^{-1} and 1166.5 cm^{-1}, respectively, which differ from experimental values by 13.1 cm^{-1} and 10.0 cm^{-1}, respectively.

4.5.2 Relative stabilities of gaseous BeH_2 and MgH_2

A combination of experimental and theoretical data can be used to estimate the dissociation energies of the metal-hydrogen bonds in gaseous BeH_2 and MgH_2. The best ab initio theoretical values for the heats of formation of gaseous BeH_2 and MgH_2 from metal vapour and molecular hydrogen are –37.6 and +3.6 kcal/mol, respectively [9,33]. On the other hand, the experimental value for the dissociation energy of H_2 is 103.3 kcal/mol [72], and those for BeH and MgH free radicals are 46.9 and 29.3 kcal/mol, respectively [73,74]. It is straightforward to calculate the dissociation energy of the first metal-hydrogen bond in BeH_2 or MgH_2 from the information given above. Therefore, the bond dissociation energies for BeH_2 are the following:

$$BeH_2(g) \rightarrow BeH(g) + H(g) \qquad \Delta E = 94.0 \text{ kcal/mol},$$

$$BeH(g) \rightarrow Be(g) + H(g) \qquad \Delta E = 46.9 \text{ kcal/mol}.$$

Note that the energy required to break the first Be–H bond in BeH_2 is twice as large as that for the second bond. A similar phenomenon is observed for the MgH_2 molecule:

$$MgH_2(g) \rightarrow MgH(g) + H(g) \qquad \Delta E = 70.4 \text{ kcal/mol},$$

$$MgH(g) \rightarrow Mg(g) + H(g) \qquad \Delta E = 29.3 \text{ kcal/mol}.$$

The other dihydrides of Group 2 elements, i.e., CaH_2, SrH_2 and BaH_2, have not been detected in the gas phase yet, and our efforts to generate these molecules were unsuccessful. A recent ab initio calculation on CaH_2 [47] predicted a total atomization energy of 100.1 kcal/mol for this molecule, while the experimental dissociation energy of the CaH free radical is 39.4 kcal/mol [75]. Thus, the energy required to break the first Ca–H bond in CaH_2 is about 50% larger than that for the second bond:

$$CaH_2(g) \rightarrow CaH(g) + H(g) \qquad \Delta E = 60.7 \text{ kcal/mol},$$

$$CaH(g) \rightarrow Ca(g) + H(g) \qquad \Delta E = 39.4 \text{ kcal/mol}.$$

Based on the dissociation energy of the first metal-hydrogen bond, the relative stabilities of gaseous alkaline earth dihydrides decrease from BeH_2 to CaH_2. The relative energies of gaseous MH and MH_2 molecules (M = Be, Mg and Ca) are compared in a simple diagram in Figure 4.5.

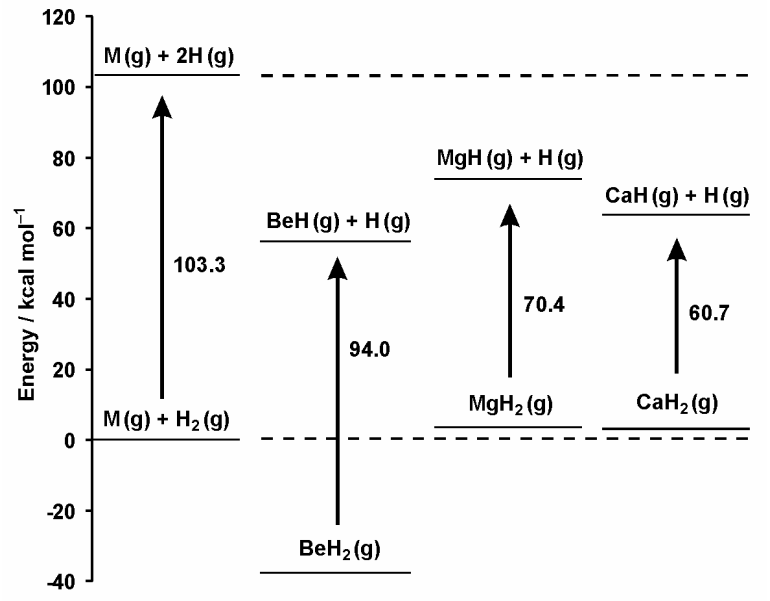

Figure 4.5. A diagram showing the relative energies of Group 2 monohydride and dihydride molecules in the gas phase. For each metal (M), the energy of the ground state M(g) + H_2(g) was taken as zero.

4.6 Summary

Gaseous BeH_2, BeD_2, MgH_2 and MgD_2 molecules were discovered, and their high-resolution infrared emission spectra were recorded with a Fourier transform spectrometer. The ν_3 antisymmetric stretching fundamental band and several hot bands in the ν_3 region were rotationally analyzed, and spectroscopic constants were obtained. Using the rotational constants of the 000 ground states, the r_0 internuclear distances were determined to be 1.333758(1) Å, 1.331361(4) Å, 1.703327(3) Å and 1.700874(8) Å for $^9BeH_2$, $^9BeD_2$, $^{24}MgH_2$ and $^{24}MgD_2$, respectively. Rotational ℓ-type doubling and ℓ-type resonance were observed in some vibration-rotation bands of BeH_2, BeD_2 and MgH_2, and the equilibrium vibrational frequencies (ω_1, ω_2 and ω_3) were estimated using Eqs. (4.10) to (4.12). Rotational constants of the 000, 100, 01^10 and 001 levels were used to determine the equilibrium rotational constant (B_e) for BeH_2, and the associated equilibrium internuclear distance (r_e) was calculated to be 1.326376(3) Å.

4.7 References

[1] S.R. Radel, M.H. Navidi, *Chemistry*, West Publishing Co., St. Paul, MN (1990).

[2] W.D. Laidig, R.J. Bartlett, Chem. Phys. Lett. 104 (1984) 424-430.

[3] H. Nakano, J. Chem. Phys. 99 (1993) 7983-7992.

[4] U.S. Mahapatra, B. Datta, D. Mukherjee, J. Chem. Phys. 110 (1999) 6171-6188.

[5] D.A. Mazziotti, Phys. Rev. A. 60 (1999) 4396-4408.

[6] M. Hanrath, , J. Chem. Phys. 123 (2005) 084102:1-12.

[7] J.A. Pople, B.T. Luke, M.J. Frisch, J.S. Binkley, J. Phys. Chem. 89 (1985) 2198-2203.

[8] J.M.L. Martin, T.J. Lee, Chem. Phys. Lett. 200 (1992) 502-510.

[9] J.M.L. Martin, Chem. Phys. Lett. 273 (1997) 98-106.

[10] S. Budavari, M.J. O'Neil, A. Smith, P.E. Heckelman, *The Merck Index*, 11th ed., Merck & Co. Inc., Rahway, NJ (1989).

[11] R.P. Blickensderfer, K.D. Jordan, N. Adams, W.H. Breckenridge, J. Phys. Chem. 86 (1982) 1930-1932.

[12] V. Kello, A.J. Sadlej, Theor. Chim. Acta. 81 (1992) 417-424.

[13] J. Hinze, O. Friedrich, A. Sundermann, Mol. Phys. 96 (1999) 711-718.

[14] S.B. Sharp, G.L. Gellene, J. Phys. Chem. A. 104 (2000) 10951-10957.

[15] T.J. Tague, Jr., L. Andrews, J. Am. Chem. Soc. 115 (1993) 12111-12116.

[16] N. Adams, W.H. Breckenridge, J. Simons, Chem. Phys. 56 (1981) 327-335.

[17] P. Chaquin, A. Sevin, H. Yu, J. Phys. Chem. 89 (1985) 2813-2818.

[18] Y.-R. Ou, D.-K. Liu, K.-C. Lin, J. Chem. Phys. 108 (1998) 1475-1484.

[19] Y.-R. Ou, Y.-M. Hung, K.-C. Lin, J. Phys. Chem. A 103 (1999) 7938-7948.

[20] Y.-M. Hung, K.-C. Lin, J. Phys. Chem. A 105 (2001) 41-47.

[21] W.H. Breckenridge, H. Umemoto, J. Chem. Phys. 75 (1981) 698-703.

[22] W.H. Breckenridge, J. Stewart, J. Chem. Phys. 77 (1982) 4469-4473.

[23] W.H. Breckenridge, H. Umemoto, J. Chem. Phys. 80 (1984) 4168-4176.

[24] P.D. Kleiber, A.M. Lyyra, K.M. Sando, S.P. Heneghan, W.C. Stwalley, Phys. Rev. Lett. 54 (1985) 2003-2006.

[25] P.D. Kleiber, A.M. Lyyra, K.M. Sando, V. Zafiropulos, W.C. Stwalley, J. Chem. Phys. 85 (1986) 5493-5504.

[26] W.H. Breckenridge, J.-H. Wang, Chem. Phys. Lett. 137 (1987) 195-200.

[27] W.H. Breckenridge, J.-H. Wang, Chem. Phys. Lett. 139 (1987) 28-34.

[28] K.-C. Lin, C.-T. Huang, J. Chem. Phys. 91 (1989) 5387-5391.

[29] D.-K. Liu, T.-L. Chin, K.-C. Lin, Phys. Rev. A 50 (1994) 4891-4898.

[30] W.H. Breckenridge, J. Phys. Chem. 100 (1996) 14840-14855.

[31] D.-K. Liu, K.-C. Lin, Chem. Phys. Lett. 274 (1997) 37-40.

[32] R. Ahlrichs, F. Keil, H. Lischka, W. Kutzelnigg, V. Staemmler, J. Chem. Phys. 63 (1975) 455-463.

[33] H. Li, D. Xie, H. Guo, J. Chem. Phys. 121 (2004) 4156-4163.

[34] G.S. Tschumper, H.F. Schaefer, J. Chem. Phys. 108 (1998) 7511-7515.

[35] T.J. Tague, Jr., L. Andrews, J. Phys. Chem. 98 (1994) 8611-8616.

[36] J.G. McCaffrey, J.M. Parnis, G.A. Ozin, W.H. Breckenridge, J. Phys. Chem. 89 (1985) 4945-4950.

[37] E. Wiberg, E. Amberger, *Hydrides of the Elements of Main Groups I-IV*, Elsevier, Amsterdam (1971).

[38] G.J. Brendel, E.M. Marlett, L.M. Niebylski, Inorg. Chem. 17 (1978) 3589-3592.

[39] G.S. Smith, Q.C. Johnson, D.K. Smith, D.E. Cox, R.L. Snyder, R.-S. Zhou, A. Zalkin, Solid State Commun. 67 (1988) 491-494.

[40] M. Tsuda, W.A. Diño, H. Kasai, H. Nakanishi, Appl. Phys. Lett. 86 (2005) 213109:1-3.

[41] S.R. Johnson, P.A. Anderson, P.P. Edwards, I. Gameson, J.W. Prendergast, M. Al-Mamouri, D. Book, I.R. Harris, J.D. Speight, A. Walton, Chem. Commun. (2005) 2823-2825.

[42] S. Aldridge, A.J. Downs, Chem. Rev. 101 (2001) 3305-3365.

[43] M. Kaupp, P.v.R. Schleyer, H. Stoll, H. Preuss, J Chem. Phys. 94 (1991) 1360-1366.

[44] I. Bytheway, R.J. Gillespie, T.-H. Tang, R.F.W. Bader, Inorg. Chem. 34 (1995) 2407-2414.

[45] T.S. Fujii, S. Iwata, Chem. Phys. Lett. 251 (1996) 150-156.

[46] L.V. Szentpály, J. Phys. Chem. A. 106 (2002) 11945-11949.

[47] J. Koput, J. Phys. Chem. A. 109 (2005) 4410-4414.

[48] X. Wang, L. Andrews, Inorg. Chem. 44 (2005) 610-614.

[49] X. Wang, L. Andrews, J. Phys. Chem. A. 108 (2004) 11511-11520.

[50] X. Wang, L. Andrews, J. Phys. Chem. A. 108 (2004) 11500-11510.

[51] P.F. Bernath, A. Shayesteh, K. Tereszchuk, R. Colin, Science 297 (2002) 1323-1324.

[52] A. Shayesteh, K. Tereszchuk, P.F. Bernath, R. Colin, J. Chem. Phys. 118 (2003) 3622-3627.

[53] A. Shayesteh, D.R.T. Appadoo, I. Gordon, P.F. Bernath, J. Chem. Phys. 119 (2003) 7785-7788.

[54] A. Shayesteh, D.R.T. Appadoo, I. Gordon, P.F. Bernath, Can. J. Chem. 82 (2004) 947-950.

[55] A. Shayesteh, P.F. Bernath, J. Chem. Phys. 124 (2006) 156101:1-2.

[56] P.F. Bernath, *Spectra of Atoms and Molecules*, 2nd ed., Oxford University Press, New York (2005).

[57] G. Herzberg, *Molecular Spectra and Molecular Structure II. Infrared and Raman Spectra of Polyatomic Molecules*, Krieger, Malabar, FL (1991).

[58] G. Herzberg, Rev. Mod. Phys. 14 (1942) 219-223.

[59] G. Amat, H.H. Nielsen, J. Mol. Spectrosc. 2 (1958) 163-172.

[60] A.G. Maki, Jr., D.R. Lide, Jr., J. Chem. Phys. 47 (1967) 3206-3210.

[61] S.A. Tashkun, V.I. Perevalov, J.-L. Teffo, L.S. Rothman, V.G. Tyuterev, J. Quant. Spectrosc. Radiat. Transfer 60 (1998) 785-801.

[62] G. Blanquet, E. Baeten, I. Cauuet, J. Walrand, C.P. Courtoy, J. Mol. Spectrosc. 112 (1985) 55-70.

[63] S. Yu, A. Shayesteh, P.F. Bernath, J. Koput, J. Chem. Phys. 123 (2005) 134303:1-8.

[64] H. Li, R.J. Le Roy, J. Chem. Phys. (2006) in press.

[65] J. Kraitchman, Am. J. Phys. 21 (1953) 17-24.

[66] C.C. Costain, J. Chem. Phys. 29 (1958) 864-874.

[67] A. Chutjian, J. Mol. Spectrosc. 14 (1964) 361-370.

[68] J.K.G. Watson, J. Mol. Spectrosc. 48 (1973) 479-502.

[69] D. Papoušek, M.R. Aliev, *Molecular Vibrational-Rotational Spectra*, Elsevier, Amsterdam (1982).

[70] J.K.G. Watson, Can. J. Phys. 79 (2001) 521-532.

[71] J. Koput, K.A. Peterson, J. Chem. Phys. (2006) submitted.

[72] K.P. Huber, G. Herzberg, *Molecular Spectra and Molecular Structure IV. Constants of Diatomic Molecules*, Van Nostrand, New York (1979).

[73] R. Colin, D. De Greef, Can. J. Phys. 53 (1975) 2142-2169.

[74] W. J. Balfour, B. Lindgren, Can. J. Phys. 56 (1978) 767-779.

[75] H. Martin, J. Chem. Phys. 88 (1988) 1797-1806.

Chapter 5

Infrared Emission Spectra of ZnH_2 and HgH_2

5.1 Introduction

Mercury and its compounds have been studied extensively as toxic chemicals in the environment [1-5]. Two major anthropogenic sources of mercury in the environment are coal combustion and waste incineration [1]. Mercury in the atmosphere exists mainly as neutral Hg vapour, whereas mercuric salts and methyl-mercury compounds can be found in natural waters and sediments [4]. Anaerobic bacteria in natural waters can reduce Hg(II) to Hg^0, which is re-emitted to the atmosphere as vapour phase elemental mercury [5,6]. The reduction of Hg(II) to Hg^0, followed by the gas phase detection of atomic mercury, is in fact the most commonly used method for detecting trace amounts of mercury in liquid and solid samples. The method is called "cold vapour generation", which was developed in the late 1960's, and is based on the reduction of aqueous Hg(II) by $SnCl_2$ or $NaBH_4$ and detection of gas phase Hg^0 by atomic absorption spectroscopy [7,8]. A similar technique called "hydride generation" is based on the reduction of acidified solutions of Group 13, 14, 15 and 16 elements by $NaBH_4$ to form volatile hydrides, which can be detected in the gas phase after atomization [8]. The hydride generation technique was recently examined for all Group 12 metals, and it was found that Hg-, Cd- and Zn-containing molecules are formed in the reduction process, and are released into the gas phase [9-11]. Although these molecules are probably metal dihydrides (HgH_2, CdH_2 and ZnH_2), their identities have not yet been determined with certainty. In another experiment, methyl-mercury chloride (CH_3HgCl) was reduced by $NaBH_4$, and the volatile CH_3HgH molecule was detected in the gas phase by FT-

IR and mass spectrometry [12]. Considering the fact that anaerobic bacteria can reduce aqueous Hg(II) and aqueous ions of Group 14, 15 and 16 elements to form volatile Hg^0, SnH_4, PH_3, AsH_3 and H_2S in the environment [5,6,13,14], a further reduction of Hg^0 by these bacteria may result in the formation of the volatile HgH_2 molecule.

Solid HgH_2, CdH_2 and ZnH_2 have been known for about fifty years, and a few methods have been reported for their synthesis [15-22]. For example, solid HgH_2 has been synthesized from the reaction of HgI_2 with $LiAlH_4$ in ether-THF-petroleum ether solution at –135°C [17-19]. Very recent infrared spectra of these solids suggest that HgH_2 is a covalent molecular solid [23,24], while CdH_2 and ZnH_2 solids probably have hydrogen-bridge bonding [25]. However, these solids are unstable [19,26], and it is probably not possible to vaporize them without decomposition to the constituent elements. In fact, the decomposition of solid HgH_2, CdH_2 and ZnH_2 to metal atoms and molecular hydrogen has been observed at about –125°C, –20°C and +90°C, respectively [16,17]. Aldridge and Downs [27] have reviewed the chemical properties of Group 12 and other main-group hydrides.

High level ab initio theoretical calculations have been performed for the HgH_2, CdH_2 and ZnH_2 molecules, predicting linear H–M–H structures and closed-shell $\widetilde{X}\ ^1\Sigma_g^+$ ground electronic states [28-36]. Equilibrium bond lengths, dissociation energies and vibrational frequencies were also estimated. For a heavy atom like Hg, relativistic effects are significant and should be included in the calculations. For example, it was found that non-relativistic calculations overestimate the Hg–H bond length by more than 0.1 Å [30-33]. Recently, Li et al. [36] performed a very high level ab initio calculation for HgH_2, and predicted the energies for many vibrational levels of HgH_2, HgHD and HgD_2 at $J = 0$ (no rotation) using a variational method. They also calculated that the gas phase reaction, $Hg(g) + H_2(g) \rightarrow HgH_2(g)$, is endoergic by 20.8 kcal/mol. The corresponding reactions for Cd and Zn atoms are also endoergic by 17.0 and 7.6 kcal/mol, respectively [34].

The direct gas phase reactions of Hg, Cd and Zn with H_2 have been studied extensively both by theoretical calculations [37-45] and by various experimental methods [46-57]. It is generally accepted that mercury, cadmium and zinc atoms in their ^1S ground states do not react with molecular hydrogen because large energy barriers exist and the overall reactions (with the production of gaseous MH or MH_2) are endoergic. However, when these atoms are excited to either ^3P or ^1P electronic state, they react efficiently with molecular hydrogen to produce HgH, CdH or ZnH free radicals, i.e., $M^*(g) + H_2(g) \rightarrow MH(g) + H(g)$. Although all

experimental and theoretical work on these reactions [37-57] has supported the idea that an unstable [H–M–H]* excited complex is formed as a reaction intermediate in the production of gaseous MH molecules, little attention has been given to the possibility of forming stable linear H–M–H molecules (M = Hg, Cd, Zn) in the gas phase [39,41].

Many transition metal hydrides including HgH_2, CdH_2 and ZnH_2 have been trapped in solid matrices at temperatures below 12 K, and studied by infrared absorption spectroscopy [58]. Excited Hg, Cd and Zn atoms reacted with molecular hydrogen in solid argon, neon, or hydrogen matrices, and metal dihydrides were formed [23-25,34,58-61]. Low-resolution infrared spectra of these molecules trapped in solid matrices were recorded and vibrational frequencies were obtained. There was no observation of gaseous HgH_2, CdH_2 and ZnH_2 molecules prior to the present work.

In this chapter, the discovery of gaseous ZnH_2, ZnD_2, HgH_2 and HgD_2 molecules, and detailed analyses of their high-resolution infrared emission spectra are reported. The molecules were generated from direct gas phase reactions of excited Zn and Hg atoms with molecular hydrogen or deuterium in a discharge-furnace cell. Gaseous CdH_2 and CdD_2 were also discovered in our laboratory, and their infrared emission spectra were analyzed by Yu et al. [62]. Since many properties of gaseous HgH_2, CdH_2 and ZnH_2 molecules are similar, some of the results for CdH_2 and CdD_2 are cited here for comparison. The results presented in this chapter have been previously published in Refs. [63-66].

5.2 Experiments and Results

The discharge-furnace emission source described in Chapter 1 was used to generate the ZnH_2, ZnD_2, HgH_2 and HgD_2 molecules. Emission lines of ZnH_2 and ZnD_2 were observed in the same spectra recorded for ZnH and ZnD molecules, respectively, so the experimental conditions are exactly the same as those described in Chapter 3. The instrumental resolution was 0.01 cm^{-1}, and the signal-to-noise ratios for the strongest emission lines of ZnH_2 and ZnD_2 were about 50 and 20, respectively.

For the HgH_2 and HgD_2 experiments, about 100 grams of liquid Hg was placed inside a small zirconia boat at the central part of an alumina tube, and pure hydrogen or deuterium (0.7 Torr) flowed slowly through the tube at room temperature. A dc discharge (3 kV / 333 mA) was created between the electrodes, and the resulting emission was focused onto the entrance aperture of the spectrometer using a BaF_2 lens. The infrared emission spectrum of HgH_2 was recorded using a KBr beamsplitter and an InSb detector cooled by liquid nitrogen. The spectral range was limited to 1750–2200 cm^{-1} by the detector response and a 2200 cm^{-1} long-wave pass filter. The instrumental resolution was set to 0.01 cm^{-1}, and 100 scans were co-added during 90 minutes of recording. The spectrum of HgD_2 was recorded using the same beamsplitter and a liquid-nitrogen-cooled MCT detector. The spectral range for HgD_2 was 1200–2200 cm^{-1}, set by the transmission of the 2200 cm^{-1} long-wave pass filter. The instrumental resolution was 0.01 cm^{-1}, and 400 scans were co-added during 6 hours of recording. The signal-to-noise ratios for the strongest emission lines of HgH_2 and HgD_2 were about 100 and 40, respectively.

The absolute wavenumber calibration for ZnH_2 and ZnD_2 spectra was based on carbon monoxide impurity [67] and common atomic emission lines, as described in Chapter 3. The absolute accuracy of calibrated line positions for ZnH_2 and ZnD_2 is about 0.001 cm^{-1}. Emission lines of impurity CO also appeared in both HgH_2 and HgD_2 spectra, and these spectra were calibrated independently. The calibrated line positions of HgH_2 and HgD_2 have an absolute accuracy of about 0.0005 cm^{-1}.

The strongest molecular emission lines were assigned to the antisymmetric stretching fundamental bands, $001(\Sigma_u^+) \rightarrow 000(\Sigma_g^+)$, of ZnH_2, ZnD_2, HgH_2 and HgD_2 for the following reasons: *a*) the observed ν_3 band origins in the spectra match the values obtained from matrix isolation experiments [34,60] if matrix shifts are taken into account; *b*) the rotational

constants determined from the spectra match the values predicted by ab initio theoretical calculations [29,34]; *c*) the adjacent rotational lines for MH_2 and MD_2 have alternating 3:1 and 1:2 intensity ratios, respectively, due to the *ortho-para* nuclear spin statistical weights associated with hydrogen and deuterium nuclei [68]. Overviews of ZnH_2 and HgD_2 spectra are shown in Figures 5.1 and 5.2, respectively. Expanded views of HgH_2 and HgD_2 spectra in Figures 5.3 and 5.4, respectively, show the 3:1 and 1:2 intensity alternations in adjacent rotational lines.

Zinc has five stable isotopes, three of which are relatively abundant: ^{64}Zn (48.6%), ^{66}Zn (27.9%), ^{67}Zn (4.1%), ^{68}Zn (18.8%), and ^{70}Zn (0.6%). The terrestrial abundances for the seven stable isotopes of mercury are: ^{204}Hg (6.9%), ^{202}Hg (29.8%), ^{201}Hg (13.2%), ^{200}Hg (23.1%), ^{199}Hg (16.9%), ^{198}Hg (10.0%) and ^{196}Hg (0.1%). Lines from several isotopes of Zn and Hg (all except ^{70}Zn and ^{196}Hg) were observed in the spectra, and their intensity ratios match the terrestrial abundances of those isotopes. The isotope splitting in rotational lines of HgH_2 and ZnD_2 are illustrated in Figures 5.5 and 5.6, respectively.

Five vibration-rotation bands were observed for $^{202}HgH_2$, $^{200}HgH_2$, $^{202}HgD_2$ and $^{200}HgD_2$, i.e., the $001(\Sigma_u^+)\rightarrow000(\Sigma_g^+)$ fundamental band and the following hot bands:

$$002(\Sigma_g^+)\rightarrow001(\Sigma_u^+), \qquad 01^11(\Pi_g)\rightarrow01^10(\Pi_u),$$
$$003(\Sigma_u^+)\rightarrow002(\Sigma_g^+), \qquad 101(\Sigma_u^+)\rightarrow100(\Sigma_g^+).$$

Fewer hot bands were detectable for the ^{201}Hg, ^{199}Hg, ^{198}Hg and ^{204}Hg isotopes because of their lower abundances. The ν_3 fundamental and the following hot bands were observed for both $^{64}ZnH_2$ and $^{64}ZnD_2$:

$$002(\Sigma_g^+)\rightarrow001(\Sigma_u^+), \qquad 01^11(\Pi_g)\rightarrow01^10(\Pi_u),$$
$$003(\Sigma_u^+)\rightarrow002(\Sigma_g^+), \qquad 101(\Sigma_u^+)\rightarrow100(\Sigma_g^+),$$
$$02^21(\Delta_u)\rightarrow02^20(\Delta_g), \qquad 02^01(\Sigma_u^+)\rightarrow02^00(\Sigma_g^+).$$

In addition, the $004(\Sigma_g^+)\rightarrow003(\Sigma_u^+)$ and $200(\Sigma_g^+)\rightarrow001(\Sigma_u^+)$ bands of $^{64}ZnH_2$, and the $01^12(\Pi_u)\rightarrow01^11(\Pi_g)$ band of $^{64}ZnD_2$ were found. Fewer hot bands were detectable for the ^{66}Zn and ^{68}Zn isotopes because of their lower abundances. Lines from the ^{67}Zn isotope were too weak to be observed, except for the $001(\Sigma_u^+)\rightarrow000(\Sigma_g^+)$ fundamental band of $^{67}ZnH_2$.

Line positions of the ν_3 fundamental bands of $^{64}ZnH_2$, $^{66}ZnH_2$, $^{64}ZnD_2$, $^{66}ZnD_2$, $^{202}HgH_2$, $^{200}HgH_2$, $^{202}HgD_2$ and $^{200}HgD_2$ are listed in Tables A5 to A12 of the Appendix, respectively.

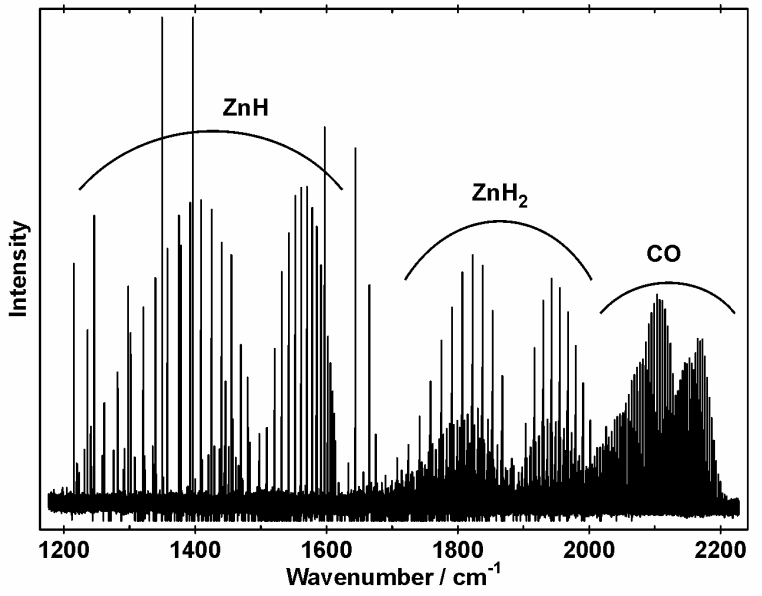

Figure 5.1. An overview of ZnH_2 spectrum after baseline correction.

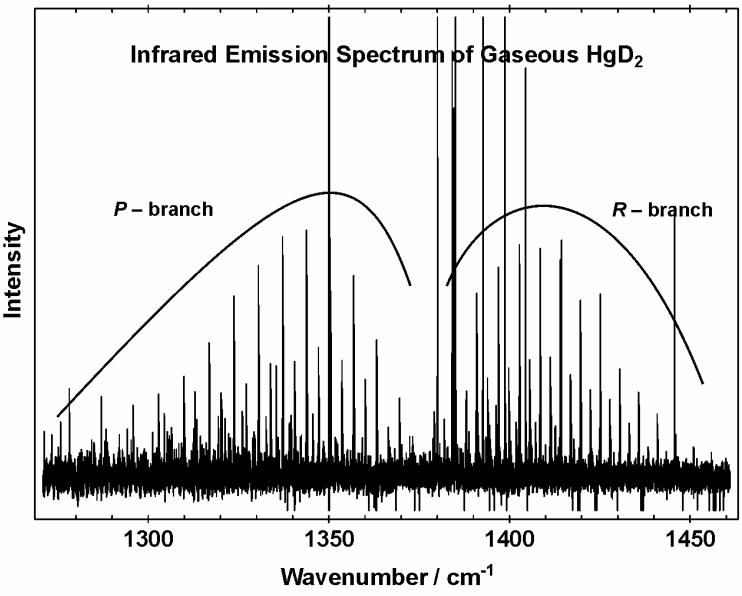

Figure 5.2. An overview of HgD_2 spectrum after baseline correction.

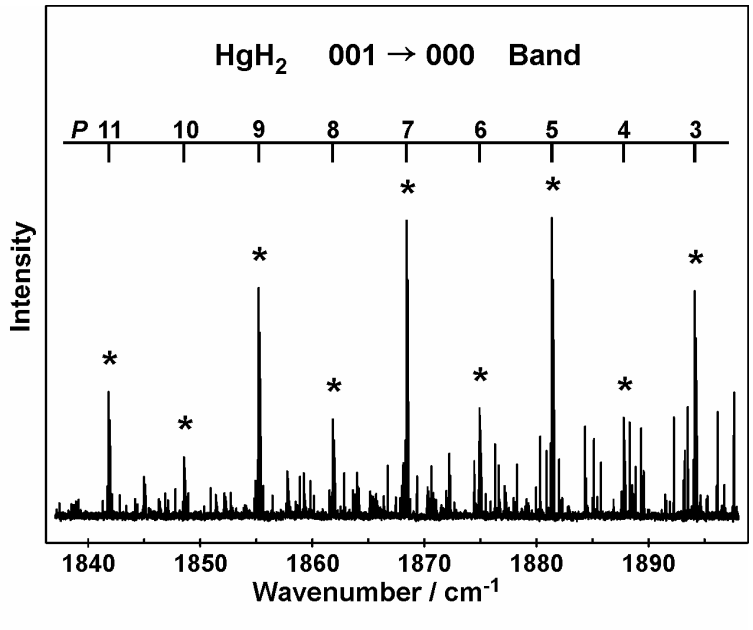

Figure 5.3. An expanded view of HgH_2 spectrum showing the 3:1 intensity alternation.

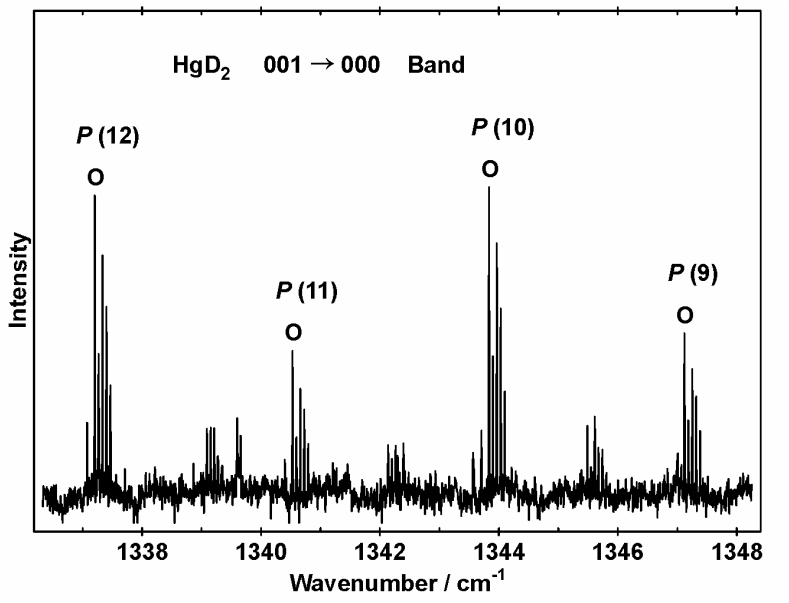

Figure 5.4. An expanded view of HgD_2 spectrum showing the 1:2 intensity alternation.

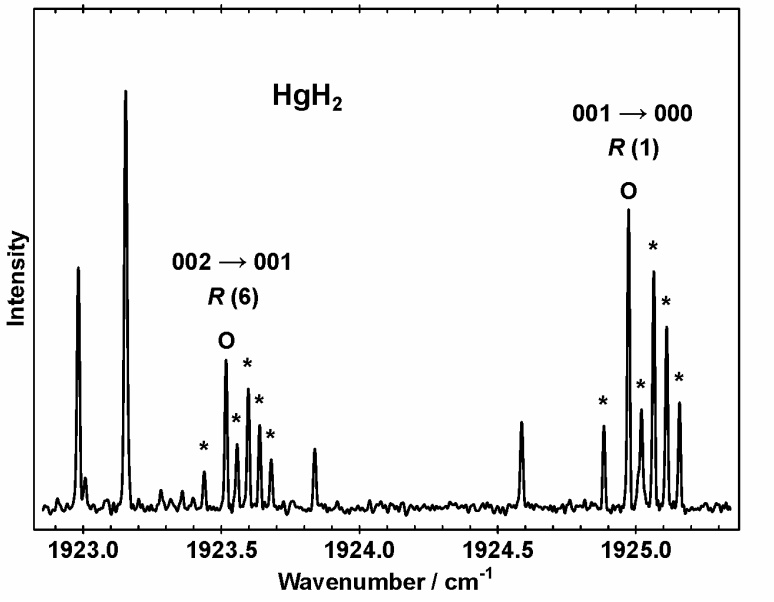

Figure 5.5. An expanded view of HgH_2 spectrum showing the isotope splitting.

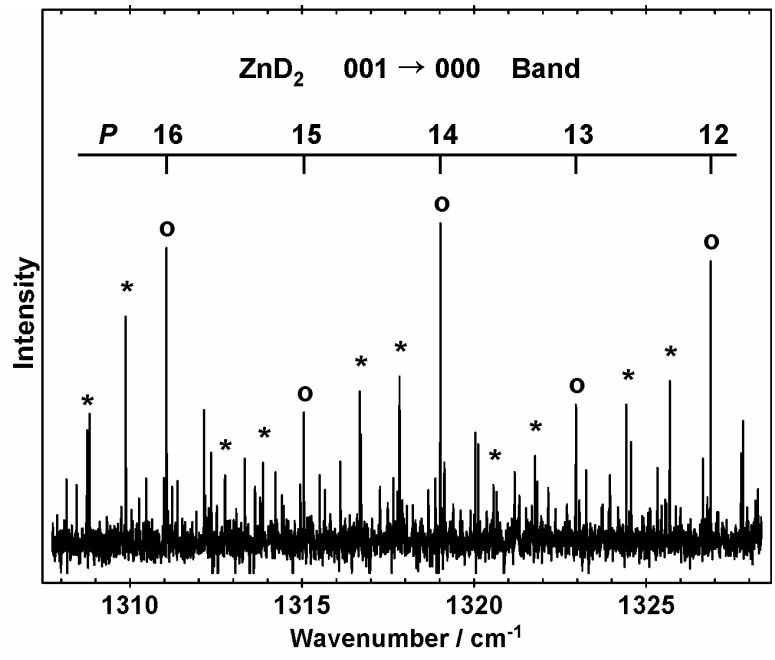

Figure 5.6. An expanded view of ZnD_2 spectrum showing the isotope splitting and the 1:2 intensity alternation.

5.3 Analyses of ZnH_2 and ZnD_2 Spectra

5.3.1 Vibration-rotation bands of ZnH_2 and ZnD_2

The absolute rotational assignments of the $001(\Sigma_u^+)\rightarrow 000(\Sigma_g^+)$ fundamental bands of ZnH_2 and ZnD_2 were not difficult to find because the low J lines near the band origins were observed. The intensity alternations in adjacent rotational lines and small local perturbations at high J's of the $001(\Sigma_u^+)$ state of both ZnH_2 and ZnD_2 further confirmed the absolute J assignments. The local perturbations observed in the 001 level are caused by the nearby 030 level, because the frequency of the antisymmetric stretching mode is almost equal to three times the frequency of the bending mode, i.e., $\nu_3 \approx 3\nu_2$ [34]. Rotational lines of the $001(\Sigma_u^+)\rightarrow 000(\Sigma_g^+)$ fundamental bands were fitted using the energy expression in Eq. (4.3), and the ground state vibrational energies (G_{000}) were set to zero for both ZnH_2 and ZnD_2. For the perturbed rotational levels in the $001(\Sigma_u^+)$ state, i.e., $J' > 15$ for ZnH_2 and $J' > 20$ for ZnD_2, the total energies were fitted to individual term values. As a result, accurate rotational constants were obtained for the 000 ground states of ZnH_2 and ZnD_2, while the rotational constants of the 001 states can reproduce the data only for the lower J's.

The rotational assignment of the $002(\Sigma_g^+)\rightarrow 001(\Sigma_u^+)$, $003(\Sigma_u^+)\rightarrow 002(\Sigma_g^+)$ and $004(\Sigma_g^+)\rightarrow 003(\Sigma_u^+)$ hot bands were obtained consecutively using lower state combination differences (see Chapter 2). The $002(\Sigma_g^+)$ states of both ZnH_2 and ZnD_2 were globally perturbed by the nearby $200(\Sigma_g^+)$ states. Ab initio calculations of Greene et al. [34] have predicted that the ν_1 and ν_3 frequencies are nearly equal. Although the 001 and 100 levels have opposite g/u symmetries and do not interact with one another, the 002 and 200 levels both have Σ_g^+ symmetry, and are hence strongly coupled by Fermi resonance. Due to the strong mixing of the 002 and 200 levels in ZnH_2, rotational lines of the $200(\Sigma_g^+)\rightarrow 001(\Sigma_u^+)$ combination band of ZnH_2 appeared in the spectrum, and were easily assigned using lower state combination differences. The energy expression in Eq. (4.3) with $\ell = 0$ was used for all these vibrational levels, and effective spectroscopic constants were determined for all the observed isotopologues. Rotational assignments of the $101(\Sigma_u^+)\rightarrow 100(\Sigma_g^+)$ hot bands of ZnH_2 and ZnD_2 were based on intensity alternations in adjacent rotational lines, and no perturbations were observed for these bands. The vibrational energy of the $100(\Sigma_g^+)$ state was set to zero in the fit, since only the difference between the vibrational energies of the $101(\Sigma_u^+)$ and $100(\Sigma_g^+)$ states can be determined using these data. Complete lists of the

observed line positions and the outputs of the least-squares fitting program have been published in the supplementary tables of Ref. [65]. Effective spectroscopic constants for several vibrational states of $^{64}ZnH_2$, $^{66}ZnH_2$, $^{64}ZnD_2$ and $^{66}ZnD_2$ are presented in Tables 5.1 to 5.4, respectively. The effect of Fermi resonance was neglected in the determination of the constants listed in Tables 5.1 to 5.4, but the effective constants reported in these tables can reproduce the data within experimental uncertainty.

The second strongest bands in both ZnH_2 and ZnD_2 spectra had large ℓ-type doubling, and were assigned as the $01^11(\Pi_g)\rightarrow01^10(\Pi_u)$ hot bands. The absolute J assignments for these bands were obtained based on the intensity alternations and the fact that e and f parity components must have the same band origins. Small local perturbations were observed in the high J's of the $01^11(\Pi_g)$ state for both ZnH_2 and ZnD_2. These perturbations are caused by the nearby 040 vibrational level, and they further confirm the absolute J assignments. Rotational lines of the $01^11(\Pi_g)\rightarrow01^10(\Pi_u)$ bands were fitted using the energy expression in Eq. (4.3) with $\ell = 1$. For the perturbed rotational levels in the $01^11(\Pi_g)$ state, the total energies were fitted to individual term values. The rotational assignment of the $01^12(\Pi_u)\rightarrow01^11(\Pi_g)$ hot band of ZnD_2 was obtained using lower state combination differences. Rotational constants and the ℓ-type doubling constants of the 01^10, 01^11 and 01^12 states are listed in Tables 5.1 to 5.4 for $^{64}ZnH_2$, $^{66}ZnH_2$, $^{64}ZnD_2$ and $^{66}ZnD_2$, respectively.

Table 5.1. Effective spectroscopic constants (in cm^{-1}) for the Σ and Π states of $^{64}ZnH_2$.

	Vibrational levels			
$^{64}ZnH_2$	000 (Σ_g^+)[a]	001 (Σ_u^+)[b]	002 (Σ_g^+)[c]	003 (Σ_u^+)
G	0.0	1889.43310(24)	3772.29298(33)	5605.28350(56)
B	3.5482143(86)	3.5065650(83)	3.4578091(65)	3.4195915(88)
$10^5\ D$	4.9225(25)	4.9001(23)	4.7293(10)	4.8433(19)
$10^{10}\ H$	4.27(22)	…	…	…

$^{64}ZnH_2$	010 (Π_u)[d]	011 (Π_g)
G	ν_2	1876.96690(24) + ν_2
B	3.542900(10)	3.501569(11)
$10^5\ D$	4.9850(18)	4.9792(21)
$10^2\ q$	–5.9464(21)	–5.8509(21)
$10^6\ q_D$	2.920(35)	2.784(41)

$^{64}ZnH_2$	200 (Σ_g^+)[c]	004 (Σ_g^+)	100 (Σ_g^+)[d]	101 (Σ_u^+)
G	3712.96942(60)	7422.50030(75)	ν_1	1827.65621(46) + ν_1
B	3.451241(15)	3.372528(12)	3.496356(27)	3.454273(27)
$10^5\ D$	5.0353(57)	4.6570(31)	4.8994(77)	4.9321(77)

[a] The numbers in parentheses are 1σ uncertainties in the last quoted digits.

[b] The effective constants of the 001 state can accurately reproduce the $J = 0$ to 15 rotational energy levels (see the text).

[c] The effect of Fermi resonance between the 002 and 200 states was neglected in determination of these constants (see the text).

[d] The wavenumbers of ν_1 and ν_2 cannot be determined from the data. The neon matrix value for ν_2 is 632.5 cm^{-1}, and ν_1 is almost equal to ν_3.

Table 5.2. Effective spectroscopic constants (in cm^{-1}) for the Σ and Π states of $^{66}ZnH_2$.

	Vibrational levels			
$^{66}ZnH_2$	000 (Σ_g^+)[a]	001 (Σ_u^+)[b]	002 (Σ_g^+)[c]	003 (Σ_u^+)
G	0.0	1888.59587(24)	3771.26231(35)	5603.16104(62)
B	3.5482232(90)	3.5066355(89)	3.4576360(69)	3.4196843(96)
$10^5\ D$	4.9231(25)	4.9008(25)	4.7239(11)	4.8417(20)
$10^{10}\ H$	4.37(22)	…	…	…

$^{66}ZnH_2$	010 (Π_u)[d]	011 (Π_g)
G	ν_2	1876.15119(25) + ν_2
B	3.542870(11)	3.501604(12)
$10^5\ D$	4.9823(19)	4.9779(24)
$10^2\ q$	–5.9465(22)	–5.8497(23)
$10^6\ q_D$	2.825(39)	2.640(45)

$^{66}ZnH_2$	200 (Σ_g^+)[c]	100 (Σ_g^+)[d]	101 (Σ_u^+)
G	3712.37191(57)	ν_1	1826.83307(82) + ν_1
B	3.451495(15)	3.496339(48)	3.454325(51)
$10^5\ D$	5.0260(57)	4.899(13)	4.941(14)

[a] The numbers in parentheses are 1σ uncertainties in the last quoted digits.

[b] The effective constants of the 001 state can accurately reproduce the J = 0 to 15 rotational energy levels (see the text).

[c] The effect of Fermi resonance between the 002 and 200 states was neglected in determination of these constants (see the text).

[d] The wavenumbers of ν_1 and ν_2 cannot be determined from the data. The neon matrix value for ν_2 is 632.5 cm^{-1}, and ν_1 is almost equal to ν_3.

Table 5.3. Effective spectroscopic constants (in cm^{-1}) for the Σ and Π states of $^{64}ZnD_2$.

	Vibrational levels			
$^{64}ZnD_2$	000 (Σ_g^+)[a]	001 (Σ_u^+)[b]	002 (Σ_g^+)[c]	003 (Σ_u^+)
G	0.0	1371.63134(22)	2732.32243(32)	4076.86517(57)
B	1.7834239(67)	1.7679889(64)	1.7521750(56)	1.7366911(64)
$10^5\ D$	1.2271(11)	1.22073(93)	1.21509(56)	1.21586(68)
$10^{10}\ H$	0.452(54)	…	…	…
$^{64}ZnD_2$	010 (Π_u)[d]	011 (Π_g)	012 (Π_u)	
G	ν_2	1364.99238(19) + ν_2	2719.38019(44) + ν_2	
B	1.7817330(48)	1.7663714(50)	1.7505663(57)	
$10^5\ D$	1.23746(38)	1.23401(48)	1.22974(60)	
$10^2\ q$	–2.0744(10)	–2.0538(10)	–2.0353(10)	
$10^6\ q_D$	0.491(8)	0.466(9)	0.467(10)	
$^{64}ZnD_2$	100 (Σ_g^+)[d]	101 (Σ_u^+)		
G	ν_1	1340.31010(52) + ν_1		
B	1.765108(27)	1.749586(28)		
$10^5\ D$	1.2215(52)	1.2278(55)		

[a] The numbers in parentheses are 1σ uncertainties in the last quoted digits.

[b] The effective constants of the 001 state can accurately reproduce the $J = 0$ to 20 rotational energy levels (see the text).

[c] The effect of Fermi resonance between the 002 and 200 states was neglected in determination of these constants (see the text).

[d] The wavenumbers of ν_1 and ν_2 cannot be determined from the data. The neon matrix value for ν_2 is 456.4 cm^{-1}, and ν_1 is about 30 cm^{-1} smaller than ν_3.

Table 5.4. Effective spectroscopic constants (in cm^{-1}) for the Σ and Π states of $^{66}ZnD_2$.

	Vibrational levels			
$^{66}ZnD_2$	000 (Σ_g^+)[a]	001 (Σ_u^+)[b]	002 (Σ_g^+)[c]	003 (Σ_u^+)
G	0.0	1370.43744(31)	2730.14651(39)	4073.56984(63)
B	1.7834268(77)	1.7680319(70)	1.7522234(61)	1.7367913(76)
$10^5\ D$	1.2276(13)	1.2209(10)	1.21534(61)	1.21548(97)
$10^{10}\ H$	0.454(70)	…	…	…

$^{66}ZnD_2$	010 (Π_u)[d]	011 (Π_g)	012 (Π_u)
G	ν_2	1363.81977(22) + ν_2	2717.26479(52) + ν_2
B	1.7817418(78)	1.7664250(82)	1.7506271(90)
$10^5\ D$	1.2411(9)	1.2381(10)	1.2355(12)
$10^2\ q$	–2.0764(16)	–2.0558(16)	–2.0362(17)
$10^6\ q_D$	0.493(18)	0.476(20)	0.441(22)

$^{66}ZnD_2$	100 (Σ_g^+)[d]	101 (Σ_u^+)
G	ν_1	1339.13278(74) + ν_1
B	1.765154(36)	1.749652(38)
$10^5\ D$	1.2284(71)	1.2318(78)

[a] The numbers in parentheses are 1σ uncertainties in the last quoted digits.

[b] The effective constants of the 001 state can accurately reproduce the $J = 0$ to 20 rotational energy levels (see the text).

[c] The effect of Fermi resonance between the 002 and 200 states was neglected in determination of these constants (see the text).

[d] The wavenumbers of ν_1 and ν_2 cannot be determined from the data. The neon matrix value [25] for ν_2 is 456.4 cm^{-1}, and ν_1 is about 30 cm^{-1} smaller than ν_3.

5.3.2 Rotational ℓ-type resonance in ZnH_2 and ZnD_2

Similar to the BeH_2, BeD_2 and MgH_2 bands, rotational ℓ-type resonance was observed in the $02^21(\Delta_u)\rightarrow02^20(\Delta_g)$ and $02^01(\Sigma_u^+)\rightarrow02^00(\Sigma_g^+)$ bands of both $^{64}ZnH_2$ and $^{64}ZnD_2$. The energy level expressions in Eqs. (4.5) to (4.8) were used to fit these bands, and the relative assignments of the $\Sigma^+(e)$ and $\Delta(e)$ levels were based on the assumption that $[g_{22} - B]$ is negative (see Chapter 4). The constants obtained from the ℓ-type resonance fits of $^{64}ZnH_2$ and $^{64}ZnD_2$ are listed in Tables 5.5 and 5.6, respectively. For both $^{64}ZnH_2$ and $^{64}ZnD_2$, switching the $\Sigma^+(e)$ and $\Delta(e)$ assignments results in a small increase (about 10%) in the standard deviation of the fit. The relative assignments of the $\Sigma^+(e)$ and $\Delta(e)$ levels were confirmed very recently by the ab initio calculations of Koput [69]. The theoretical g_{22} constants of $^{64}ZnH_2$ and $^{64}ZnD_2$ predicted by Koput [69] differ from the experimental values (Tables 5.5 and 5.6) by less than 0.03 cm^{-1}.

Lines from the minor isotopologues $^{66}ZnH_2$ and $^{66}ZnD_2$ were weak, and only the *f* parity component of the Δ states could be assigned with certainty. Lines from the *f* parity component of the $02^21(\Delta_u)\rightarrow02^20(\Delta_g)$ bands of $^{66}ZnH_2$ and $^{66}ZnD_2$ were fitted using Eq. (4.6), and the corresponding constants (G_Δ, B_Δ and D_Δ) are listed in Tables 5.5 and 5.6.

Table 5.5. Spectroscopic constants (in cm^{-1}) for the rotational ℓ-type resonance in ZnH_2; all uncertainties are 1σ.

	$^{64}ZnH_2$		$^{66}ZnH_2$	
	Vibrational levels		Vibrational levels	
Const.	020 [a]	021	020 [a]	021
G_Δ	a	1864.5521(5) + a	a'	1863.7596(8) + a'
g_{22}	1.6452(70)	1.6038(70)	…	…
B_Δ	3.537753(24)	3.496759(25)	3.537689(27)	3.496719(28)
$10^5\ D_\Delta$	5.0832(41)	5.0862(44)	5.0787(54)	5.0686(57)
B_Σ	3.539086(51)	3.498055(51)	…	…
$10^5\ D_\Sigma$	5.099(12)	5.095(11)	…	…
$10^2\ q$	–5.9735(67)	–5.8764(66)	…	…
$10^6\ q_D$	2.95(11)	2.81(10)	…	…

[a] The absolute vibrational energy of the 020 level cannot be determined from the data; $a \approx 2\nu_2$.

Table 5.6. Spectroscopic constants (in cm^{-1}) for the rotational ℓ-type resonance in ZnD_2; all uncertainties are 1σ.

	$^{64}ZnD_2$		$^{66}ZnD_2$	
	Vibrational levels		Vibrational levels	
Const.	020 [a]	021	020 [a]	021
G_Δ	b	1358.3792(4) + b	b'	1357.2253(7) + b'
g_{22}	0.9075(45)	0.8918(45)	…	…
B_Δ	1.780174(17)	1.764880(18)	1.779766(24)	1.764510(25)
$10^5\ D_\Delta$	1.2625(19)	1.2591(20)	1.1844(29)	1.1697(30)
B_Σ	1.780388(27)	1.765095(28)	…	…
$10^5\ D_\Sigma$	1.2513(32)	1.2478(32)	…	…
$10^2\ q$	–2.0767(26)	–2.0559(26)	…	…
$10^6\ q_D$	0.446(23)	0.425(22)	…	…

[a] The absolute vibrational energy of the 020 level cannot be determined from the data; $b \approx 2\nu_2$.

5.3.3 Local perturbations in ZnH_2 and ZnD_2

For both $^{64}ZnH_2$ and $^{64}ZnD_2$ molecules, high rotational levels of the 001 (Σ_u^+) state are perturbed by the nearby 030 vibrational level, which has $03^10(\Pi_u)$ and $03^30(\Phi_u)$ states. Rotational levels of the 001(Σ_u^+) state of ZnH_2 with $J \leq 17$ are shifted towards higher energies, whereas the $J \geq 18$ levels are shifted towards lower energies. Similarly, the rotational levels of the 001(Σ_u^+) state of ZnD_2 with $J \leq 22$ were shifted up and the $J \geq 23$ levels were shifted down. The magnitudes of these perturbations were small, and the largest energy shifts were about 0.04 cm^{-1}, observed right at the crossing point ($J = 17$ for ZnH_2 and $J = 22$ for ZnD_2). The perturbation pattern observed in both ZnH_2 and ZnD_2 clearly indicates that the perturbing state has a larger effective $B_{[v]}$ value. The effective $B_{[v]}$ values of the $03^10(\Pi_u)$ and $03^30(\Phi_u)$ states were estimated using the $B_{[v]}$ values of the 000, 01^10, 02^00 and 02^20 states. The $03^10(\Pi_u)$ and $03^30(\Phi_u)$ states have *e* and *f* parity components, but only the *e* parity levels can interact with the 001(Σ_u^+) rotational levels. Due to the large rotational ℓ-type doubling in the $03^10(\Pi_u)$ state, the effective $B_{[v]}$ value of its *e* parity component becomes considerably smaller than that of the 001(Σ_u^+) state. Therefore, in both ZnH_2 and ZnD_2, the $03^30(\Phi_u)$ state is responsible for the observed perturbations in the 001(Σ_u^+) state. A 3×3 Hamiltonian matrix was constructed for the *e* parity levels of 001(Σ_u^+), $03^30(\Phi_u)$ and $03^10(\Pi_u)$ states. The $03^10(\Pi_u)$ state was included in the matrix because it interacts with the $03^30(\Phi_u)$ state through rotational ℓ-type resonance [70], and thus has an indirect effect on the state of interest (001, Σ_u^+). The vibrational energy difference between the 03^10 and 03^30 states is equal to $8g_{22}$ based on Eq. (4.2). Maki and Lide [70] have derived the Hamiltonian matrix for rotational ℓ-type resonance between Π and Φ states. After parity transformation and including the Σ_u^+ (*e*) state, the following 3×3 Hamiltonian matrix was obtained for the *e* levels:

$$\mathbf{H} = \begin{pmatrix} E_\Sigma^0(001) & -W_{03} & 0 \\ -W_{03} & E_\Phi^0 & W_{31} \\ 0 & W_{31} & E_\Pi^0 + W_{11} \end{pmatrix}. \tag{5.1}$$

The matrix element connecting the Σ_u^+ and Π_u states was fixed to zero because the perturbations in the 001(Σ_u^+) state are caused by the Φ_u state. The following expressions, in which $x = J(J+1)$, were used for the above matrix elements:

$$E_\Sigma^0(001) = G_{001} + B_{001}\,x - D_{001}\,x^2 + H_{001}\,x^3 \tag{5.2}$$

$$E_\Phi^0 = G_\Phi + B_\Phi(x-9) - D_\Phi(x-9)^2 \tag{5.3}$$

$$E^0_{\Pi} = (G_{\Phi} - 8\,g_{22}) + B_{\Pi}(x-1) - D_{\Pi}(x-1)^2 \tag{5.4}$$

$$W_{11} = qx + q_{\rm D}x^2 \tag{5.5}$$

$$W_{31} = \frac{\sqrt{3}}{2}(q + q_{\rm D}x)\left[(x-2)(x-6)\right]^{1/2} \tag{5.6}$$

$$W_{03} = K_{03}\left[x(x-2)(x-6)\right]^{1/2}. \tag{5.7}$$

Note that the rotational energy expressions used for the Φ_u (ℓ = 3) and Π_u (ℓ = 1) states in Eqs. (5.3) and (5.4) are power series in [$J(J+1) - \ell^2$]. The J-dependence of W_{03}, which connects the Σ and Φ states, was determined by applying the $\left(\hat{J}^+\right)^3$ operator (in the molecular frame) [71] to the Φ state basis function. The purpose of this perturbation analysis was to obtain the unperturbed constants for the $001(\Sigma^+_u)$ state, and to estimate the vibrational energy of the $03^30(\Phi_u)$ state.

All rotational lines of the 001→000, 002→001 and 200→001 bands were fitted using the Hamiltonian matrix in Eq. (5.1) for the 001 levels, while the constants of the 000, 002 and 200 states were fixed to the values reported in Tables 5.1 to 5.4. Rotational constants (B, D) and the ℓ-type doubling constants (q, $q_{\rm D}$) of the $03^10(\Pi_u)$ and $03^30(\Phi_u)$ states were fixed to the values estimated by extrapolating the 000, 01^10, 02^00 and 02^20 constants. The following expression was used to estimate the $B_{[v]}$ values as accurately as possible [70]:

$$\begin{aligned} B_{[v]} = {} & B_e - \alpha_1\left(v_1 + \tfrac{1}{2}\right) - \alpha_2\left(v_2 + 1\right) - \alpha_3\left(v_3 + \tfrac{1}{2}\right) \\ & + \gamma_{11}\left(v_1 + \tfrac{1}{2}\right)^2 + \gamma_{22}\left(v_2 + 1\right)^2 + \gamma_{33}\left(v_3 + \tfrac{1}{2}\right)^2 + \gamma_{\ell\ell}\ell^2 \\ & + \gamma_{12}\left(v_1 + \tfrac{1}{2}\right)\left(v_2 + 1\right) + \gamma_{13}\left(v_1 + \tfrac{1}{2}\right)\left(v_3 + \tfrac{1}{2}\right) + \gamma_{23}\left(v_2 + 1\right)\left(v_3 + \tfrac{1}{2}\right) \end{aligned} \tag{5.8}$$

The above expression for the $B_{[v]}$ constants is preferred to Eq. (4.4), as it includes higher-order terms. Note that the γ_{ij} constants in Eq. (5.8) account for the second-order vibrational dependence of the rotational constant $B_{[v]}$, and are totally different from the $\gamma_{l,m}$ coefficients introduced in Chapters 2 and 3. The constants γ_{22}, $\gamma_{\ell\ell}$, and $[-\alpha_2 + \gamma_{12} + \gamma_{23}]$ were obtained using the 000, 01^10, 02^00 and 02^20 $B_{[v]}$ values, and were used to calculate the $B_{[v]}$ constants of the 03^30 and 03^10 states of $^{64}ZnH_2$ and $^{64}ZnD_2$. A quadratic expression analogous to Eq. (5.8) was used to calculate the $D_{[v]}$ constants. For the minor isotopologues $^{66}ZnH_2$ and $^{66}ZnD_2$, the γ_{22} and $\gamma_{\ell\ell}$ constants were not available and the corresponding constants of $^{64}ZnH_2$ and $^{64}ZnD_2$ were used instead. The ℓ-type doubling constants $q_{[v]}$ and $q_{D,[v]}$ were estimated using the corresponding constants of the 010 and 020 levels, and by assuming a linear vibrational dependence similar to that of Eq. (4.4). The vibrational constants g_{22} of ZnH_2 and ZnD_2 were also fixed to the values reported in Tables 5.5 and 5.6. The least-

squares fitting resulted in determination of G_Φ (vibrational energy of the 03^30 state), K_{03} (off-diagonal matrix element between Σ and Φ states), and the unperturbed constants of the $001(\Sigma_u^+)$ state for $^{64}ZnH_2$, $^{66}ZnH_2$, $^{64}ZnD_2$ and $^{66}ZnD_2$ molecules (Table 5.7). The constants of Table 5.7 differ slightly from those reported in Tables 5.1 to 5.4 for the $001(\Sigma_u^+)$ states. For example, since all the rotational lines (including high J's) were included in the perturbation analysis, the third order H_{001} constants were also required for both $^{64}ZnH_2$ and $^{64}ZnD_2$. Overall, the constants of Table 5.7 are more reliable for the $001(\Sigma_u^+)$ states, because they reproduce all the observed energy levels within their experimental uncertainties of about 0.001 cm^{-1}.

The Σ-Φ interaction constants (K_{03}) were determined to be $4.214(16)\times10^{-5}$ cm^{-1} and $0.794(16)\times10^{-5}$ cm^{-1} for $^{64}ZnH_2$ and $^{64}ZnD_2$, respectively. The off-diagonal matrix element W_{03} is zero for $J < 3$, and it increases rapidly with J. At the highest observed rotational levels of $^{64}ZnH_2$ ($J = 28$) and $^{64}ZnD_2$ ($J = 35$), W_{03} is about 0.97 cm^{-1} and 0.35 cm^{-1}, respectively. Although the vibrational energies of the 03^30 states (G_Φ) have statistical uncertainties of about 0.01 cm^{-1} in Table 5.7, an absolute accuracy of about 0.5 cm^{-1} is estimated for these energies, because several constants in the fits were fixed to the extrapolated values.

Table 5.7. Unperturbed constants (in cm^{-1}) for the 001(Σ_u^+) states of $^{64}ZnH_2$, $^{66}ZnH_2$, $^{64}ZnD_2$ and $^{66}ZnD_2$; all uncertainties are 1σ.

Constant [a]	$^{64}ZnH_2$	$^{66}ZnH_2$	$^{64}ZnD_2$	$^{66}ZnD_2$
G_{001}	1889.4326(1)	1888.5954(2)	1371.6310(2)	1370.4371(2)
B_{001}	3.506592(2)	3.506661(3)	1.767999(2)	1.768042(2)
$10^5\ D_{001}$	4.9252(9)	4.9255(11)	1.2257(4)	1.2258(5)
$10^{10}\ H_{001}$	4.46(9)	4.45(11)	0.453(23)	0.423(32)
$10^5\ K_{03}$ (Σ,Φ)	4.214(16)	4.196(16)	0.794(16)	0.814(23)
G_Φ	1898.1196(85)	1897.2938(86)	1374.7226(63)	1373.515(11)
g_{22}	1.6452 [b]	1.6452 [b]	0.9075 [b]	0.9075 [b]
B_Φ	3.53277	3.53266	1.77875	1.77877
$10^5\ D_\Phi$	5.217	5.208	1.302	1.312
B_Π	3.53544	3.53533	1.77917	1.77920
$10^5\ D_\Pi$	5.249	5.240	1.280	1.290
$10^2\ q$	–6.001	–6.001	–2.079	–2.081
$10^6\ q_D$	2.98	2.88	0.401	0.403

[a] The constants reported in this table can reproduce all the observed rotational energy levels of the 001 (Σ_u^+) states within their experimental uncertainties. The vibrational energies G_{001} and G_Φ are relative to the ground state vibrational energy (G_{000}).

[b] The constants B, D, q, q_D and g_{22} for the perturbing states (03^10 and 03^30) were fixed to the extrapolated values (see the text).

5.3.4 Fermi resonance in ZnH_2 and ZnD_2

Ab initio calculations at the MP2, CCSD(T) and DFT(B3LYP) levels of theory [25,34] predict that the vibrational frequencies of the symmetric stretching (ω_1) and antisymmetric stretching (ω_3) modes are very close to each other in both ZnH_2 and ZnD_2. For ZnD_2, ω_3 was predicted to be larger than ω_1 by about 30 cm^{-1}. This energy separation is smaller for ZnH_2, and in fact the results of MP2, CCSD(T) and DFT(B3LYP) calculations were inconsistent in determining which vibrational mode has the higher frequency [25,34].

There is no interaction between the $100(\Sigma_g^+)$ and $001(\Sigma_u^+)$ states, because they have opposite *g*/*u* symmetry. However, the 002 and 200 states have the same symmetry (Σ_g^+), and are strongly coupled due to Fermi resonance. The effects of this resonance were clearly observed in the ZnH_2 spectrum: *a*) The zinc isotope shift in the $002(\Sigma_g^+) \rightarrow 001(\Sigma_u^+)$ band of ZnH_2 was unusually small compared to all regular bands (see Figure 5.7), which is an indication of mixing between 002 and 200 states; *b*) The vibrational band origin of the $002(\Sigma_g^+) \rightarrow 001(\Sigma_u^+)$ band of ZnH_2 was unusually high, which indicates that the rotational levels of the $002(\Sigma_g^+)$ state are systematically shifted towards higher energies; *c*) The $B_{[v]}$ value of the $002(\Sigma_g^+)$ state was slightly different from the value predicted by α_3, which indicates that this state is mixed with another state with a different $B_{[v]}$ value; *d*) The $200(\Sigma_g^+) \rightarrow 001(\Sigma_u^+)$ combination band that should be very weak in the absence of resonance appeared in the ZnH_2 spectrum, and it had a small zinc isotope shift in a direction opposite to the shifts for all other bands.

The $002(\Sigma_g^+)$ and $200(\Sigma_g^+)$ states of ZnH_2 are pushed apart due to Fermi resonance. More precisely, rotational levels of the $002(\Sigma_g^+)$ state are shifted towards higher energies, while those of the $200(\Sigma_g^+)$ state are shifted towards lower energies by exactly the same amount. Therefore, for each value of *J*, the sum of their energies remains unchanged. It is straightforward to show that the sum of vibrational energies [$G_{sum} = G_{002} + G_{200}$], rotational constants [$B_{sum} = B_{002} + B_{200}$], and centrifugal distortion constants [$D_{sum} = D_{002} + D_{200}$] also remain unchanged. The effective $G_{[v]}$, $B_{[v]}$ and $D_{[v]}$ constants of the $002(\Sigma_g^+)$ and $200(\Sigma_g^+)$ states of $^{64}ZnH_2$ and $^{66}ZnH_2$ (Tables 5.1 and 5.2) were used to calculate these sums. A Fermi resonance fit was performed for these states using the following 2×2 Hamiltonian matrix, which is similar to the one used for the $100(\Sigma_g^+)$ and $02^00(\Sigma_g^+)$ states of CO_2 [71,72]:

$$\mathbf{H} = \begin{pmatrix} E_\Sigma^0(002) & -K_{00} \\ -K_{00} & E_\Sigma^0(200) \end{pmatrix}. \qquad (5.9)$$

The diagonal elements in the above matrix are simple energy expressions for the Σ states with $G_{[v]}$, $B_{[v]}$ and $D_{[v]}$ constants, and K_{00} is the perturbation matrix element that has no J-dependence. All rotational lines of the 002→001, 200→001 and 003→002 bands of $^{64}ZnH_2$ and $^{66}ZnH_2$ were fitted using the Hamiltonian matrix in Eq. (5.9) for the 002 and 200 states, with the constants for the 001 and 003 states fixed at the previously determined values (Tables 5.1, 5.2 and 5.7). The sums of $G_{[v]}$, $B_{[v]}$ and $D_{[v]}$ constants for the 002(Σ_g^+) and 200(Σ_g^+) states, i.e., G_{sum}, B_{sum} and D_{sum}, were also fixed to the values calculated from Tables 5.1 and 5.2. In order to determine the off-diagonal matrix element (K_{00}) and the unperturbed constants for these states, it was necessary to fix at least one more parameter in the fits. The D_{200} constant was chosen to be fixed to the extrapolated value, i.e., $D_{200} = 2D_{100} - D_{000}$, because the 000($\Sigma_g^+$) and 100($\Sigma_g^+$) states are not perturbed, and their $D_{[v]}$ constants are reliable. Since no rotational line with $J > 16$ was observed for the 100(Σ_g^+) and 200(Σ_g^+) states, only the low-J lines of the 001→000 band were fitted to obtain a comparable D_{000}, appropriate for extrapolation. The D_{200} constants for $^{64}ZnH_2$ and $^{66}ZnH_2$ were then calculated to be 4.8891×10^{-5} and 4.8896×10^{-5} cm^{-1}, respectively, and were held fixed in the least-squares fitting. Only three parameters, i.e., G_{200}, B_{200} and K_{00}, were allowed to vary in the fit, and the results are presented in Table 5.8. The constants of the 002(Σ_g^+) state of $^{64}ZnH_2$ and $^{66}ZnH_2$ were then calculated by subtracting G_{200}, B_{200} and D_{200} from G_{sum}, B_{sum} and D_{sum}, respectively. The constants of Table 5.8 can reproduce all the observed energy levels of the 002 and 200 states within their experimental uncertainties (0.001 or 0.002 cm^{-1}). The off-diagonal matrix elements (K_{00}) were determined to be about 28 cm^{-1} for $^{64}ZnH_2$ and $^{66}ZnH_2$. The unperturbed G_{002} constants in Table 5.8 are about 20 cm^{-1} larger than G_{200}, but this energy separation increases to about 60 cm^{-1} (Tables 5.1 and 5.2) due to the off-diagonal matrix element (K_{00}). Although the unperturbed G_{200} constants of $^{64}ZnH_2$ and $^{66}ZnH_2$ have uncertainties of about 0.02 cm^{-1} in the fits (see Table 5.8), an absolute accuracy of about 0.5 cm^{-1} is estimated for G_{002} and G_{200}, because the D_{200} constants in the fit were fixed to extrapolated values.

The constants of Table 5.8 can be used to calculate the eigenfunctions for the 002(Σ_g^+) and 200(Σ_g^+) states from their basis functions, and to quantify the extent of mixing between the two states. The eigenfunctions of the perturbed states are related to their unperturbed basis functions by the following equations [68]:

$$\left|002', J\right\rangle = c_1\left|002, J\right\rangle - c_2\left|200, J\right\rangle \qquad (5.10)$$

$$\left|2'00,J\right\rangle = c_2\left|002,J\right\rangle + c_1\left|200,J\right\rangle \tag{5.11}$$

In these equations, c_1 and c_2 are equal to cosθ and sinθ, respectively, and of course $c_1^2 + c_2^2 = 1$. For each value of *J*, the mixing coefficients c_1^2 and c_2^2 can be calculated using the following equation [68], which relates θ to the matrix elements of Eq. (5.9):

$$\tan 2\theta = \frac{2K_{00}}{E_\Sigma^0(002) - E_\Sigma^0(200)}. \tag{5.12}$$

The mixing coefficients c_1^2 and c_2^2 were determined for the $J = 0$ to 15 levels of the $002(\Sigma_g^+)$ and $200(\Sigma_g^+)$ states of $^{64}ZnH_2$. The extent of mixing decreases very slowly with increasing *J*; for example, there is a 66% - 34% mixture at $J = 0$, and a 69% - 31% mixture at $J = 15$. Similar calculations for $^{66}ZnH_2$ showed mixing almost to the same extent. Therefore, the observed $002(\Sigma_g^+)$ state of ZnH_2 can be considered approximately as a ⅔:⅓ mixture of the unperturbed 002 and 200 states, and vice versa.

Another way to quantify the mixing between these states is to consider the zinc isotope shifts for the $002(\Sigma_g^+) \rightarrow 001(\Sigma_u^+)$ band. For the unperturbed bands of ZnH_2 in the ν_3 region, i.e., $(v_1,v_2,v_3+1)\rightarrow(v_1,v_2,v_3)$, the observed ^{64}Zn:^{66}Zn isotope shift is about 0.8 cm^{-1}. In other words, ω_3 for $^{64}ZnH_2$ is larger than that of $^{66}ZnH_2$ by about 0.8 cm^{-1}. On the other hand, within the harmonic oscillator approximation, ω_1 has no dependence on the mass of the zinc atoms. Therefore, the ^{64}Zn:^{66}Zn isotope shifts for the $002(\Sigma_g^+) \rightarrow 001(\Sigma_u^+)$ and $200(\Sigma_g^+) \rightarrow 001(\Sigma_u^+)$ bands are expected to be +0.8 and –0.8 cm^{-1}, respectively, in the absence of Fermi resonance. The observed ^{64}Zn:^{66}Zn isotope shift of the $002(\Sigma_g^+) \rightarrow 001(\Sigma_u^+)$ band of ZnH_2 was about +0.2 cm^{-1}, which indicates that the observed $002(\Sigma_g^+)$ state is approximately a 62% - 38% mixture of the unperturbed 002 and 200 states, consistent with the more accurate results obtained from Eqs. (5.10) to (5.12). The energy separation between ω_1 and ω_3 of ZnD_2 is larger than that of ZnH_2 [34], and the Fermi resonance effects in ZnD_2 were not as severe as in ZnH_2. The $200(\Sigma_g^+) \rightarrow 001(\Sigma_u^+)$ combination band was not observed for ZnD_2, because the extent of mixing between the 200 and 002 states is relatively small. In this case, the observed ^{64}Zn:^{66}Zn isotope shift was about 1.2 cm^{-1} for the unperturbed bands in the ν_3 region, and about 1.0 cm^{-1} for the $002(\Sigma_g^+) \rightarrow 001(\Sigma_u^+)$ band. Based on the isotope shifts, it is estimated that the observed $002(\Sigma_g^+)$ state of ZnD_2 is approximately a 92% - 8% mixture of the unperturbed 002 and 200 states. There is yet another way to estimate the mixing coefficients for the 002 and 200 states of ZnD_2. The effective B_{002} constant of $^{64}ZnD_2$

(observed) is related to the unperturbed B_{002}^0 and B_{200}^0 constants by the following equation [73]:

$$B'_{002}(\text{obs.}) \approx c_1^2 B_{002}^0 + c_2^2 B_{200}^0 . \qquad (5.13)$$

The unperturbed B_{002}^0 and B_{200}^0 constants of $^{64}ZnD_2$ were estimated using α_3 and α_1, respectively, and the effective B_{002} constant was taken from Table 5.3. The mixing coefficients, c_1^2 and c_2^2, were found to be 93% and 7%, respectively, consistent with the ones calculated from zinc isotope shifts.

The anomalous zinc isotope shift in the $002(\Sigma_g^+) \rightarrow 001(\Sigma_u^+)$ band of ZnH_2 is illustrated in Figure 5.7, and an approximate energy diagram showing all the observed vibration-rotation bands of $^{64}ZnH_2$ is drawn in Figure 5.8.

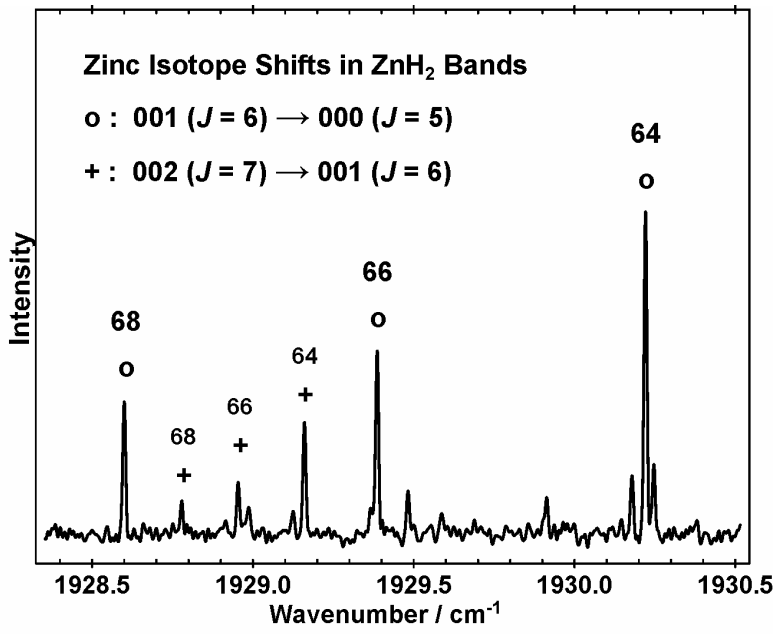

Figure 5.7. An expanded view of the ZnH_2 spectrum showing the zinc isotope shifts in two *R*-branch lines. The zinc isotope shifts in the 002→001 hot band are anomalously small, due to the coupling between 002 and 200 states (Fermi resonance).

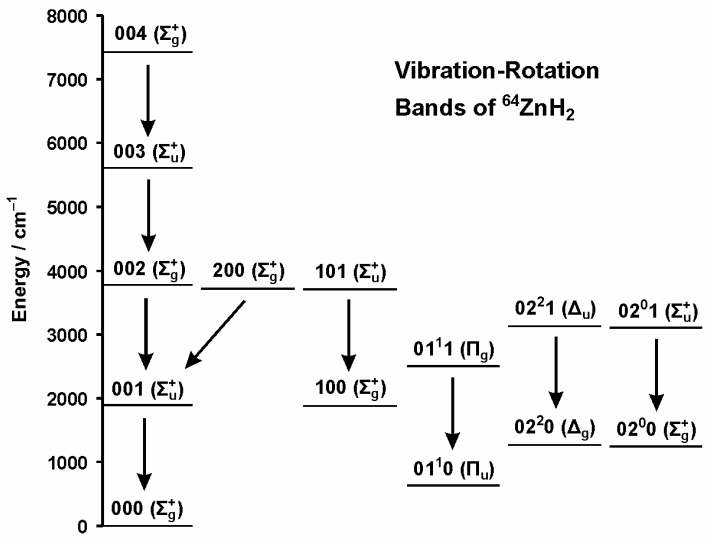

Figure 5.8. An approximate energy level diagram showing the observed vibration-rotation bands of $^{64}ZnH_2$.

Table 5.8. Unperturbed constants (in cm^{-1}) for the 002(Σ_g^+) and 200(Σ_g^+) states of $^{64}ZnH_2$ and $^{66}ZnH_2$.

	$^{64}ZnH_2$		
constant	[002+200] [a]	200 (Σ_g^+) [b]	002 (Σ_g^+) [d]
G	7485.26240 [a]	3733.334(21) [b]	3751.928 [d]
B	6.909050 [a]	3.444130(16) [b]	3.464920 [d]
$10^5\ D$	9.7646 [a]	4.8891 [c]	4.8755 [d]
K_{00} (Σ,Σ)	…	28.1680(73) [b]	
	$^{66}ZnH_2$		
constant	[002+200] [a]	200 (Σ_g^+) [b]	002 (Σ_g^+) [d]
G	7483.63421 [a]	3732.919(23) [b]	3750.715 [d]
B	6.909131 [a]	3.444474(17) [b]	3.464657 [d]
$10^5\ D$	9.7500 [a]	4.8896 [c]	4.8604 [d]
K_{00} (Σ,Σ)	…	28.0694(75) [b]	

[a] Sum of the effective constants for the 200 and 002 states, calculated directly from Tables 7.1 and 7.2, and held fixed in the least-squares fitting (see the text).

[b] These constants were determined by least-squares fitting. The numbers in parentheses are 1σ uncertainties in the last quoted digits.

[c] D_{200} was calculated using D_{000} and D_{100} constants, and held fixed in the fit (see the text).

[d] The unperturbed constants of the 002 state were finally calculated by subtracting G_{200}, B_{200} and D_{200} from G_{sum}, B_{sum} and D_{sum}, respectively (see the text).

5.3.5 Internuclear distances of ZnH_2 and ZnD_2

The B_{000} constants taken from Tables 5.1 to 5.4 were used to determine the r_0 internuclear distances for $^{64}ZnH_2$, $^{66}ZnH_2$, $^{64}ZnD_2$ and $^{66}ZnD_2$. The r_0 distances of $^{64}ZnH_2$ and $^{64}ZnD_2$ are 1.535274(2) Å and 1.531846(3) Å, respectively, their difference being in the fourth significant figure. The vibration-rotation interaction constants, α_1, α_2 and α_3 in Eq. (4.4), were determined from the $B_{[v]}$ values of the 000, 100, 01^10 and 001 levels. The equilibrium rotational constant (B_e) was then calculated for $^{64}ZnH_2$, $^{66}ZnH_2$, $^{64}ZnD_2$ and $^{66}ZnD_2$ using their B_{000} values and the three α's. The equilibrium constants of $^{64}ZnH_2$, $^{66}ZnH_2$, $^{64}ZnD_2$ and $^{66}ZnD_2$ are listed in Table 5.9. Although Eq. (5.8) for $B_{[v]}$ is more accurate than Eq. (4.4), it was not used for calculation of B_e, because a few γ_{ij} constants in Eq. (5.8) could not be determined from the data. The equilibrium centrifugal distortion constant (D_e) was also calculated for $^{64}ZnH_2$, $^{66}ZnH_2$, $^{64}ZnD_2$ and $^{66}ZnD_2$ using a linear equation analogous to Eq. (4.4) for the $D_{[v]}$ values.

Using the B_e values of 3.600269(31) cm^{-1} and 1.801985(25) cm^{-1} for $^{64}ZnH_2$ and $^{64}ZnD_2$, respectively, the equilibrium internuclear distances (r_e) were obtained for these isotopologues independently. The r_e distances were determined to be 1.52413(1) Å and 1.52394(1) Å for $^{64}ZnH_2$ and $^{64}ZnD_2$, respectively. The difference in the r_e values of $^{64}ZnH_2$ and $^{64}ZnD_2$ is very small (only about 0.01%), but still considerably larger than the statistical uncertainties. This discrepancy appears to be due to the breakdown of Born-Oppenheimer approximation or the exclusion of higher order γ_{ij} constants in determination of B_e. In order to examine the contribution of γ_{ij} constants in this discrepancy, the B_e constants of $^{64}ZnH_2$ and $^{64}ZnD_2$ were recalculated, this time from Eq. (5.8), by fixing the γ_{11} constant of $^{64}ZnD_2$ to the mass-scaled value and setting the unknown γ_{12} constants to zero. The new r_e values turned out to be 1.52406(2) Å and 1.52386(3) Å for $^{64}ZnH_2$ and $^{64}ZnD_2$, respectively, and their difference is still about 0.01%. Therefore, it was concluded that the main reason for this discrepancy is the breakdown of the Born-Oppenheimer approximation.

Both r_0 and r_e were determined for the $^{64}ZnH_2$ and $^{64}ZnD_2$ molecules independently, but an average r_s distance was calculated using Eq. (4.9) for comparison. The r_s distance for ZnH_2/ZnD_2 is 1.52841 Å, and lies between the r_0 and r_e values.

5.3.6 Vibrational analyses for ZnH_2 and ZnD_2

The anharmonicity constants x_{13} and x_{23} in Eq. (4.2) were calculated for ZnH_2 and ZnD_2 isotopologues from the vibrational band origins (see Chapter 4). The difference between the 002→001 and 001→000 band origins is equal to $2x_{33}$, but the 002 state is perturbed by Fermi resonance. The unperturbed G_{002} value from Table 5.8 was used to calculate this difference for ZnH_2 and to obtain the x_{33} constant. In the case of ZnD_2, the slightly perturbed G_{002} from Table 5.3 had to be used, and the resultant x_{33} constant is not very reliable.

The equilibrium vibrational frequencies of ZnH_2 and ZnD_2 were estimated using Eqs. (4.10) to (4.12). The ω_1, ω_2 and ω_3 frequencies of $^{64}ZnH_2$ turned out to be 1958, 656 and 1959.72 cm^{-1}, respectively, and those of $^{64}ZnD_2$ are 1385, 474 and 1404.87 cm^{-1}, respectively. These results indicate that ω_3 is larger than ω_1 for both ZnH_2 and ZnD_2 isotopologues, and their difference is larger for ZnD_2. The ω_3 constant of ZnD_2 has an absolute uncertainty of a few cm^{-1}, due to the large uncertainty in the x_{33} constant (see Eq. (4.10). The ω_2 frequency of ZnD_2 has a large uncertainty too, because it depends on ω_3 via Eq. (4.12).

The other constants in Eq. (4.2), i.e., x_{11}, x_{12} and x_{22}, could not be determined from the data, and therefore, the absolute vibrational energies of the $100(\Sigma_g^+)$, $01^10(\Pi_u)$ and $02^20(\Delta_g)$ states are not known with experimental accuracy. However, the vibrational energies of the $200(\Sigma_g^+)$ state of ZnH_2 and the $03^30(\Phi_u)$ state of both ZnH_2 and ZnD_2 (Tables 5.7 and 5.8) have reasonable accuracies, and may be used to estimate roughly the vibrational energies of the 100, 01^10 and 02^20 states.

5.3.7 Isotope effects in ZnH_2 and ZnD_2

For a symmetric linear triatomic molecule such as ZnH_2, the vibrational frequencies of different isotopologues are related by the following equations [73]:

$$\left(\frac{\omega_1^i}{\omega_1}\right)^2 = \left(\frac{m_{\mathrm{H}}}{m_{\mathrm{H}}^i}\right), \tag{5.14}$$

$$\left(\frac{\omega_2^i}{\omega_2}\right)^2 = \left(\frac{\omega_3^i}{\omega_3}\right)^2 = \left(\frac{m_{\mathrm{H}}}{m_{\mathrm{H}}^i}\right)\left(\frac{m_{\mathrm{Zn}}}{m_{\mathrm{Zn}}^i}\right)\left(\frac{M^i}{M}\right). \tag{5.15}$$

In these equations, m_{H} and m_{Zn} are atomic masses of hydrogen (or deuterium) and zinc, respectively, and M is the total mass of the molecule. The observed ^{64}Zn:^{66}Zn isotope shift for the ν_3 fundamental band of ZnH_2 is 0.837 cm^{-1}, which corresponds to a ratio of 1.00044 between the ν_3 fundamentals of $^{64}ZnH_2$ and $^{66}ZnH_2$. The ratio predicted by Eq. (5.15) is 1.00046, and the discrepancy is in the sixth significant figure. Similarly, the observed ^{64}Zn:^{66}Zn isotope shift for the ν_3 fundamental band of ZnD_2 is 1.194 cm^{-1}, corresponding to a ratio of 1.00087 between the ν_3 fundamentals of $^{64}ZnD_2$ and $^{66}ZnD_2$, whereas a ratio of 1.00090 is predicted by Eq. (5.15). The observed ratio between the ν_3 fundamentals of $^{64}ZnH_2$ and $^{64}ZnD_2$ (Table 5.7) is 1.3775 and the predicted ratio from Eq. (5.15) is 1.3926. If one uses the estimated ω_3 frequencies from Table 5.9 instead, the agreement improves and a ratio of 1.3950 is obtained. The observed H:D isotopic ratios for ω_1 and ω_2 of $^{64}ZnH_2$ and $^{64}ZnD_2$ (Table 5.9) are 1.4136 and 1.3849, respectively, and the predicted ratios from Eqs. (5.14) and (5.15) are 1.4137 and 1.3926, respectively.

Simple isotopic relations exist for the B_e, α_1 and D_e constants of symmetric linear triatomic molecules. These constants are not sensitive to the mass of the central atom, and for ZnH_2 they should change only when hydrogen is substituted with deuterium. The mass dependences of the B_e, α_1 and D_e constants are given in the following equations [72-74]:

$$\frac{B_e(^{64}\mathrm{ZnH_2})}{B_e(^{64}\mathrm{ZnD_2})} = \frac{m_{\mathrm{D}}}{m_{\mathrm{H}}}, \tag{5.16}$$

$$\frac{\alpha_1(^{64}\mathrm{ZnH_2})}{\alpha_1(^{64}\mathrm{ZnD_2})} = \left(\frac{m_{\mathrm{D}}}{m_{\mathrm{H}}}\right)^{\frac{3}{2}}, \tag{5.17}$$

$$\frac{D_e(^{64}\mathrm{ZnH_2})}{D_e(^{64}\mathrm{ZnD_2})} = \left(\frac{m_{\mathrm{D}}}{m_{\mathrm{H}}}\right)^2. \tag{5.18}$$

The observed ratios between the B_e, α_1 and D_e constants of $^{64}ZnH_2$ and $^{64}ZnD_2$ are 1.9979, 2.8313 and 3.9912, respectively, whereas the predicted ratios from Eqs. (5.16) to (5.18) are 1.9985, 2.8252 and 3.9939, respectively.

The other constant for which a relatively simple mass dependence can be found is the ℓ-type doubling constant (q). This constant is related to B_e, ω_2 and ω_3 constants via Eq. (4.12), and its mass dependence is obtained by combining Eqs. (4.12), (5.15) and (5.16). The mass dependence of q is thus given by the following equation:

$$\frac{q(^{64}\mathrm{ZnH_2})}{q(^{64}\mathrm{ZnD_2})} = \left(\frac{m_\mathrm{D}}{m_\mathrm{H}}\right)^{\frac{3}{2}} \left[\frac{M(^{64}\mathrm{ZnD_2})}{M(^{64}\mathrm{ZnH_2})}\right]^{\frac{1}{2}}. \tag{5.19}$$

The observed ratio between the q_{010} constants of $^{64}ZnH_2$ and $^{64}ZnD_2$ is 2.8665 while the predicted ratio is 2.8680.

Overall, the observed isotope effects are consistent with theoretical predictions. The r_e distances for all the isotopologues should be the same if the Born-Oppenheimer approximation is exact. As seen in Table 5.9, the r_e values are the same for different isotopes of zinc, within their experimental uncertainties. However, the r_e values of $^{64}ZnH_2$ and $^{64}ZnD_2$ differ in the fifth significant figure, and this is mainly due to the breakdown of Born-Oppenheimer approximation.

Table 5.9. Molecular constants of $^{64}ZnH_2$, $^{66}ZnH_2$, $^{64}ZnD_2$ and $^{66}ZnD_2$ (in cm^{-1}).

Constant	$^{64}ZnH_2$	$^{66}ZnH_2$	$^{64}ZnD_2$	$^{66}ZnD_2$
B_{000}	3.548214(9)	3.548223(9)	1.783424(7)	1.783427(8)
r_0 / Å	1.535274(2)	1.535272(2)	1.531846(3)	1.531845(3)
α_1	0.05186(3) [a]	0.05188(5)	0.01832(3)	0.01827(4)
α_2	0.00531(1)	0.00535(1)	0.00169(1)	0.00169(1)
α_3	0.04162(1)	0.04156(1)	0.01542(1)	0.01538(1)
B_e	3.600269(31)	3.600300(38)	1.801985(25)	1.801940(30)
r_e / Å	1.52413(1)	1.52413(1)	1.52394(1)	1.52396(1)
$10^5 D_e$	4.870(9)	4.875(10)	1.220(4)	1.214(5)
q_{010}	–0.05946(2)	–0.05946(2)	–0.02074(1)	–0.02076(2)
$\nu_3(\sigma_u)$	1889.4326(2)	1888.5955(2)	1371.6310(2)	1370.4370(2)
x_{13}	–61.7764(5)	–61.7624(8)	–31.3209(6)	–31.3042(8)
x_{23}	–12.4657(3)	–12.4443(3)	–6.6386(3)	–6.6172(3)
x_{33}	–13.47(1)	–13.24(1)	–5.47 [b]	–5.36 [b]
$\omega_1(\sigma_g)$	1958 [c]	1957 [c]	1385 [c]	1388 [c]
$\omega_2(\pi_u)$	656 [d]	657 [d]	474 [d]	473 [d]
$\omega_3(\sigma_u)$	1959.72(2)	1958.40(2)	1404.87 [b]	1403.43 [b]
g_{22}	1.645(7)	…	0.907(4)	…

[a] The numbers in parentheses are one standard deviation statistical uncertainties, calculated by propagation of errors.

[b] The constants x_{33} and ω_3 of $^{64}ZnD_2$ are uncertain by a few cm^{-1} (see the text).

[c] Estimated from B_e and D_e, using Eq. (4.11).

[d] Estimated from q_{010}, B_e and ω_3, using Eq. (4.12).

5.4 Analyses of HgH_2 and HgD_2 Spectra

5.4.1 Vibration-rotation bands of HgH_2 and HgD_2

The absolute rotational assignments of the $001(\Sigma_u^+)\rightarrow000(\Sigma_g^+)$ fundamental bands of HgH_2 and HgD_2 were obtained readily as all the low J lines near the band origins were observed. The absolute J assignments were further confirmed by intensity alternations in adjacent rotational lines. The rotational assignment of the $002(\Sigma_g^+)\rightarrow001(\Sigma_u^+)$ and $003(\Sigma_u^+)\rightarrow002(\Sigma_g^+)$ hot bands were obtained consecutively using lower state combination differences, and the energy expression in Eq. (4.3) with $\ell = 0$ was used to fit all these bands. Individual band constants for these vibrational levels of $^{202}HgH_2$, $^{200}HgH_2$, $^{202}HgD_2$ and $^{200}HgD_2$ are listed in Tables 5.10 to 5.13, respectively, and the corresponding constants for the less abundant isotopes of Hg have been reported in the supplementary tables of Ref. [66]. Assignment of the $01^11(\Pi_g)\rightarrow01^10(\Pi_u)$ hot band was based on the observed ℓ-type doubling and the intensity alternations. Lines from the $01^11(\Pi_g)\rightarrow01^10(\Pi_u)$ band of HgH_2 and HgD_2 were fitted using Eq. (4.3) with $\ell = 1$, and the constants are listed in Tables 5.10 to 5.13.

The absolute J assignments of the $101(\Sigma_u^+)\rightarrow100(\Sigma_g^+)$ hot bands of HgH_2 and HgD_2 were difficult to obtain because a few rotational lines near the band origins were missing. Therefore, it was necessary to estimate the $B_{[v]}$ values for the $100(\Sigma_g^+)$ states of HgH_2 and HgD_2 in order to obtain definite J assignments for these bands. First, the $B_{[v]}$ constants of the 000, 01^10 and 001 levels were used to calculate the vibration-rotation interaction constants, α_2 and α_3, for $^{202}HgH_2$ and $^{202}HgD_2$ using Eq. (4.4). The mass-dependences of α_1 and B_e constants given in Eqs. (5.16) and (5.17), respectively, were then used to estimate α_1 for both HgH_2 and HgD_2. More precisely, after determining the α_2 and α_3 constants for both HgH_2 and HgD_2 from Eq. (4.4), there are still four unknowns left, i.e., α_1 and B_e for both isotopologues. There are also four equations that can be solved to determine these unknowns: Eq. (4.4) for both isotopologues, plus Eqs. (5.16) and (5.17). Therefore, α_1 and B_e were estimated for both HgH_2 and HgD_2 with reasonable accuracy, and were used to estimate the $B_{[v]}$ value of the $100(\Sigma_g^+)$ state. The absolute J assignments of the $101(\Sigma_u^+)\rightarrow100(\Sigma_g^+)$ hot bands of HgH_2 and HgD_2 were then obtained immediately, based on the estimated values of B_{100}. Rotational lines of this band were fitted using the energy expression in Eq. (4.3) with $\ell = 0$, and the constants are listed in Tables 5.10 to 5.13. Complete lists of line positions and constants for all observed isotopologues of HgH_2 and HgD_2 have been published in Ref. [66].

Table 5.10. Spectroscopic constants of $^{202}HgH_2$; all uncertainties are 1σ.

	Vibrational levels			
$^{202}HgH_2$	000 (Σ_g^+)	001 (Σ_u^+)	002 (Σ_g^+)	003 (Σ_u^+)
G	0.0	1912.81427(6)	3795.38853(17)	5637.39817(27)
B	3.0848585(37)	3.0550309(34)	3.0231248(40)	2.9851048(58)
$10^5\ D$	2.83129(76)	2.85675(63)	2.90922(94)	3.0813(19)
$^{202}HgH_2$	010 (Π_u)[a]	011 (Π_g)	100 (Σ_g^+)[a]	101 (Σ_u^+)
G	ν_2	1896.67557(16) + ν_2	ν_1	1842.02415(30) + ν_1
B	3.073253(13)	3.043677(12)	3.036964(32)	3.006489(32)
$10^5\ D$	2.8634(53)	2.8879(44)	2.877(24)	2.902(21)
$10^2\ q$	–4.3421(18)	–4.2410(17)	…	…
$10^6\ q_D$	1.56(8)	1.44(7)	…	…

[a] The best ab initio value [36] for ν_1 is 1982 cm^{-1}, and the neon matrix value [24] for ν_2 is 782 cm^{-1}.

Table 5.11. Spectroscopic constants of $^{200}HgH_2$; all uncertainties are 1σ.

	Vibrational levels			
$^{200}HgH_2$	000 (Σ_g^+)	001 (Σ_u^+)	002 (Σ_g^+)	003 (Σ_u^+)
G	0.0	1912.90555(6)	3795.56107(16)	5637.62326(24)
B	3.0848578(39)	3.0550265(36)	3.0231103(41)	2.9850824(55)
$10^5\ D$	2.83101(92)	2.85688(78)	2.90782(98)	3.0864(19)
$^{200}HgH_2$	010 (Π_u)[a]	011 (Π_g)	100 (Σ_g^+)[a]	101 (Σ_u^+)
G	ν_2	1896.76451(22) + ν_2	ν_1	1842.11402(53) + ν_1
B	3.073263(18)	3.043689(16)	3.036962(67)	3.006467(68)
$10^5\ D$	2.8634(88)	2.8916(69)	2.877(65)	2.896(55)
$10^2\ q$	–4.3412(25)	–4.2402(23)	…	…
$10^6\ q_D$	1.46(14)	1.36(11)	…	…

[a] The best ab initio value [36] for ν_1 is 1982 cm^{-1}, and the neon matrix value [24] for ν_2 is 782 cm^{-1}.

Table 5.12. Spectroscopic constants of $^{202}HgD_2$; all uncertainties are 1σ.

	Vibrational levels			
$^{202}HgD_2$	000 (Σ_g^+)	001 (Σ_u^+)	002 (Σ_g^+)	003 (Σ_u^+)
G	0.0	1375.78848(8)	2736.90048(20)	4080.50260(52)
B	1.5511565(26)	1.5405124(26)	1.5294338(30)	1.5173166(77)
$10^5\ D$	0.70542(24)	0.70959(25)	0.71714(36)	0.7377(21)
$^{202}HgD_2$	010 (Π_u)[a]	011 (Π_g)	100 (Σ_g^+)[a]	101 (Σ_u^+)
G	ν_2	1367.58606(21) + ν_2	ν_1	1340.11730(35) + ν_1
B	1.547031(10)	1.536456(10)	1.534289(21)	1.523499(22)
$10^5\ D$	0.7126(20)	0.7188(23)	0.7105(51)	0.7160(54)
$10^2\ q$	–1.52172(74)	–1.49770(78)	…	…

[a] The best ab initio value [36] for ν_1 is 1421 cm^{-1}, and the neon matrix value [24] for ν_2 is 562 cm^{-1}.

Table 5.13. Spectroscopic constants of $^{200}HgD_2$; all uncertainties are 1σ.

	Vibrational levels			
$^{200}HgD_2$	000 (Σ_g^+)	001 (Σ_u^+)	002 (Σ_g^+)	003 (Σ_u^+)
G	0.0	1375.91976(9)	2737.15442(23)	4080.85692(59)
B	1.5511599(31)	1.5405104(31)	1.5294221(36)	1.5172882(90)
$10^5\ D$	0.70558(31)	0.70937(31)	0.71603(45)	0.7297(24)
$^{200}HgD_2$	010 (Π_u)[a]	011 (Π_g)	100 (Σ_g^+)[a]	101 (Σ_u^+)
G	ν_2	1367.71516(25) + ν_2	ν_1	1340.24600(38) + ν_1
B	1.547042(13)	1.536455(14)	1.534306(21)	1.523516(21)
$10^5\ D$	0.7130(28)	0.7167(34)	0.7108(44)	0.7187(42)
$10^2\ q$	–1.52157(86)	–1.49735(89)	…	…

[a] The best ab initio value [36] for ν_1 is 1421 cm^{-1}, and the neon matrix value [24] for ν_2 is 562 cm^{-1}.

For the other dihydrides of Group 12, i.e., ZnH_2 and CdH_2 molecules, local perturbations and Fermi resonance were observed in some vibrational levels [62,65]. The 001 vibrational levels of ZnH_2 and CdH_2 were perturbed locally by the nearby 030 levels because $\nu_3 \approx 3\nu_2$ for these molecules. Strong Fermi resonances were also observed between the $002(\Sigma_g^+)$ and $200(\Sigma_g^+)$ levels because $\nu_3 \approx \nu_1$ for both ZnH_2 and CdH_2 [62,65]. In contrast, these perturbations were not observed in the vibration-rotation bands of HgH_2 and HgD_2. Based on the harmonic vibrational frequencies predicted by Greene et al. [34], ν_1 and $3\nu_2$ are significantly larger than ν_3 for both HgH_2 and HgD_2 molecules, and the above perturbations are not expected.

5.4.2 Internuclear distances of HgH_2 and HgD_2

Similar to the other metal dihydrides, the r_0 internuclear distances of $^{202}HgH_2$, $^{200}HgH_2$, $^{202}HgD_2$ and $^{200}HgD_2$ were determined from the B_{000} values. The r_0 distances obtained for $^{202}HgH_2$ and $^{202}HgD_2$ are 1.646543(1) Å and 1.642535(2) Å, respectively. The $B_{[v]}$ constants of the 000, 100, 01^10 and 001 levels were used to determine α_1, α_2 and α_3 in Eq. (4.4), and the equilibrium rotational constant (B_e) was calculated for $^{202}HgH_2$, $^{200}HgH_2$, $^{202}HgD_2$ and $^{200}HgD_2$. The equilibrium constants of $^{202}HgH_2$, $^{200}HgH_2$, $^{202}HgD_2$ and $^{200}HgD_2$ are listed in Table 5.14. Using the B_e values of 3.135325(24) cm^{-1} and 1.569037(16) cm^{-1} for $^{202}HgH_2$ and $^{202}HgD_2$, respectively, the equilibrium internuclear distances (r_e) were determined to be 1.63324(1) Å and 1.63315(1) Å, respectively. Even though the difference in the r_e values for $^{202}HgH_2$ and $^{202}HgD_2$ is only 0.005%, it is still an order of magnitude larger than the statistical uncertainties. This discrepancy appears to be due to the breakdown of the Born-Oppenheimer approximation. In contrast, the r_e distances for different isotopes of mercury are equal within their statistical uncertainties (see Table 5.14). The r_s distance for HgH_2/HgD_2 estimated from Eq. (4.9) is 1.63851 Å, and lies between the r_0 and r_e values.

5.4.3 Vibrational analyses for HgH_2 and HgD_2

The anharmonicity constants x_{13}, x_{23} and x_{33} in Eq. (4.2) were calculated for $^{202}HgH_2$, $^{200}HgH_2$, $^{202}HgD_2$ and $^{200}HgD_2$ from the vibrational band origins (see Chapter 4). The equilibrium vibrational frequencies of the symmetric stretching (ω_1) and the antisymmetric stretching (ω_3) modes were determined using Eqs. (4.11) and (4.10), respectively. For the $^{202}HgH_2$ and $^{200}HgH_2$ isotopologues, q_{010}, B_e and ω_3 constants from Table 5.14 were used to

obtain ω_2 from Eq. (4.12). It was not possible to determine the ω_2 constants of $^{202}HgD_2$ and $^{200}HgD_2$ from Eq. (4.12) because the third-order equation for ω_2 did not have a solution. The ν_2 fundamental of $^{202}HgD_2$ had been observed at 562 cm^{-1} in solid neon matrix [24]. When this value was used for ω_2 of $^{202}HgD_2$ in Eq. (4.12), along with the B_e and ω_3 values, the predicted q_{010} constant turned out to be –0.01531 cm^{-1}, which differs by less than 1% from the observed value of –0.015217(7) cm^{-1}. It should be noted that Eqs. (4.11) and (4.12) for ω_1 and ω_2 are only approximately correct, and this 1% deviation is not surprising. The vibrational constants of $^{202}HgH_2$, $^{200}HgH_2$, $^{202}HgD_2$ and $^{200}HgD_2$ are also listed in Table 5.14.

5.4.4 Isotope effects in HgH_2 and HgD_2

The theoretical mass-scaling relationships in Eq. (5.14) to (5.19) were used to examine the isotope effects in HgH_2 and HgD_2 isotopologues. The observed ^{200}Hg:^{202}Hg isotope shift for the ν_3 fundamental band of HgH_2 is 0.0913 cm^{-1}, and corresponds to a ratio of 1.0000477 between the ν_3 fundamentals of $^{200}HgH_2$ and $^{202}HgH_2$. The ratio predicted by Eq. (5.15) is 1.0000495. Similarly, the observed ^{200}Hg:^{202}Hg isotope shift for the ν_3 fundamental band of HgD_2 is 0.1313 cm^{-1}, corresponding to a ratio of 1.0000954 between the ν_3 fundamentals of $^{200}HgD_2$ and $^{202}HgD_2$, whereas a ratio of 1.0000979 is predicted by Eq. (5.15). The observed ratio between the ν_3 fundamentals of $^{202}HgH_2$ and $^{202}HgD_2$ (Tables 5.10 and 5.12) is 1.3903 and the predicted ratio from Eq. (5.15) is 1.4067. If one uses the ω_3 wavenumbers from Table 5.14 instead, the agreement improves and a ratio of 1.4081 is obtained. The observed H:D isotopic ratios for ω_1 of $^{202}HgH_2$ and $^{202}HgD_2$ (Table 5.14) is 1.4151, while the predicted ratio from Eq. (5.14) is 1.4137.

The observed ratios between the B_e, α_1 and D_e constants of $^{202}HgH_2$ and $^{202}HgD_2$ (Table 5.14) are 1.99825, 2.840 and 3.984, respectively, whereas the predicted ratios from Eqs. (5.16) to (5.18) are 1.99846, 2.825 and 3.994, respectively. The observed ratio between the q_{010} constants of $^{202}HgH_2$ and $^{202}HgD_2$ is 2.8534, and the predicted ratio from Eq. (5.19) is 2.8391.

Overall, the observed isotope effects are in good agreement with the theoretical predictions. The r_e distances (Table 5.14) are the same for different isotopes of mercury, within their experimental uncertainties. There is a 0.005% difference between the r_e values of $^{202}HgH_2$ and $^{202}HgD_2$ in Table 5.14. This discrepancy can be attributed to the breakdown of the Born-Oppenheimer approximation.

Table 5.14. Molecular constants of $^{202}HgH_2$, $^{200}HgH_2$, $^{202}HgD_2$ and $^{200}HgD_2$ (in cm^{-1}).

constant	$^{202}HgH_2$	$^{200}HgH_2$	$^{202}HgD_2$	$^{200}HgD_2$
B_{000}	3.084859(4)	3.084858(4)	1.551156(3)	1.551160(3)
r_0 / Å	1.646543(1) [a]	1.646543(1)	1.642535(2)	1.642534(2)
α_1	0.04789(3)	0.04790(7)	0.01687(2)	0.01685(2)
α_2	0.01161(1)	0.01160(2)	0.00412(1)	0.00412(1)
α_3	0.029828(5)	0.029831(5)	0.010644(4)	0.010649(4)
B_e	3.135325(24)	3.135316(40)	1.569037(16)	1.569029(19)
r_e / Å	1.63324(1)	1.63324(1)	1.63315(1)	1.63315(1)
$10^5 D_e$	2.76(1)	2.76(3)	0.694(3)	0.694(4)
q_{010}	–0.04342(2)	–0.04341(3)	–0.015217(7)	–0.015216(9)
$\nu_3(\sigma_u)$	1912.81427(6)	1912.90555(6)	1375.78848(8)	1375.91976(9)
x_{13}	–70.7901(3)	–70.7915(5)	–35.6712(4)	–35.6738(4)
x_{23}	–16.1387(2)	–16.1410(2)	–8.2024(2)	–8.2046(3)
x_{33}	–15.1200(1)	–15.1250(1)	–7.3382(2)	–7.3425(2)
$\omega_1(\sigma_g)$	2112 [b]	2112 [b]	1492 [b]	1492 [b]
$\omega_2(\pi_u)$	770 [c]	774 [c]	…	…
$\omega_3(\sigma_u)$	1994.5880(4)	1994.6924(5)	1416.5030(5)	1416.6463(6)

[a] The numbers in parentheses are one standard deviation statistical uncertainties, calculated by propagation of errors.

[b] Estimated from B_e and D_e, using Eq. (4.11).

[c] Estimated from q_{010}, B_e and ω_3, using Eq. (4.12); the neon matrix values [24] for ν_2 of HgH_2 and HgD_2 are 782 cm^{-1} and 562 cm^{-1}, respectively.

5.5 Discussion

5.5.1 Comparison with theoretical predictions

A high level ab initio calculation has been performed by Li et al. [36] to obtain the potential energy surface of the $\widetilde{X}\,^1\Sigma_g^+$ ground electronic state of HgH_2. They computed the potential energy at 13000 points using the multi-reference configuration interaction (MRCI) method with very large basis sets. The potential energy surface was constructed from the ab initio points, and the vibrational energy levels (at $J = 0$) were obtained for HgH_2, HgHD and HgD_2 by solving the exact vibration-rotation Schrödinger equation variationally on this surface. The best available theoretical values for the vibrational energy levels of HgH_2, HgHD and HgD_2 are thus those obtained by Li and co-workers [36]. However, the ν_3 values predicted for HgH_2 and HgD_2 in their calculation are 1885.66 cm^{-1} and 1355.32 cm^{-1}, respectively, while the observed ν_3 values in $^{202}HgH_2$ and $^{202}HgD_2$ in this study are 1912.81427(6) cm^{-1} and 1375.78848(8) cm^{-1}, respectively (Table 5.14). It is interesting to note that even at this high level of theory, the ν_3 values of HgH_2 and HgD_2 are underestimated by about 27 and 20 cm^{-1}, respectively. The equilibrium internuclear distance (r_e) predicted by Li et al. [36] is 1.639 Å, which is larger than the experimental r_e values (Table 5.14) by about 0.006 Å.

There is no similar high level ab initio calculation for ZnH_2 in the literature. The best theoretical constants for ZnH_2, ZnHD and ZnD_2 are those reported by Green et al. [34]. They only calculated the harmonic vibrational frequencies (ω_1, ω_2 and ω_3) and the r_e internuclear distance at various levels of theory. The vibrational frequencies predicted by Green et al. [34] agree with the experimental values within about 30 cm^{-1}. The best theoretical value for r_e distance of ZnH_2 is 1.527 Å [34], which is larger than the experimental r_e (Table 5.9) by about 0.003 Å.

5.5.2 Relative stabilities of gaseous ZnH_2, CdH_2 and HgH_2

Similar to the dihydrides of Group 2 (Chapter 4), dissociation energies of metal-hydrogen bonds in ZnH_2, CdH_2 and HgH_2 can be estimated. High level ab initio calculations [36] predict that the heat of formation of gaseous HgH_2 from mercury vapour and molecular hydrogen is +20.8 kcal/mol, while the dissociation energy of H_2 is 103.3 kcal/mol [75]. The experimental value for the dissociation energy of HgH free radical is 8.6 kcal/mol [75], and thus a dissociation energy of 73.9 kcal/mol is estimated for the first Hg–H bond in HgH_2:

$$HgH_2(g) \rightarrow HgH(g) + H(g) \qquad \Delta E = 73.9 \text{ kcal/mol},$$

$$HgH(g) \rightarrow Hg(g) + H(g) \qquad \Delta E = 8.6 \text{ kcal/mol}.$$

Interestingly, the energy required to break the first Hg–H bond in HgH_2 is more than eight times larger than that for the second bond. Similar patterns exist in the bond dissociation energies of gaseous ZnH_2 and CdH_2, suggesting that average bond strengths should not be used to discuss bonding in these molecules. The best ab initio values for the heats of formation of gaseous ZnH_2 and CdH_2 from ground state metal atoms and molecular hydrogen are +7.6 and +17.0 kcal/mol, respectively [34], and experimental values for dissociation energies of ZnH and CdH free radicals are 19.6 and 15.6 kcal/mol, respectively [75]. Therefore, the dissociation energies of the first metal-hydrogen bond in gaseous ZnH_2 and CdH_2 are estimated to be 76.1 and 70.7 kcal/mol, respectively.

$$ZnH_2(g) \rightarrow ZnH(g) + H(g) \qquad \Delta E = 76.1 \text{ kcal/mol},$$

$$ZnH(g) \rightarrow Zn(g) + H(g) \qquad \Delta E = 19.6 \text{ kcal/mol},$$

$$CdH_2(g) \rightarrow CdH(g) + H(g) \qquad \Delta E = 70.7 \text{ kcal/mol},$$

$$CdH(g) \rightarrow Cd(g) + H(g) \qquad \Delta E = 15.6 \text{ kcal/mol}.$$

The relative energies of gaseous MH and MH_2 molecules (M = Zn, Cd and Hg) are compared in a simple diagram in Figure 5.9.

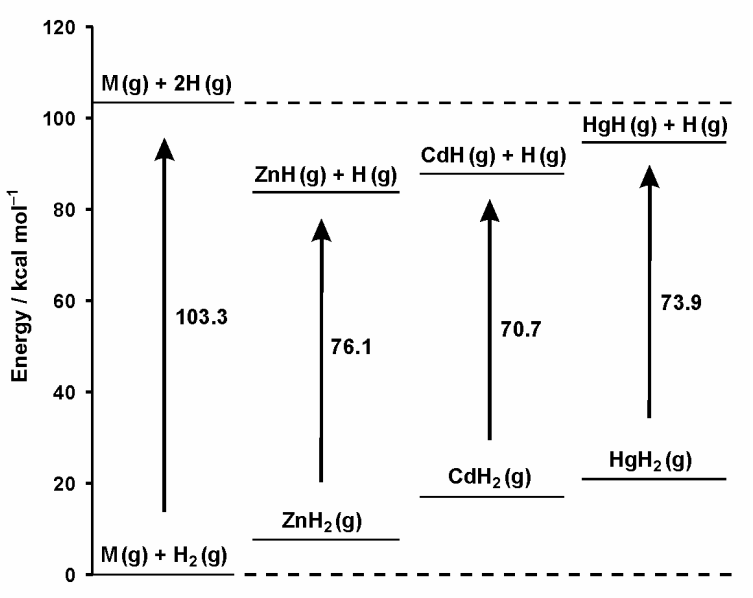

Figure 5.9. A diagram showing the relative energies of Group 12 monohydride and dihydride molecules in the gas phase. For each metal (M), the energy of the ground state M(g) + H_2(g) was taken as zero.

5.6 Summary

Gaseous ZnH_2, ZnD_2, HgH_2 and HgD_2 molecules were discovered, and their high-resolution infrared emission spectra were recorded with a Fourier transform spectrometer. The ν_3 antisymmetric stretching fundamental band and several hot bands in the ν_3 region were rotationally analyzed, and spectroscopic constants were obtained for several isotopologues. Using the rotational constants of the 000 ground states, the r_0 internuclear distances were determined to be 1.535274(2) Å, 1.531846(3) Å, 1.646543(1) Å and 1.642535(2) Å for $^{64}ZnH_2$, $^{64}ZnD_2$, $^{202}HgH_2$ and $^{202}HgD_2$, respectively. Rotational ℓ-type resonance, local perturbations and Fermi resonances were observed in some vibration-rotation bands of ZnH_2 and ZnD_2, but no perturbation was observed in HgH_2 and HgD_2 bands. Equilibrium vibrational frequencies (ω_1, ω_2 and ω_3) were estimated for all the species using Eqs. (4.10) to (4.12). Rotational constants of the 000, 100, 01^10 and 001 levels were used to determine the equilibrium rotational constants (B_e), and the associated equilibrium internuclear distances (r_e) were calculated to be 1.52413(1) Å, 1.52394(1) Å, 1.63324(1) Å and 1.63315(1) Å for $^{64}ZnH_2$, $^{64}ZnD_2$, $^{202}HgH_2$ and $^{202}HgD_2$, respectively. The r_e distances of $^{64}ZnH_2$ and $^{64}ZnD_2$ differ by about 0.01%, and those of $^{202}HgH_2$ and $^{202}HgD_2$ differ by about 0.005%. These discrepancies are larger than the statistical uncertainties by one order of magnitude, and are due to the breakdown of the Born-Oppenheimer approximation.

5.7 References

[1] E. Stokstad, Science 303 (2004) 34.

[2] D.Y. Lu, D.L. Granatstein, D.J. Rose, Ind. Eng. Chem. Res. 43 (2004) 5400-5404.

[3] W.H. Schroeder, J. Munthe, Atmos. Environ. 32 (1998) 809-822.

[4] E.D. Stein, Y. Cohen, A.M. Winer, Crit. Rev. Environ. Sci. Technol. 26 (1996) 1-43.

[5] R.P. Mason, F.M.M. Morel, H.F. Hemond, Water Air Soil Pollut. 80 (1995) 775-787.

[6] T. Barkay, S.M. Miller, A.O. Summers, FEMS Microbiol. Rev. 27 (2003) 355-384.

[7] W.R. Hatch, W.L. Ott, Anal. Chem. 40 (1968) 2085-2087.

[8] R.E. Sturgeon, Z. Mester, Appl. Spectrosc. 56 (2002) 202A-213A.

[9] A. Sanz-Medel, M.C. Valdés-Hevia y Temprano, N. Bordel García, M.R. Fernández de la Campa, Anal. Chem. 67 (1995) 2216-2223.

[10] A.S. Luna, R.E. Sturgeon, R.C. de Campos, Anal. Chem. 72 (2000) 3523-3531.

[11] Y.-L. Feng, R.E. Sturgeon, J.W. Lam, Anal. Chem. 75 (2003) 635-640.

[12] M. Filippelli, F. Baldi, F.E. Brinckman, G.J. Olson, Environ. Sci. Technol. 26 (1992) 1457-1460.

[13] J.H. Weber, Mar. Chem. 65 (1999) 67-75.

[14] J.S. Thayer, *Environmental Chemistry of the Heavy Elements: Hydrido and Organo Compounds*, VCH, New York (1995).

[15] G.D. Barbaras, C. Dillard, A.E. Finholt, T. Wartik, K.E. Wilzbach, H.I. Schlesinger, J. Am. Chem. Soc. 73 (1951) 4585-4590.

[16] E. Wiberg, W. Henle, R. Bauer, Z. Naturforsch. 6b (1951) 393.

[17] E. Wiberg, W. Henle, Z. Naturforsch. 6b (1951) 461-462.

[18] E. Wiberg, Angew. Chem. 65 (1953) 16-33.

[19] W. M. Mueller, J.P. Blackledge, G.G. Libowitz, *Metal Hydrides*, Academic Press, New York (1968).

[20] D.F. Shriver, G.J. Kubas, J.A. Marshall, J. Am. Chem. Soc. 93 (1971) 5076-5079.

[21] J.J. Watkins, E.C. Ashby, Inorg. Chem. 13 (1974) 2350-2354.

[22] E.C. Ashby, J.J. Watkins, in *Inorganic Syntheses XVII*, McGraw-Hill, New York (1977) pp. 6-9.

[23] X. Wang, L. Andrews, Inorg. Chem. 43 (2004) 7146-7150.

[24] X. Wang, L. Andrews, Phys. Chem. Chem. Phys. 7 (2005) 750-759.

[25] X. Wang, L. Andrews, J. Phys. Chem. A 108 (2004) 11006-11013.

[26] H. Smithson, C.A. Marianetti, D. Morgan, A. van der Ven, A. Predith, G. Ceder, Phys. Rev. B 66 (2002) 144107:1-10.

[27] S. Aldridge, A.J. Downs, Chem. Rev. 101 (2001) 3305-3365.

[28] G. Simons, E.R. Talaty, J. Chem. Phys. 66 (1977) 2457-2461.

[29] J. Tyrrell, A. Youakim, J. Phys. Chem. 84 (1980) 3568-3572.

[30] P. Pyykkö, J. Chem. Soc. Faraday Trans. II. 75 (1979) 1256-1276.

[31] M. Dolg, W. Küchle, H. Stoll, H. Preuss, P. Schwerdtfeger, Mol. Phys. 74 (1991) 1265-1285.

[32] P. Schwerdtfeger, G.A. Heath, M. Dolg, M.A. Bennet, J. Am. Chem. Soc. 114 (1992) 7518-7527.

[33] M. Kaupp, H.G. von Schnering, Inorg. Chem. 33 (1994) 4179-4185.

[34] T.M. Greene, W. Brown, L. Andrews, A.J. Downs, G.V. Chertihin, N. Runeberg, P. Pyykkö, J. Phys. Chem. 99 (1995) 7925-7934.

[35] J.A. Platts, J. Mol. Struct. (Theochem) 545 (2001) 111-118.

[36] H. Li, D. Xie, H. Guo, J. Chem. Phys. 122 (2005) 144314:1-7.

[37] A. Bernier, P. Millie, Chem. Phys. Lett. 134 (1987) 245-250.

[38] W.H. Breckenridge, J.-H. Wang, Chem. Phys. Lett. 139 (1987) 28-34.

[39] A. Bernier, P. Millie, J. Chem. Phys. 88 (1988) 4843-4854.

[40] J.M. Martínez-Magadán, A. Ramírez-Solís, O. Novaro, Chem. Phys. Lett. 186 (1991) 107-112.

[41] J.A. Boatz, M. Gutowski, J. Simons, J. Chem. Phys. 96 (1992) 6555-6564.

[42] A. Ramírez-Solís, S. Castillo, J. Chem. Phys. 100 (1994) 8251-8256.

[43] P.E. M. Siegbahn, M. Svensson, R.H. Crabtree, J. Am. Chem. Soc. 117 (1995) 6758-6765.

[44] M.R. Salazar, J. Simons, J. Chem. Phys. 105 (1996) 10919-10924.

[45] M.R. Salazar, J. Simons, J. Chem. Phys. 110 (1999) 229-240.

[46] W.H. Breckenridge, A.M. Renlund, J. Phys. Chem. 82 (1978) 1484-1491.

[47] W.H. Breckenridge, D. Oba, Chem. Phys. Lett. 72 (1980) 455-458.

[48] W.H. Breckenridge, J.-H. Wang, Chem. Phys. Lett. 123 (1986) 17-22.

[49] W.H. Breckenridge, H. Umemoto, J.-H. Wang, Chem. Phys. Lett. 123 (1986) 23-27.

[50] W.H. Breckenridge, W.L. Nikolai, D. Oba, J. Phys. Chem. 90 (1986) 5724-5726.

[51] W.H. Breckenridge, C. Jouvet, B. Soep, J. Chem. Phys. 84 (1986) 1443-1450.

[52] N. Bras, J. Butaux, J.C. Jeannet, D. Perrin, J. Chem. Phys. 85 (1986) 280-285.

[53] W.H. Breckenridge, J.-H. Wang, J. Chem. Phys. 87 (1987) 2630-2637.

[54] N. Bras, J.C. Jeannet, J. Butaux, D. Perrin, J. Chem. Phys. 95 (1991) 1006-1010.

[55] I. Wallace, D.J. Funk, J.G. Kaup, W.H. Breckenridge, J. Chem. Phys. 97 (1992) 3135-3148.

[56] K. Ohmori, T. Takahashi, H. Chiba, K. Saito, T. Nakamura, M. Okunishi, K. Ueda, Y. Sato, J. Chem. Phys. 105 (1996) 7464-7473.

[57] W.H. Breckenridge, J. Phys. Chem. 100 (1996) 14840-14855.

[58] L. Andrews, Chem. Soc. Rev. 33 (2004) 123-132.

[59] Z.L. Xiao, R.H. Hauge, J.L. Margrave, High Temp. Sci. 31 (1991) 59-77.

[60] N. Legay-Sommaire, F. Legay, Chem. Phys. Lett. 207 (1993) 123-128.

[61] N. Legay-Sommaire, F. Legay, J. Phys. Chem. 99 (1995) 16945-16952.

[62] S. Yu, A. Shayesteh, P.F. Bernath, J. Chem. Phys. 122 (2005) 194301:1-6.

[63] A. Shayesteh, D.R.T. Appadoo, I.E. Gordon, P.F. Bernath, J. Am. Chem. Soc. 126 (2004) 14356-14357.

[64] A. Shayesteh, S. Yu, P.F. Bernath, Chem.-Eur. J. 11 (2005) 4709-4712.

[65] A. Shayesteh, I.E. Gordon, D.R.T. Appadoo, P.F. Bernath, Phys. Chem. Chem. Phys. 7 (2005) 3132-3142.

[66] A. Shayesteh, S. Yu, P.F. Bernath, J. Phys. Chem. A 109 (2005) 10280-10286.

[67] A.G. Maki, J.S. Wells, *Wavenumber Calibration Tables from Heterodyne Frequency Measurements*, NIST Special Publication 821, U.S. Government Printing Office, Washington (1991).

[68] P.F. Bernath, *Spectra of Atoms and Molecules*, 2nd ed., Oxford University Press, New York (2005).

[69] J. Koput, private communication.

[70] A.G. Maki, Jr., D.R. Lide, Jr., J. Chem. Phys. 47 (1967) 3206-3210.

[71] D. Papoušek, M.R. Aliev, *Molecular Vibrational-Rotational Spectra*, Elsevier, Amsterdam (1982).

[72] D.M. Dennison, Rev. Mod. Phys. 12 (1940) 175-214.

[73] G. Herzberg, *Molecular Spectra and Molecular Structure II. Infrared and Raman Spectra of Polyatomic Molecules*, Krieger, Malabar, FL (1991).

[74] H.H. Nielsen, Rev. Mod. Phys. 23 (1951) 90-136.

[75] K.P. Huber, G. Herzberg, *Molecular Spectra and Molecular Structure IV. Constants of Diatomic Molecules*, Van Nostrand, New York (1979).

Chapter 6

Summary and Conclusions

Several hydrides of Group 2 and 12 elements were generated in the gas phase using an emission source that combines an electrical discharge with a high temperature furnace, and their high-resolution infrared emission spectra were recorded with a Fourier transform spectrometer. Two classes of molecules were studied: *a*) diatomic metal hydrides BeH, MgH, CaH, SrH, ZnH and CdH; *b*) linear triatomic metal hydrides BeH_2, MgH_2, ZnH_2 and HgH_2.

Infrared emission spectra of BeH, MgH, CaH, SrH, ZnH and CdH free radicals contained several vibration-rotation bands in their $^2\Sigma^+$ ground electronic state. The new data were combined with all the previous ground state data from diode laser infrared spectra and pure rotation spectra available in the literature. Band constants were determined for each observed vibrational level by least-squares fitting of all the data. In addition, empirical Dunham constants and the Born-Oppenheimer breakdown correction parameters were obtained simultaneously from multi-isotopologue fits to the data. The new molecular constants have much higher precision and accuracy in comparison with those obtained in previous studies.

Gaseous BeH_2, MgH_2, ZnH_2 and HgH_2 molecules were discovered and unambiguously identified by their high-resolution infrared emission spectra. The ν_3 antisymmetric stretching fundamental band and several hot bands in the ν_3 region were rotationally analyzed, and spectroscopic constants were obtained for almost all naturally abundant isotopologues. The rotational constants of the 000 ground states were used to determine the r_0 internuclear distances. For BeH_2, ZnH_2, ZnD_2, HgH_2 and HgD_2 molecules, the rotational constants of the

000, 100, $01^{1}0$ and 001 levels were used to determine the equilibrium rotational constants (B_e) and the associated equilibrium internuclear distances (r_e).

The equilibrium vibrational frequencies (ω_e), the first vibrational anharmonicity constants ($\omega_e x_e$) and the equilibrium internuclear distances (r_e) of BeH, MgH, CaH, SrH, ZnH and CdH are compared in Table 6.1. The $\omega_e x_e$ values of ZnH and CdH are relatively large, indicating that their potential energy curves are significantly more anharmonic than those of the alkaline earth monohydrides. There are small differences between the r_e distances of hydrides and deuterides, which are clearly due to the breakdown of the Born-Oppenheimer approximation.

Table 6.1. Equilibrium molecular constants of diatomic hydrides; all uncertainties are 2σ.

Molecule	ω_e / cm^{-1}	$\omega_e x_e$ / cm^{-1}	r_e / Å
^{9}BeH	2061.100(6)	37.077(7)	1.342424(2)
^{9}BeD	1529.886(4)	20.418(4)	1.341731(2)
^{24}MgH	1492.776(7)	29.847(8)	1.729721(1)
^{24}MgD	1077.298(5)	15.521(4)	1.729157(1)
^{40}CaH	1298.348(3)	19.123(4)	2.002360(1)
^{40}CaD	929.894(2)	9.803(2)	2.001462(1)
^{88}SrH	1206.994(4)	17.119(5)	2.146057(1)
^{88}SrD	858.881(3)	8.662(3)	2.145073(1)
^{64}ZnH	1603.181(7)	50.501(9)	1.593478(2)
^{64}ZnD	1143.219(5)	25.661(5)	1.593001(2)
^{114}CdH	1443.474(3)	48.334(3)	1.760098(3)
^{114}CdD	1025.924(2)	24.398(1)	1.759695(2)

The observed vibrational frequencies for the antisymmetric stretching mode, $\nu_3(\sigma_u)$, of BeH_2, MgH_2, ZnH_2, CdH_2 and HgH_2 are listed in Table 6.2. The vibrational frequencies of the $\nu_3(\sigma_u)$ modes of ZnH_2, CdH_2 and HgH_2 lie between those of BeH_2 and MgH_2. The best ab initio theoretical values [1-6] for ν_3, ω_1, ω_2 and ω_3 are also presented in Table 6.2. The agreement between theoretical and experimental ν_3 frequencies is excellent for BeH_2, but more modest for MgH_2 and HgH_2. Furthermore, a clear trend can be seen in the relative magnitudes of $\omega_1(\sigma_g)$ and $\omega_3(\sigma_u)$ frequencies. As the metal atom gets heavier, the ω_1/ω_3 ratio increases.

Table 6.2. Vibrational frequencies (in cm^{-1}) for triatomic hydrides; all uncertainties are 1σ.

Molecule	ν_3 Experiment	ν_3 ab initio	Ref.	ω_1 ab initio	ω_2 ab initio	ω_3 ab initio	Ref.
$^{9}BeH_2$	2178.8659(2)	2178.79	[1]	2052.22	717.18	2254.75	[2]
$^{9}BeD_2$	1689.6788(4)	1689.27	[1]	1450.59	551.31	1736.26	[2]
$^{24}MgH_2$	1588.6716(2)	1575.55	[3]	1601.6	438.0	1628.2	[4]
$^{24}MgD_2$	1176.5028(5)	1166.53	[3]	…	…	…	
$^{64}ZnH_2$	1889.4326(2)	…		1926	637	1921	[5]
$^{64}ZnD_2$	1371.6310(2)	…		1362	458	1379	[5]
$^{114}CdH_2$	1771.5296(2)[a]	…		1850	593	1829	[5]
$^{114}CdD_2$	1278.3117(3)[a]	…		1309	423	1305	[5]
$^{202}HgH_2$	1912.8143(1)	1885.66	[6]	2082	802	1960	[5]
$^{202}HgD_2$	1375.7885(1)	1355.32	[6]	1473	570	1393	[5]

[a] From Ref. [7].

The internuclear distances of BeH_2, MgH_2, ZnH_2, CdH_2 and HgH_2 molecules are compared in Table 6.3. The r_0 distances were determined for all the species, and it was found that the r_0 internuclear distances of ZnH_2, CdH_2 and HgH_2 lie between those of BeH_2 and MgH_2. The difference between the r_0 distances in each MH_2/MD_2 pair is in the fourth significant figure, and is due to the fact that the 000 ground state of MD_2 lies lower than that of MH_2 on the potential energy surface. The equilibrium r_e distance could be obtained only

for BeH_2, ZnH_2, ZnD_2, HgH_2 and HgD_2. The r_e distances of ZnH_2 and ZnD_2 differ by about 0.01%, and those of HgH_2 and HgD_2 differ by about 0.005%. These discrepancies are larger than the statistical uncertainties by one order of magnitude, and are attributed to the breakdown of the Born-Oppenheimer approximation. The ab initio theoretical values for r_e are also presented in Table 6.3 for comparison, among which the theoretical r_e distance of BeH_2 shows the best agreement with experiment. Average r_s distances were also estimated for each MH_2/MD_2 pair. The estimated r_s values lie between r_0 and r_e values, consistent with the predictions of Watson [8] about the relative magnitudes of r_0, r_s and r_e. It is also interesting to note that the r_s distances are almost exactly in the middle of r_e and r_0 for MD_2 isotopologues, see Table 6.3.

Table 6.3. Internuclear distances (in Å) for triatomic hydrides; all uncertainties are 1σ.

Molecule	r_0	r_s	r_e	r_e (ab initio)	Ref.
$^{9}BeH_2$	1.333758(1)	1.32896	1.326376(3)	1.3265	[1]
$^{9}BeD_2$	1.331361(4)		…		
$^{24}MgH_2$	1.703327(3)	1.69841	…	1.7096	[3]
$^{24}MgD_2$	1.700874(8)		…		
$^{64}ZnH_2$	1.535274(2)	1.52841	1.52413(1)	1.527	[5]
$^{64}ZnD_2$	1.531846(3)		1.52394(1)		
$^{114}CdH_2$	1.683034(2)[a]	1.67528[a]	…	1.668	[5]
$^{114}CdD_2$	1.679172(5)[a]		…		
$^{202}HgH_2$	1.646543(1)	1.63851	1.63324(1)	1.639	[6]
$^{202}HgD_2$	1.642535(2)		1.63315(1)		

[a] From Ref. [7].

Finally, the equilibrium metal-hydrogen internuclear distances of MH free radicals (Table 6.1) are slightly larger than those of the corresponding MH_2 molecules (Table 6.3). For example, the M–H distances of BeH and ZnH are larger than those of BeH_2 and ZnH_2 by about 1% and 4%, respectively.

6.1 References

[1] H. Li, R. J. Le Roy, J. Chem. Phys. (2006) in press.

[2] J. Koput, K.A. Peterson, J. Chem. Phys. (2006) submitted.

[3] H. Li, D. Xie, H. Guo, J. Chem. Phys. 121 (2004) 4156-4163.

[4] G.S. Tschumper, H.F. Schaefer, J. Chem. Phys. 108 (1998) 7511-7515.

[5] T.M. Greene, W. Brown, L. Andrews, A.J. Downs, G.V. Chertihin, N. Runeberg, P. Pyykkö, J. Phys. Chem. 99 (1995) 7925-7934.

[6] H. Li, D. Xie, H. Guo, J. Chem. Phys. 122 (2005) 144314:1-7.

[7] S. Yu, A. Shayesteh, P.F. Bernath, J. Chem. Phys. 122 (2005) 194301:1-6.

[8] J.K.G. Watson, J. Mol. Spectrosc. 48 (1973) 479-502.

Appendix

Table A1. Line positions (in cm^{-1}) for the $001(\Sigma_u^+) \rightarrow 000(\Sigma_g^+)$ band of $^9BeH_2$.[a]

J'	J''	Wavenumber	Obs – Calc	J'	J''	Wavenumber	Obs – Calc
38	37	2415.2724	0.0000	0	1	2169.4633	-0.0003
37	36	2412.4101	-0.0009	1	2	2159.9251	-0.0002
36	35	2409.3578	0.0001	2	3	2150.2534	-0.0003
35	34	2406.1100	-0.0030	3	4	2140.4510	-0.0003
34	33	2402.6791	0.0021	4	5	2130.5204	-0.0004
33	32	2399.0547	0.0045	5	6	2120.4645	-0.0004
32	31	2395.2346	0.0016	6	7	2110.2861	-0.0001
31	30	2391.2267	0.0009	7	8	2099.9872	-0.0003
30	29	2387.0307	0.0012	8	9	2089.5711	-0.0003
29	28	2382.6450	0.0004	9	10	2079.0413	0.0004
28	27	2378.0722	0.0004	10	11	2068.3986	0.0000
27	26	2373.3112	-0.0007	11	12	2057.6475	0.0001
26	25	2368.3649	-0.0009	12	13	2046.7906	0.0006
25	24	2363.2332	-0.0012	13	14	2035.8294	0.0000
24	23	2357.9169	-0.0019	14	15	2024.7687	0.0004
23	22	2352.4196	-0.0005	15	16	2013.6100	0.0004
22	21	2346.7138 [b]	-0.0254	16	17	2002.3567	0.0005
21	20	2340.8797	0.0021	17	18	1991.0115	0.0006
20	19	2334.8370	0.0005	18	19	1979.5773	0.0006
19	18	2328.6179	0.0006	19	20	1968.0576	0.0013
18	17	2322.2210	-0.0003	20	21	1956.4530	0.0005
17	16	2315.6495	-0.0006	21	22	1944.7708	0.0025
16	15	2308.9046	-0.0005	22	23	1932.9816 [b]	-0.0248
15	14	2301.9879	-0.0002	23	24	1921.1660	-0.0038
14	13	2294.9003	-0.0003	24	25	1909.2587	-0.0023
13	12	2287.6444	-0.0001	25	26	1897.2808	-0.0021
12	11	2280.2215	-0.0001	26	27	1885.2367	-0.0016
11	10	2272.6347	0.0011	27	28	1873.1278	-0.0019
10	9	2264.8816	-0.0010	28	29	1860.9594	-0.0006
9	8	2256.9706	0.0002	29	30	1848.7266	-0.0051
8	7	2248.8995	0.0002	30	31	1836.4484	0.0009
7	6	2240.6717	0.0005	31	32	1824.1102	0.0003
6	5	2232.2885	0.0003	32	33	1811.7249	0.0037
5	4	2223.7525	-0.0001				
4	3	2215.0632	-0.0034				
3	2	2206.2332	0.0005				
2	1	2197.2547	0.0018				
1	0	2188.1294	-0.0004				

[a] The observed-minus-calculated values have been computed using the constants of Table 4.1 for the 000 and 001 states.

[b] These lines were not included in the fit; the discrepancy of about –0.025 cm^{-1} for the $J' = 22$ level is clearly due to a perturbation (see Chapter 4).

Table A2. Line positions (in cm^{-1}) for the $001(\Sigma_u^+) \rightarrow 000(\Sigma_g^+)$ band of $^9BeD_2$.[a]

J'	J''	Wavenumber	Obs – Calc	J'	J''	Wavenumber	Obs – Calc
29	28	1797.7665 [b]	0.0190	1	2	1680.1748	0.0006
28	27	1795.0018	0.0004	3	4	1670.4343	0.0051
27	26	1792.1835	-0.0006	4	5	1665.4685	0.0005
26	25	1789.2959	0.0008	5	6	1660.4474	-0.0013
25	24	1786.3325	-0.0022	6	7	1655.3714	-0.0004
24	23	1783.3053	0.0027	7	8	1650.2395	0.0014
23	22	1780.1993	0.0005	9	10	1639.8002	-0.0027
22	21	1777.0218	-0.0016	10	11	1634.5017	-0.0011
21	20	1773.7767	0.0000	11	12	1629.1471	-0.0015
20	19	1770.4593	0.0007	12	13	1623.7412	0.0001
19	18	1767.0684	-0.0011	13	14	1618.2783	-0.0026
18	17	1763.6060	-0.0034	14	15	1612.7667	-0.0022
17	16	1760.0785	-0.0004	15	16	1607.2025	-0.0033
16	15	1756.4807	0.0026	16	17	1601.5927	0.0002
15	14	1752.8075	0.0001	17	18	1595.9303	0.0006
14	13	1749.0668	-0.0004	18	19	1590.2204	0.0021
13	12	1745.2568	-0.0012	19	20	1584.4612	0.0021
12	11	1741.3807	0.0006	20	21	1578.6548	0.0018
11	10	1737.4345	0.0004	21	22	1572.8032	0.0022
10	9	1733.4185	-0.0019	22	23	1566.9041	0.0002
9	8	1729.3408	0.0013	23	24	1560.9622	-0.0006
8	7	1725.1919	0.0000	24	25	1554.9791	0.0005
7	6	1720.9811	0.0029	25	26	1548.9519	-0.0006
6	5	1716.6979	-0.0011	26	27	1542.8825	-0.0031
5	4	1712.3551	0.0004	27	28	1536.7765	-0.0024
3	2	1703.4802	0.0068	28	29	1530.6323	-0.0016
				29	30	1524.4709 [b]	0.0194
				31	32	1511.9808	0.0004

[a] The observed-minus-calculated values have been computed using the constants of Table 4.2 for the 000 and 001 states.

[b] These lines were not included in the fit; the discrepancy of about +0.019 cm^{-1} for the $J' = 29$ level is clearly due to a perturbation (see Chapter 4).

Table A3. Line positions (in cm^{-1}) for the $001(\Sigma_u^+) \rightarrow 000(\Sigma_g^+)$ band of $^{24}MgH_2$.[a]

J'	J''	Wavenumber	Obs – Calc	J'	J''	Wavenumber	Obs – Calc
30	29	1726.1501	-0.0048	0	1	1582.9065	-0.0001
28	27	1719.3386	0.0001	1	2	1577.0738	-0.0007
26	25	1712.1626	0.0001	2	3	1571.1767	0.0002
24	23	1704.6319	0.0003	3	4	1565.2155	0.0020
23	22	1700.7389	0.0041	4	5	1559.1867	0.0004
22	21	1696.7513	0.0002	5	6	1553.0933	-0.0029
21	20	1692.6794	-0.0018	6	7	1546.9445	0.0008
20	19	1688.5263	0.0003	7	8	1540.7292	-0.0009
19	18	1684.2864	0.0005	8	9	1534.4569	0.0005
18	17	1679.9607	-0.0012	9	10	1528.1244	0.0011
17	16	1675.5565	0.0019	10	11	1521.7316	-0.0003
16	15	1671.0645	-0.0003	11	12	1515.2838	0.0005
15	14	1666.4919	-0.0014	13	14	1502.2176	-0.0005
14	13	1661.8409	0.0001	14	15	1495.6029	-0.0005
13	12	1657.1066	-0.0015	15	16	1488.9360	0.0007
12	11	1652.2959	-0.0001	16	17	1482.2138	-0.0011
10	9	1642.4374	0.0002	17	18	1475.4443	0.0012
9	8	1637.3909	-0.0011	18	19	1468.6206	-0.0002
8	7	1632.2703	-0.0006	19	20	1461.7492	0.0001
7	6	1627.0746	0.0000	20	21	1454.8288	0.0000
6	5	1621.8047	0.0006	21	22	1447.8610	0.0000
5	4	1616.4613	0.0012	22	23	1440.8472	0.0005
4	3	1611.0441	0.0004	24	25	1426.6819	-0.0003
3	2	1605.5584	0.0026	26	27	1412.3408	-0.0021
2	1	1599.9963	-0.0008	30	31	1383.1706	0.0001
				32	33	1368.3525	0.0001

[a] The observed-minus-calculated values have been computed using the constants of Table 4.6 for the 000 and 001 states.

Table A4. Line positions (in cm^{-1}) for the $001(\Sigma_u^+) \rightarrow 000(\Sigma_g^+)$ band of $^{24}MgD_2$.[a]

J'	J''	Wavenumber	Obs – Calc	J'	J''	Wavenumber	Obs – Calc
33	32	1255.7142	-0.0010	4	5	1161.7764	0.0012
31	30	1251.8824	0.0018	5	6	1158.7515	-0.0006
30	29	1249.9150	0.0013	6	7	1155.7024	-0.0015
26	25	1241.7188	-0.0006	7	8	1152.6289	-0.0016
25	24	1239.5880	-0.0021	8	9	1149.5300	-0.0024
24	23	1237.4242	-0.0047	9	10	1146.4112	0.0015
21	20	1230.7547	-0.0007	11	12	1140.0935	0.0018
19	18	1226.1510	0.0005	12	13	1136.8975	0.0006
17	16	1221.4244	0.0018	13	14	1133.6775	-0.0010
16	15	1219.0145	0.0015	14	15	1130.4315	-0.0054
15	14	1216.5708	-0.0024	15	16	1127.1724	0.0004
13	12	1211.6035	-0.0006	17	18	1120.5743	-0.0001
12	11	1209.0786	0.0034	19	20	1113.8870	-0.0005
11	10	1206.5151	-0.0019	21	22	1107.1143	0.0008
9	8	1201.3190	0.0057	23	24	1100.2550	0.0005
8	7	1198.6693	0.0009	24	25	1096.7928	-0.0010
7	6	1195.9973	0.0024	25	26	1093.3130	0.0004
5	4	1190.5640	0.0003	26	27	1089.8115	0.0002
				27	28	1086.2911	0.0011
				29	30	1079.1882	-0.0006
				30	31	1075.6099	0.0005
				31	32	1072.0120	0.0007
				33	34	1064.7581	-0.0014

[a] The observed-minus-calculated values have been computed using the constants of Table 4.7 for the 000 and 001 states.

Table A5. Line positions (in cm^{-1}) for the $001(\Sigma_u^+) \rightarrow 000(\Sigma_g^+)$ band of $^{64}ZnH_2$.[a]

J'	J''	Wavenumber	Obs – Calc	J'	J''	Wavenumber	Obs – Calc
28	27	2050.0316	0.0028	0	1	1882.3363	-0.0002
27	26	2045.7036	-0.0013	1	2	1875.1581	0.0000
26	25	2041.2686	0.0019	2	3	1867.8986	-0.0004
25	24	2036.7171	0.0018	3	4	1860.5598	-0.0003
24	23	2032.0519	0.0001	4	5	1853.1426	-0.0001
23	22	2027.2768	-0.0002	5	6	1845.6480	0.0001
22	21	2022.3923	0.0002	6	7	1838.0768	-0.0002
21	20	2017.3987	0.0009	7	8	1830.4308	-0.0002
20	19	2012.2947	-0.0004	8	9	1822.7112	-0.0001
19	18	2007.0826	-0.0006	9	10	1814.9187	-0.0002
18	17	2001.7494	-0.0005	10	11	1807.0547	-0.0002
17	16	1996.4017	-0.0002	11	12	1799.1204	-0.0003
16	15	1990.8564	-0.0001	12	13	1791.1174	-0.0001
15	14	1985.2288	-0.0003	13	14	1783.0444	-0.0019
14	13	1979.5036	0.0000	14	15	1774.9086	-0.0001
13	12	1973.6792	-0.0001	15	16	1766.7060	-0.0002
12	11	1967.7571	0.0002	16	17	1758.4420	0.0002
11	10	1961.7379	0.0005	17	18	1750.1340	0.0000
10	9	1955.6221	0.0004	18	19	1741.6695	-0.0001
9	8	1949.4111	0.0002	19	20	1733.2345	0.0009
8	7	1943.1068	0.0004	20	21	1724.7215	0.0000
7	6	1936.7095	0.0003	21	22	1716.1484	0.0006
6	5	1930.2209	0.0004	22	23	1707.5146	-0.0007
5	4	1923.6419	0.0004	23	24	1698.8250	-0.0005
4	3	1916.9735	0.0002	24	25	1690.0795	-0.0003
3	2	1910.2174	0.0003	25	26	1681.2767	-0.0025
2	1	1903.3744	0.0002	26	27	1672.4235	-0.0016
1	0	1896.4452	-0.0004	27	28	1663.5176	-0.0007
				28	29	1654.5631	0.0029

[a] The observed-minus-calculated values have been computed using the constants of Table 5.1 for the 000 state and those of Table 5.7 for the perturbed 001 state.

Table A6. Line positions (in cm^{-1}) for the $001(\Sigma_u^+) \rightarrow 000(\Sigma_g^+)$ band of $^{66}ZnH_2$.[a]

J'	J''	Wavenumber	Obs – Calc	J'	J''	Wavenumber	Obs – Calc
26	25	2040.4717	0.0012	0	1	1881.4988	-0.0004
24	23	2031.2488	-0.0013	1	2	1874.3212	0.0002
23	22	2026.4730	0.0002	2	3	1867.0621	0.0001
22	21	2021.5853	0.0001	3	4	1859.7231	-0.0004
21	20	2016.5893	0.0007	4	5	1852.3064	-0.0002
20	19	2011.4826	-0.0008	5	6	1844.8123	-0.0001
19	18	2006.2701	0.0011	6	7	1837.2421	-0.0001
18	17	2000.9319	-0.0006	7	8	1829.5968	-0.0003
17	16	1995.5818	-0.0003	8	9	1821.8782	-0.0001
16	15	1990.0356	-0.0002	9	10	1814.0870	0.0001
15	14	1984.4065	-0.0001	10	11	1806.2243	0.0001
14	13	1978.6795	0.0002	11	12	1798.2912	-0.0001
13	12	1972.8531	-0.0003	12	13	1790.2893	-0.0002
12	11	1966.9295	0.0001	13	14	1782.2198	-0.0002
11	10	1960.9085	0.0002	14	15	1774.0839	-0.0001
10	9	1954.7918	0.0005	15	16	1765.8834	0.0002
9	8	1948.5796	0.0002	16	17	1757.6208	0.0002
8	7	1942.2739	0.0002	17	18	1749.3140	0.0003
7	6	1935.8758	0.0002	18	19	1740.8511	-0.0006
6	5	1929.3865	0.0006	19	20	1732.4176	-0.0012
5	4	1922.8062	0.0000	20	21	1723.9090	0.0000
4	3	1916.1375	0.0001	21	22	1715.3388	0.0011
3	2	1909.3814	0.0006	22	23	1706.7080	0.0004
2	1	1902.5378	0.0004	23	24	1698.0204	0.0002
1	0	1895.6075	-0.0010	24	25	1689.2768	-0.0001
				26	27	1671.6268	-0.0004

[a] The observed-minus-calculated values have been computed using the constants of Table 5.2 for the 000 state and those of Table 5.7 for the perturbed 001 state.

Table A7. Line positions (in cm^{-1}) for the $001(\Sigma_u^+) \rightarrow 000(\Sigma_g^+)$ band of $^{64}ZnD_2$.[a]

J'	J''	Wavenumber	Obs – Calc	J'	J''	Wavenumber	Obs – Calc
35	34	1474.9665	0.0030	0	1	1368.0615	-0.0028
34	33	1472.6481	0.0005	1	2	1364.4676	0.0008
33	32	1470.2905	-0.0008	2	3	1360.8387	-0.0006
32	31	1467.8951	0.0005	3	4	1357.1814	-0.0003
31	30	1465.4598	0.0017	4	5	1353.4936	-0.0008
30	29	1462.9806	-0.0013	5	6	1349.7778	0.0000
29	28	1460.4663	0.0002	6	7	1346.0313	-0.0008
28	27	1457.9093	-0.0021	7	8	1342.2576	0.0000
27	26	1455.3172	-0.0004	8	9	1338.4546	-0.0001
26	25	1452.6858	0.0006	9	10	1334.6233	-0.0002
25	24	1450.0137	-0.0006	10	11	1330.7645	0.0001
24	23	1447.3046	-0.0003	11	12	1326.8777	-0.0001
23	22	1444.5548	-0.0006	12	13	1322.9638	-0.0001
22	21	1441.8133	-0.0006	13	14	1319.0229	0.0000
21	20	1438.9619	-0.0002	14	15	1315.0548	-0.0005
20	19	1436.1022	0.0003	15	16	1311.0612	0.0000
19	18	1433.2115	0.0049	16	17	1307.0410	-0.0001
18	17	1430.2757	0.0002	17	18	1302.9955	0.0003
17	16	1427.3086	0.0003	18	19	1298.9239	0.0001
16	15	1424.3057	0.0001	19	20	1294.8275	0.0001
15	14	1421.2675	0.0003	20	21	1290.7064	0.0000
14	13	1418.1935	-0.0004	21	22	1286.5625	0.0002
13	12	1415.0863	0.0007	22	23	1282.4226	0.0002
12	11	1411.9402	-0.0024	23	24	1278.1853	0.0000
11	10	1408.7654	0.0002	24	25	1273.9694	-0.0006
10	9	1405.5540	0.0001	25	26	1269.7289	0.0001
9	8	1402.3095	0.0007	26	27	1265.4635	-0.0005
8	7	1399.0305	0.0004	27	28	1261.1761	0.0000
7	6	1395.7189	0.0006	28	29	1256.8666	0.0012
6	5	1392.3725	-0.0012	29	30	1252.5321	-0.0003
5	4	1388.9965	0.0001	30	31	1248.1775	0.0002
4	3	1385.5863	-0.0005	31	32	1243.8014	0.0010
3	2	1382.1457	0.0006	32	33	1239.4022	0.0001
2	1	1378.6723	0.0005	33	34	1234.9822	-0.0004
1	0	1375.1678	0.0009	34	35	1230.5416	-0.0006
				35	36	1226.0815	0.0002

[a] The observed-minus-calculated values have been computed using the constants of Table 5.3 for the 000 state and those of Table 5.7 for the perturbed 001 state.

Table A8. Line positions (in cm^{-1}) for the $001(\Sigma_u^+) \rightarrow 000(\Sigma_g^+)$ band of $^{66}ZnD_2$.[a]

J'	J''	Wavenumber	Obs – Calc	J'	J''	Wavenumber	Obs – Calc
35	34	1473.8241	0.0048	0	1	1366.8747	0.0044
33	32	1469.1425	0.0003	2	3	1359.6441	-0.0015
32	31	1466.7429	-0.0003	3	4	1355.9878	-0.0004
31	30	1464.3006	-0.0036	4	5	1352.3004	-0.0009
30	29	1461.8251	-0.0005	5	6	1348.5847	-0.0003
29	28	1459.3086	0.0010	6	7	1344.8402	0.0004
28	27	1456.7506	0.0001	7	8	1341.0656	-0.0003
27	26	1454.1540	-0.0005	8	9	1337.2639	0.0003
26	25	1451.5189	-0.0011	9	10	1333.4328	-0.0004
25	24	1448.8459	-0.0010	10	11	1329.5748	-0.0001
24	23	1446.1346	-0.0007	11	12	1325.6890	-0.0002
23	22	1443.3840	0.0007	12	13	1321.7757	-0.0005
22	21	1440.6356	0.0009	13	14	1317.8365	0.0001
21	20	1437.7876	0.0004	14	15	1313.8705	0.0006
20	19	1434.9264	0.0010	15	16	1309.8774	0.0003
19	18	1432.0281	-0.0003	16	17	1305.8580	-0.0003
18	17	1429.0964	0.0008	17	18	1301.8134	-0.0004
17	16	1426.1273	0.0003	18	19	1297.7443	0.0003
16	15	1423.1223	-0.0005	19	20	1293.6489	-0.0003
15	14	1420.0831	-0.0002	20	21	1289.5292	-0.0008
14	13	1417.0079	-0.0006	21	22	1285.3877	0.0001
13	12	1413.8991	0.0001	22	23	1281.2422	-0.0013
12	11	1410.7555	0.0005	23	24	1277.0111	-0.0024
11	10	1407.5771	0.0004	24	25	1272.8015	0.0009
10	9	1404.3649	0.0004	25	26	1268.5614	-0.0003
9	8	1401.1183	-0.0002	26	27	1264.2992	0.0001
7	6	1394.5255	-0.0012	27	28	1260.0124	-0.0010
6	5	1391.1813	-0.0002	28	29	1255.7057	0.0006
5	4	1387.8059	0.0022	29	30	1251.3741	-0.0003
4	3	1384.3918	-0.0019	30	31	1247.0237	0.0019
3	2	1380.9517	0.0000	31	32	1242.6466	-0.0008
2	1	1377.4798	0.0017	32	33	1238.2526	0.0010
1	0	1373.9742	0.0011	33	34	1233.8327	-0.0019
				35	36	1224.9387	0.0004

[a] The observed-minus-calculated values have been computed using the constants of Table 5.4 for the 000 state and those of Table 5.7 for the perturbed 001 state.

Table A9. Line positions (in cm^{-1}) for the $001(\Sigma_u^+) \rightarrow 000(\Sigma_g^+)$ band of $^{202}HgH_2$.[a]

J'	J''	Wavenumber	Obs – Calc	J'	J''	Wavenumber	Obs – Calc
26	25	2050.1721	0.0002	0	1	1906.6447	0.0001
24	23	2041.3332	-0.0004	1	2	1900.4158	-0.0003
22	21	2032.1845	0.0003	2	3	1894.1292	0.0000
21	20	2027.4948	-0.0001	3	4	1887.7847	0.0000
19	18	2017.8908	-0.0001	4	5	1881.3831	-0.0001
18	17	2012.9780	0.0001	5	6	1874.9254	0.0000
17	16	2007.9921	0.0001	6	7	1868.4119	0.0000
16	15	2002.9337	-0.0002	7	8	1861.8434	0.0001
15	14	1997.8046	0.0001	8	9	1855.2205	0.0000
14	13	1992.6045	0.0000	9	10	1848.5439	0.0001
13	12	1987.3347	0.0000	10	11	1841.8140	0.0000
12	11	1981.9959	0.0000	11	12	1835.0319	0.0003
11	10	1976.5887	-0.0001	12	13	1828.1974	0.0000
10	9	1971.1141	0.0000	13	14	1821.3112	-0.0007
9	8	1965.5726	-0.0001	14	15	1814.3755	-0.0002
8	7	1959.9651	0.0000	15	16	1807.3885	-0.0009
7	6	1954.2923	0.0000	16	17	1800.3540	0.0004
6	5	1948.5549	0.0000	17	18	1793.2688	0.0000
5	4	1942.7539	0.0002	18	19	1786.1355	-0.0001
4	3	1936.8893	0.0001				
3	2	1930.9624	0.0000				
2	1	1924.9739	0.0000				
1	0	1918.9242	0.0000				

[a] The observed-minus-calculated values have been computed using the constants of Table 5.10 for the 000 and 001 states.

Table A10. Line positions (in cm^{-1}) for the $001(\Sigma_u^+) \rightarrow 000(\Sigma_g^+)$ band of $^{200}HgH_2$.[a]

J'	J''	Wavenumber	Obs – Calc	J'	J''	Wavenumber	Obs – Calc
26	25	2050.2588	0.0000	0	1	1906.7359	-0.0001
25	24	2045.8794	0.0000	1	2	1900.5081	0.0007
23	22	2036.8870	0.0014	2	3	1894.2204	0.0000
22	21	2032.2731	0.0004	3	4	1887.8759	-0.0001
21	20	2027.5825	-0.0011	4	5	1881.4743	-0.0001
20	19	2022.8190	-0.0002	5	6	1875.0165	0.0000
19	18	2017.9797	-0.0005	6	7	1868.5030	0.0000
18	17	2013.0674	-0.0001	7	8	1861.9347	0.0002
17	16	2008.0822	0.0004	8	9	1855.3114	-0.0001
16	15	2003.0241	0.0001	9	10	1848.6347	0.0000
15	14	1997.8948	0.0001	10	11	1841.9048	0.0000
13	12	1987.4252	0.0000	11	12	1835.1219	-0.0005
12	11	1982.0864	-0.0001	12	13	1828.2880	-0.0001
11	10	1976.6795	0.0000	13	14	1821.4023	-0.0001
10	9	1971.2049	0.0000	14	15	1814.4664	0.0004
9	8	1965.6635	0.0000	15	16	1807.4800	0.0004
8	7	1960.0561	0.0000	16	17	1800.4435	0.0000
7	6	1954.3834	0.0000	18	19	1786.2241	-0.0010
6	5	1948.6461	0.0001				
5	4	1942.8448	0.0000				
4	3	1936.9804	0.0000				
3	2	1931.0538	0.0001				
2	1	1925.0651	0.0000				
1	0	1919.0153	-0.0002				

[a] The observed-minus-calculated values have been computed using the constants of Table 5.11 for the 000 and 001 states.

Table A11. Line positions (in cm^{-1}) for the $001(\Sigma_u^+) \rightarrow 000(\Sigma_g^+)$ band of $^{202}HgD_2$.[a]

J'	J''	Wavenumber	Obs – Calc	J'	J''	Wavenumber	Obs – Calc
29	28	1455.7754	-0.0001	1	2	1369.5630	0.0002
27	26	1450.9254	0.0006	2	3	1366.4188	0.0003
26	25	1448.4593	-0.0008	3	4	1363.2530	-0.0004
25	24	1445.9697	0.0006	4	5	1360.0673	-0.0003
24	23	1443.4514	-0.0011	5	6	1356.8613	-0.0001
23	22	1440.9098	-0.0003	6	7	1353.6348	0.0000
22	21	1438.3422	-0.0002	7	8	1350.3883	0.0000
21	20	1435.7498	0.0005	8	9	1347.1216	-0.0001
20	19	1433.1307	-0.0004	9	10	1343.8352	-0.0001
19	18	1430.4881	0.0000	10	11	1340.5294	0.0002
18	17	1427.8203	-0.0001	11	12	1337.2036	-0.0001
17	16	1425.1285	0.0003	12	13	1333.8587	-0.0002
16	15	1422.4111	-0.0006	13	14	1330.4948	-0.0001
15	14	1419.6710	0.0000	14	15	1327.1120	0.0001
14	13	1416.9066	0.0003	15	16	1323.7101	0.0000
13	12	1414.1182	0.0002	16	17	1320.2895	-0.0001
12	11	1411.3058	-0.0002	17	18	1316.8505	0.0000
11	10	1408.4707	0.0001	18	19	1313.3930	0.0000
10	9	1405.6120	0.0000	19	20	1309.9170	-0.0003
9	8	1402.7306	0.0002	20	21	1306.4234	0.0000
8	7	1399.8261	0.0001	21	22	1302.9117	0.0000
7	6	1396.8986	-0.0002	22	23	1299.3822	0.0002
6	5	1393.9492	0.0000	23	24	1295.8351	0.0003
5	4	1390.9773	0.0002	24	25	1292.2712	0.0011
4	3	1387.9827	-0.0003	25	26	1288.6878	-0.0003
3	2	1384.9671	0.0002	26	27	1285.0868	-0.0020
2	1	1381.9298	0.0008	27	28	1281.4727	0.0003
1	0	1378.8702	0.0008	28	29	1277.8388	-0.0003
				29	30	1274.1889	-0.0002

[a] The observed-minus-calculated values have been computed using the constants of Table 5.12 for the 000 and 001 states.

Table A12. Line positions (in cm^{-1}) for the $001(\Sigma_u^+) \rightarrow 000(\Sigma_g^+)$ band of $^{200}HgD_2$.[a]

J'	J''	Wavenumber	Obs – Calc	J'	J''	Wavenumber	Obs – Calc
29	28	1455.9048	-0.0001	0	1	1372.8199	0.0025
27	26	1451.0543	0.0001	1	2	1369.6936	-0.0005
26	25	1448.5869	-0.0025	2	3	1366.5501	0.0004
25	24	1446.0965	-0.0021	3	4	1363.3847	0.0002
24	23	1443.5815	-0.0005	4	5	1360.1986	-0.0001
23	22	1441.0396	0.0000	5	6	1356.9925	0.0001
22	21	1438.4723	0.0004	6	7	1353.7660	0.0002
21	20	1435.8789	-0.0001	7	8	1350.5191	-0.0001
20	19	1433.2607	-0.0002	8	9	1347.2525	0.0000
19	18	1430.6179	0.0000	9	10	1343.9660	0.0000
18	17	1427.9503	-0.0001	10	11	1340.6599	0.0000
17	16	1425.2585	0.0002	11	12	1337.3343	0.0000
16	15	1422.5418	0.0000	12	13	1333.9900	0.0006
15	14	1419.8011	-0.0001	13	14	1330.6254	0.0002
14	13	1417.0367	0.0000	14	15	1327.2424	0.0002
13	12	1414.2485	0.0001	15	16	1323.8401	-0.0001
12	11	1411.4370	0.0004	16	17	1320.4193	-0.0002
11	10	1408.6013	0.0000	17	18	1316.9805	0.0002
10	9	1405.7428	0.0000	18	19	1313.5220	-0.0007
9	8	1402.8613	0.0000	19	20	1310.0474	0.0005
8	7	1399.9570	0.0000	20	21	1306.5525	-0.0005
7	6	1397.0299	0.0000	21	22	1303.0412	0.0001
6	5	1394.0802	0.0000	22	23	1299.5120	0.0006
5	4	1391.1084	0.0001	23	24	1295.9633	-0.0009
4	3	1388.1140	-0.0003	24	25	1292.4012	0.0017
3	2	1385.0976	-0.0005	25	26	1288.8173	0.0000
2	1	1382.0592	-0.0011	27	28	1281.6016	-0.0001
1	0	1379.0015	0.0008	29	30	1274.3195	0.0010

[a] The observed-minus-calculated values have been computed using the constants of Table 5.13 for the 000 and 001 states.